

Vibration-based condition monitoring in planetary gearbox via using an internal sensor

Zhiqi Fan

A thesis in fulfilment of the requirements for the degree of
Master of Engineering



School of Mechanical & Manufacturing Engineering
Faculty of Engineering
The University of New South Wales

April 2015

Originality Statement

'I hereby declare that this submission is my own work and to the best of my knowledge it contains no materials previously published or written by another person, or substantial proportions of material which have been accepted for the award of any other degree or diploma at UNSW or any other educational institution, except where due acknowledgement is made in the thesis. Any contribution made to the research by others, with whom I have worked at UNSW or elsewhere, is explicitly acknowledged in the thesis. I also declare that the intellectual content of this thesis is the product of my own work, except to the extent that assistance from others in the project's design and conception or in style, presentation and linguistic expression is acknowledged.'

Signed 

Date 14/04/2015

Copyright Statement

'I hereby grant the University of New South Wales or its agents the right to archive and to make available my thesis or dissertation in whole or part in the University libraries in all forms of media, now or here after known, subject to the provisions of the Copyright Act 1968. I retain all proprietary rights, such as patent rights. I also retain the right to use in future works (such as articles or books) all or part of this thesis or dissertation. I also authorise University Microfilms to use the 350 word abstract of my thesis in Dissertation Abstract International (this is applicable to doctoral theses only). I have either used no substantial portions of copyright material in my thesis or I have obtained permission to use copyright material; where permission has not been granted I have applied/will apply for a partial restriction of the digital copy of my thesis or dissertation.'

Signed..........

Date14/04/2015.....

Authenticity Statement

'I certify that the Library deposit digital copy is a direct equivalent of the final officially approved version of my thesis. No emendation of content has occurred and if there are any minor variations in formatting, they are the result of the conversion to digital format.'

Signed 

Date 14/04/2015

Abstract

With the benefits of strong load-bearing capacity, compact, light weight and large transmission ratio, planetary gearboxes are widely applied in the fields of automobiles, helicopters, wind turbines, etc. However, at harsh working environments, some critical components of planetary gearboxes, such as gears and bearings, are extremely vulnerable to faults after the long-time operation, which may cause the breakdown of the entire machinery system.

Vibration analysis is an efficient way for monitoring the machine conditions to avoid the catastrophic failures and facilitate maintenance plans for numerous industrial applications. However, there is still a lack of successful signal processing strategies for the detection and diagnosis of bearing faults of the planetary gearbox. Because planetary gearbox comprises many rotating components that lead to signal contamination by strong background noise. Besides, the transmission path between an externally mounted sensor and fault signal source is time-varying, which means those traditional fault diagnosis methods developed for fixed-axis gearboxes may not work.

For the purpose of solving the aforementioned bearing fault detection issues in the planetary gearbox, this thesis utilizes an internally mounted accelerometer for the vibration data collection. This thesis also develops a hybrid signal processing approach to the internal sensor-based measurement. The result shows that, in contrast to the externally mounted sensor, the internal sensor has an overwhelmingly superior performance for the inner race faults detection in the planet bearings.

In addition, a novel spectral kurtosis (SK) based demodulation band selection approach is presented in this thesis. This method is introduced to address the electromagnetic interference (EMI) issue from internal sensor-based measurement. It also could be further applied in other industrial cases where intense EMI appears.

Acknowledgements

First and foremost, I would like to thank my supervisors Professor Zhongxiao Peng and Dr Huaizhong Li for their assistance, guidance and patience during my candidature. Your help is inestimable.

I would like to thank my co-supervisor Dr Wade Smith for helping me in better understanding the academic knowledge and offering great help in research algorithm construction and experimental study. Also, sincere thanks to my co-supervisor Professor Robert Bond Randall for his advice and assistance on the research topics.

I would like to thank Mr Russell Overhaul and Mr Vincenzo Carnevale for their assistance in gearbox design and assembly as well as laboratory testing.

In addition, I would like to thank my colleagues, PhD students Chongqing Hu and Xiaogang Zhang for their assistance in learning the basic theory and resolving some experimental issues.

Last but not least, I would like to thank my parents for their patience, understanding, support and encouragement.

Table of Contents

Originality Statement	II
Copyright Statement	III
Authenticity Statement	IV
Abstract	V
Acknowledgements	VI
Table of Contents	VII
List of Publications	XII
List of Figures	XIII
List of Tables	XIX
List of Abbreviations	XX
 CHAPTER 1 INTRODUCTION	 1
1.1 Background and Motivation	1
1.2 Research objectives	4
1.3 Thesis structure	5
 CHAPTER 2 LITERATURE REVIEW	 6
2.1 Introduction	6
2.2 Machine condition monitoring	6
2.2.1 Basic concept	6
2.2.2 Condition monitoring techniques	7
2.3 Vibration-based bearing fault diagnosis	9
2.3.1 Vibration signal induced by the bearing fault	9
2.3.2 Random and deterministic signal separation	12
2.3.2.1 Time synchronous averaging (TSA)	13

2.3.2.2 Self-adaptive noise cancellation (SANC)	14
2.3.2.3 Discrete random separation (DRS)	15
2.3.2.4 Cepstrum pre-whitening	15
2.3.3 Bearing signal enhancement techniques	16
2.3.3.1 Minimum entropy deconvolution (MED)	17
2.3.3.2 Empirical mode decomposition (EMD)	18
2.3.3.3 Spectral Kurtosis (SK)	19
2.3.4 Bearing faults feature extraction techniques	21
2.3.4.1 Time domain methods	21
2.3.4.2 Frequency domain methods	23
2.3.4.3 Time-Frequency Domain methods	23
2.3.4.4 Envelope analysis	24
2.4 Planetary gearbox fault diagnosis	25
2.4.1 Gear fault diagnosis	25
2.4.2 Bearing fault diagnosis	27
2.5 Summary	29
 CHAPTER 3 METHODOLOGY	 30
3.1 Introduction	30
3.2 An overview of the methodology	30
3.3 Experimental setup and data collection	32
3.3.1 Test equipment preparation	32
3.3.1.1 Planetary gearbox test rig	32
3.3.1.2 Data collection system	36
3.3.1.3 Sensing by using internal vibration sensor	38
3.3.2 Bearing faults seeding	39
3.4 Data analysis	40
3.4.1 EMI signal filtering	41

3.4.2 Optimum demodulation band selection	41
3.4.3 A hybrid signal processing procedure	42
3.5 Summary	43
 CHAPTER 4 ELECTROMAGNETIC INTERFERENCE ISSUE AND THE FILTERING SOLUTIONS	 44
4.1 Introduction	44
4.2 Review of the EMI issue in bearing fault diagnosis	45
4.3 Further examination of EMI issue and EMI components	46
4.4 EMI signal filtering strategies	48
4.4.1 DRS based filtering	49
4.4.2 Cepstrum editing based filtering	52
4.4.3 Cepstrum whitening based filtering	55
4.5 Discussion	58
4.6 Summary	58
 CHAPTER 5 A NOVEL SPECTRAL KURTOSIS METHOD FOR DEMODULATION BAND SELECTION.....	 59
5.1 Introduction	59
5.2 Review of Fast Kurtogram and Protrugram	60
5.2.1 Fast Kurtogram	60
5.2.2 Protrugram	61
5.3 Vibration signal description	62
5.3.1 Test equipments.....	63
5.3.2 Bearing fault information.....	63
5.3.3 Test conditions.....	64
5.3.4 Bearing fault frequencies	64
5.4 Results with established methods.....	65

5.4.1 Outer race fault detection	66
5.4.2 Inner race fault detection.....	73
5.5 Introduction of the new presented method 'Kurtrugram'	80
5.6 Results with Kurtrugram	82
5.6.1 Outer race fault detection	83
5.6.2 Inner race fault detection.....	86
5.7 Discussions.....	89
5.7.1 Comparison of methods	89
5.7.2 Computation time.....	90
5.7.3 Limitations of the presented method.....	90
5.8 Summary	91
 CHAPTER 6 A HYBRID BEARING DIAGNOSTIC APPROACH BASED ON INTERNAL SENSOR MEASUREMENT	 92
6.1 Introduction	92
6.2 Planetary bearing diagnostic procedures.....	93
6.3 Vibration signal description	95
6.3.1 Test equipment	95
6.3.2 Bearing fault information.....	96
6.3.3 Test conditions.....	96
6.3.4 Planetary gearbox calculations.....	97
6.3.4.1 Components frequency calculations	97
6.3.4.2 Bearing fault frequencies	98
6.4 Experimental results.....	98
6.4.1 Outer race fault detection	98
6.4.1.1 1.6 mm defect size.....	99
6.4.1.2 1.2 mm defect size.....	103
6.4.1.3 0.8 mm defect size.....	108

6.4.1.4 0.4 mm defect size.....	112
6.4.2 Inner race fault detection.....	115
6.4.2.1 1.6 mm defect size.....	116
6.4.2.2 1.2 mm defect size.....	120
6.4.2.3 0.8 mm defect size.....	125
6.4.2.4 0.4 mm defect size.....	129
6.5 Discussions.....	133
6.5.1 Performance of outer race fault detection	133
6.5.2 Performance of inner race fault detection	134
6.5.3 Effectiveness and limitations of the presented approach	135
6.6 Summary	136
CHAPTER 7 CONCLUSION AND FUTURE WORK.....	137
7.1 Conclusions	137
7.2 Future work	138
7.2.1 Internal sensor-based measurement	138
7.2.2 EMI issue	139
References	141
Appendix MATLAB signal processing codes.....	151
A. Envelope analysis.....	151
B. Protrugram.....	153
C. Kurtrugram	154
D. Pulse width modulation signal	155

List of Publications

Zhiqi Fan and Huaizhong Li, "Fault diagnosis of rolling element bearings based on signal pre-whitening and empirical mode decomposition," presented in the conference of International Forum on Systems and Mechatronics (IFSM), Taiwan, October 12-15, 2014.

Zhiqi Fan and Huaizhong Li, "A hybrid approach for fault diagnosis of planetary bearings using an internal vibration sensor," *Measurement*, vol. 64, pp. 71–80, 2015.

Zhiqi Fan and Huaizhong Li, "A new approach on fault diagnosis of rolling element bearings using signal pre-whitening method and empirical mode decomposition" *Journal of Mechanics*, submitted in December 2014 (under review).

Zhiqi Fan, Wade A. Smith, Zhongxiao Peng, Huaizhong Li and Robert B. Randall, "The Kurtrugram: a simple approach to demodulation band selection for bearing diagnostics under wideband interference," *Mechanical Systems and Signal Processing*, submitted in April 2015 (under review).

List of Figures

Fig. 1.1 (a) Wind turbine planetary gearbox [2] (b) Helicopter planetary gearbox [3]	
.....	Error! Bookmark not defined.
Fig. 1.2 Planetary gear sets [1].....	Error! Bookmark not defined.
Fig. 2.1 Structure of the rolling element bearing [25].....	Error! Bookmark not defined.
Fig. 2.2 Typical fault signals in rolling element bearing [27]	Error! Bookmark not defined.
Fig. 2.3 Key parameters in rolling element bearing [28]	Error! Bookmark not defined.
Fig. 2.4 Rolling element bearing single point defect model [29]...	Error! Bookmark not defined.
Fig. 2.5 The influence of random fluctuations on the bearing fault signal [31].....	Error! Bookmark not defined.
Fig. 2.6 Comb filter [36]	Error! Bookmark not defined.
Fig. 2.7 Schematic diagram of SANC [27]	Error! Bookmark not defined.
Fig. 2.8 A comparison between the envelope spectrum of (a) Original vibration signal (b) DRS filtered signal [41]	Error! Bookmark not defined.
Fig. 2.9 Procedure of Cepstrum pre-whitening.....	16
Fig. 2.10 STFT based SK for a simulated bearing fault signal [27]	Error! Bookmark not defined.
Fig. 2.11 Paving of the Fast Kurtogram [58]	Error! Bookmark not defined.
Fig. 2.12 Comparison of the Fast Kurtogram with the full Kurtogram [27].....	Error! Bookmark not defined.
Fig. 2.13 Hilbert transform method for envelope analysis [27]	Error! Bookmark not defined.
Fig. 3.1 The flowchart of methodology in this study	31
Fig. 3.2 UNSW gearbox test rig	33
Fig. 3.3 Test rig control panel	33

Fig. 3.4 CAD model of the planetary gearbox	34
Fig. 3.5 Details of the gear stages [86]	Error! Bookmark not defined.
Fig. 3.6 (a) Hunting tooth planetary gearbox; (b) CAD model of the planetary gearbox	36
Fig. 3.7 (a) Brüel & Kjær 4394 IEPE-type accelerometer; (b) Michigan Scientific B6-2 slip ring	36
Fig. 3.8 (a) Hiedhan 426-36000 shaft encoder; (b) Torque transducer	37
Fig. 3.9 Planetary gearbox test rig data capture system	37
Fig. 3.10 Mounting location of the internal sensor [13] .	Error! Bookmark not defined.
Fig. 3.11 (a) Top view of UNSW planetary gearbox [14]; (b) A CAD model for showing the locations of transducers	39
Fig. 3.12 (a) Simulated outer race fault; (b) Simulated inner race fault	40
Fig. 3.13 Layout of the bearing fault detection procedure	40
Fig. 4.1 The working procedure of VFD [91]	Error! Bookmark not defined.
Fig. 4.2 Generation of apparent sinusoid from pulse-width modulated signal. (a) Reference (···) and carrier (–) signals; (b) Pulse-width modulated signal (–) and generated sinusoid (···)	Error! Bookmark not defined.
Fig. 4.3 Time domain of the EMI signal. (a) No slip ring; (b) Slip ring	47
Fig. 4.4 Frequency domain of the EMI signal. (a) No slip ring; (b) Slip ring	48
Fig. 4.5 Zoomed spectrum of the EMI around 8000 Hz	48
Fig. 4.6 Time waveform: (a) raw signal, and (b) DRS filtered signal.....	50
Fig. 4.7 Comparison between the spectrum of raw signal and DRS filtered signal	50
Fig. 4.8 Comparison between the zoom of PSD of raw signal and DRS filtered signal (around 8000 Hz)	51
Fig. 4.9 Envelope spectrum: (a) raw signal, and (b) DRS filtered signal	51
Fig. 4.10 Time waveform: (a) raw signal, and (b) Cepstrum editing filtered signal.....	53
Fig. 4.11 Comparison between the spectrum of raw signal and cepstrum editing filtered signal	53

Fig. 4.12 Comparison between the zoom of PSD of raw signal and cepstrum editing filtered signal (around 8000 Hz)	54
Fig. 4.13 Envelope spectrum: (a) raw signal, and (b) Cepstrum editing filtered signal ..	54
Fig. 4.14 Time waveform: (a) raw signal, and (b) Cepstrum whitening Filtered signal ..	56
Fig. 4.15 Comparison between the spectrum of raw signal and Cepstrum whitening filtered signal.....	56
Fig. 4.16 Comparison between the zoom of PSD of raw signal and cepstrum whitening filtered signal (around 8000 Hz)	57
Fig. 4.17 Envelope spectrum: (a) raw signal, and (b) Cepstrum whitening filtered signal	57
Fig. 5.1 Time waveforms of ORF signals at torque loads of (a) 70 Nm, (b) 50 Nm, and (c) 30 Nm	66
Fig. 5.2 PSDs of ORF signals at torque loads of (a) 70 Nm, (b) 50 Nm, and (c) 30 Nm	67
Fig. 5.3 Fast Kurtogram for Case 1 (70 Nm, outer race fault).....	68
Fig. 5.4 Squared envelope spectrum from Fast Kurtogram for Case 1 (70 Nm, outer race fault)	69
Fig. 5.5 Protrugram for Case 1 (70 Nm, outer race fault).....	69
Fig. 5.6 Squared envelope spectrum from Protrugram for Case 1 (70 Nm, Outer race fault)	70
Fig. 5.7 Fast Kurtogram for Case 2 (50 Nm, outer race fault).....	71
Fig. 5.8 Squared envelope spectrum from Fast Kurtogram for Case 2 (50 Nm, outer race fault)	71
Fig. 5.9 Protrugram for Case 2 (50 Nm, outer race fault)	72
Fig. 5.10 Squared envelope spectrum from Protrugram for Case 2 (50 Nm, ORF)	72
Fig. 5.11 Time waveforms of IRF signals at torque loads of (a) 70 Nm, (b) 50 Nm, and (c) 30 Nm	73
Fig. 5.12 PSDs of IRF signals at torque loads of (a) 70 Nm, (b) 50 Nm, and (c) 30 Nm	74

Fig. 5.13 Fast Kurtogram for Case 4 (70 Nm, inner race fault)	75
Fig. 5.14 Squared envelope spectrum from Fast Kurtogram for Case 4 (70 Nm, inner race fault)	75
Fig. 5.15 Protrugram for Case 4 (70 Nm, inner race fault)	76
Fig. 5.16 Squared envelope spectrum from Protrugram for Case 4 (70 Nm, inner race fault)	76
Fig. 5.17 Squared envelope spectrum from Protrugram (The maximum of the 'hump') for Case 4 (70 Nm, inner race fault)	77
Fig. 5.18 Fast Kurtogram for Case 5 (50 Nm, inner race fault)	78
Fig. 5.19 Squared envelope spectrum from Fast Kurtogram for Case 5 (50 Nm, inner race fault)	78
Fig. 5.20 Protrugram for Case 5 (50 Nm, inner race fault)	79
Fig. 5.21 Squared envelope spectrum from Protrugram for Case 5 (50 Nm, inner race fault)	79
Fig. 5.22 Flow chart of the Kurtrugram	82
Fig. 5.23 Kurtrugram for Case 1 (70 Nm, outer race fault)	83
Fig. 5.24 Squared envelope spectrum from Kurtrugram for Case 1 (70 Nm, outer race fault)	84
Fig. 5.25 Kurtrugram for Case 2 (50 Nm, outer race fault)	85
Fig. 5.26 Squared envelope spectrum from Kurtrugram for Case 2 (50 Nm, outer race fault)	85
Fig. 5.27 Kurtrugram for Case 4 (70 Nm, inner race fault)	86
Fig. 5.28 Squared envelope spectrum from Kurtrugram for Case 4 (70 Nm, inner race fault)	87
Fig. 5.29 Kurtrugram for Case 5 (50 Nm, inner race fault)	88
Fig. 5.30 Squared envelope spectrum from Kurtrugram for Case 5 (50 Nm, inner race fault)	88
Fig. 6.1 Main components of a measured signal using an internal accelerometer	94

Fig. 6.2 Flow chart of the procedure developed for bearing fault diagnosis based on internal sensor measurements	95
Fig. 6.3 (a) Raw time signal; (b) Cepstrum whitened signal; (c) Signal after Cepstrum whitening and MED filter (45 Nm, 1.6 mm outer race fault, internal sensor).....	100
Fig. 6.4 Kurtrugram (1.6 mm outer race fault, internal sensor)	100
Fig. 6.5 Envelope spectrum (1.6 mm outer race fault, internal sensor)	101
Fig. 6.6 Envelope spectrum (Good bearing, internal sensor).....	101
Fig. 6.7 Kurtrugram (1.6 mm outer race fault, internal sensor)	102
Fig. 6.8 Envelope spectrum (1.6 mm outer race fault, internal sensor)	103
Fig. 6.9 (a) Raw time signal; (b) Cepstrum whitened signal; (c) Signal after Cepstrum whitening and MED filter (1.2 mm outer race fault, internal sensor).....	104
Fig. 6.10 Kurtrugram (1.2 mm outer race fault, internal sensor)	105
Fig. 6.11 Envelope spectrum (1.2 mm outer race fault, internal sensor)	105
Fig. 6.12 Envelope spectrum (Good bearing, internal sensor).....	106
Fig. 6.13 Kurtrugram (1.2 mm outer race fault, external sensor)	107
Fig. 6.14 Envelope spectrum (1.2 mm outer race fault, external sensor)	107
Fig. 6.15 (a) Raw time signal; (b) Cepstrum whitened signal; (c) Signal after Cepstrum whitening and MED filter (0.8 mm outer race fault, internal sensor).....	109
Fig. 6.16 Kurtrugram (0.8 mm outer race fault, internal sensor)	109
Fig. 6.17 Envelope spectrum (0.8 mm outer race fault, internal sensor)	110
Fig. 6.18 Envelope spectrum (Good bearing, internal sensor).....	110
Fig. 6.19 Kurtrugram (0.8 mm outer race fault, external sensor)	111
Fig. 6.20 Squared envelope spectrum (0.8 mm outer race fault, external sensor)	112
Fig. 6.21 (a) Raw time signal; (b) Cepstrum whitened signal; (c) Signal after Cepstrum whitening and MED filter (0.4 mm outer race fault, internal sensor).....	113
Fig. 6.22 Kurtrugram (0.4 mm outer race fault, internal sensor)	113
Fig. 6.23 Envelope spectrum (0.4 mm outer race fault, internal sensor)	114
Fig. 6.24 Kurtrugram (0.4 mm outer race fault, external sensor)	115

Fig. 6.25 Envelope spectrum (0.4 mm outer race fault, external sensor)	115
Fig. 6.26 (a) Raw time signal; (b) Cepstrum whitened signal; (c) Signal after Cepstrum whitening and MED filter (1.6 mm inner race fault, internal sensor).....	117
Fig. 6.27 Kurtrugram (1.6 mm inner race fault, internal sensor)	117
Fig. 6.28 Envelope spectrum (1.6 mm inner race fault, internal sensor)	118
Fig. 6.29 Envelope spectrum (good bearing, internal sensor)	118
Fig. 6.30 Kurtrugram (1.6 mm inner race fault, external sensor)	119
Fig. 6.31 Envelope spectrum (1.6 mm inner race fault, external sensor)	120
Fig. 6.32 (a) Raw time signal; (b) Cepstrum whitened signal; (c) Signal after Cepstrum whitening and MED filter (1.2 mm inner race fault, internal sensor).....	121
Fig. 6.33 Kurtrugram (1.2 mm inner race fault, internal sensor)	122
Fig. 6.34 Squared envelope spectrum (1.2 mm inner race fault, internal sensor).....	122
Fig. 6.35 Squared envelope spectrum (Good bearing, internal sensor)	123
Fig. 6.36 Kurtrugram (1.2 mm inner race fault, external sensor)	124
Fig. 6.37 Squared envelope spectrum (1.2 mm inner race fault, external sensor)	124
Fig. 6.38 (a) Raw time signal; (b) Cepstrum whitened signal; (c) Signal after Cepstrum whitening and MED filter (0.8 mm inner race fault, internal sensor).....	126
Fig. 6.39 Kurtrugram (0.8 mm inner race fault, internal sensor)	126
Fig. 6.40 Envelope spectrum (0.8 mm inner race fault, internal sensor)	127
Fig. 6.41 Envelope spectrum (good bearing, internal sensor)	127
Fig. 6.42 Kurtrugram (0.8 mm inner race fault, external sensor)	128
Fig. 6.43 Envelope spectrum (0.8 mm inner race fault, external sensor)	129
Fig. 6.44 (a) Raw time signal; (b) Cepstrum whitened signal; (c) Signal after Cepstrum whitening and MED filter (0.4 mm inner race fault, internal sensor).....	130
Fig. 6.45 Kurtrugram (0.4 mm inner race fault, internal sensor)	130
Fig. 6.46 Envelope spectrum (0.4 mm inner race fault, internal sensor)	131
Fig. 6.47 Kurtrugram (0.4 mm inner race fault, external sensor)	132
Fig. 6.48 Envelope spectrum (0.4 mm inner race fault, external sensor)	132

Fig. 6.49 Semi-automated procedure for bearing diagnosis [27]...**Error! Bookmark not defined.**

List of Tables

Table 5.1 Planet gear bearing parameters63

Table 5.2 Test conditions of the gearbox rig64

Table 5.3 Performance comparisons of the Kurtrugram, Fast Kurtogram and Protrugram
.....89

Table 6.1 Planet gear bearing parameters96

Table 6.2 Test conditions of the gearbox rig97

Table 6.3 Diagnostic results for tests with outer race faults133

Table 6.4 Diagnostic results for tests with inner race faults134

List of Abbreviations

AE	Acoustic emission
ANC	Adaptive noise cancellation
AR	Autoregressive
ASR	Adaptive stochastic resonance
BPFO	Ball pass frequency, outer race
BPFI	Ball pass frequency, inner race
BSF	Ball spin frequency
BW	Bandwidth
CBM	Condition-based maintenance
CF	Center frequency
CPB	Constant-percentage-bandwidth
CK	Correlated Kurtosis
DRS	Discrete/random separation
DTW	Dynamic time wrapping
EMI	Electromagnetic interference
EMD	Empirical mode decomposition
EEMD	Ensemble empirical mode decomposition
FTF	Fundamental train frequency

FIR	Finite impulse response
FRF	Frequency response function
FFT	Fast Fourier transform
IRT	Infrared thermography
IMF	Intrinsic mode function
IADT	Iterative atomic decomposition thresholding
ICA	Independent component analysis
LPF	Linear prediction filter
MED	Minimum entropy deconvolution
PSD	Power spectral density
RMS	Root mean square
SK	Spectral kurtosis
SANC	Self adaptive noise cancellation
SNR	Signal-to-noise ratio
STFT	Short time Fourier transform
SVD	Singular value decomposition
TSA	Time synchronous averaging
TKEO	Teager Kaiser energy operator
UNSW	University of New South Wales
VFD	Variable frequency drive
WPT	Wavelet packet transform
WVD	Wigner-Ville distribution

CHAPTER 1 INTRODUCTION

1.1 Background and Motivation

Owing to the advantages of large transmission ratio, strong load-bearing capacity and light weight, planetary gearbox is widely used in many industrial cases, such as hoisting, transportation, engineering machinery, metallurgy, mining, petrochemical, construction machinery and aerospace [1]. Fig. 1.1 presents typical examples of the planetary gearbox in wind turbine and helicopter.

Different from the fixed-axis gearboxes, planetary gearboxes are based on the transmission structure of the planetary gear set (Fig. 1.2), which is a compound gear system that mainly consists of the internally toothed ring gear, a set of externally toothed planet gears and a central, externally toothed sun gear. One of these three key components (ring gear, planet gear and sun gear) in planetary gear system is set to be stationary, and the other two remaining elements rotate around their centers (For the planet gear, it not only rotates around its center but also spins around the center of sun gear). By the selection of which of the elements above is driving, the rotational speed of the input shaft could be speed up or down.

Due to the compact structure, some crucial components of planetary gearbox, such as gears and bearings, could be damaged easily after long-time operation, which may then result in disastrous breakdown of the whole machinery system and cause casualties as well as economic loss. As illustrated in [4], the statistical results showed that, from 1990 to 1996, the various system and structure failure was one of the most frequent causes of accidents in a study with 1168 helicopter accidents. In addition, in 1999, for the world total of 192 turbine helicopter accidents, 28 were directly related to the mechanical failures happened in the drive train of gearboxes. Hence, it is essential to decide on an

efficient maintenance strategy for assuring a satisfactory level of reliability during the useful life of the mechanical elements [5].

Condition monitoring, known as a crucial part of predictive maintenance, is commonly used for recognising a significant change in machinery components and detecting mechanical faults at a very early stage. Condition monitoring has the benefits of minimizing downtime, reducing the maintenance cost, and maximizing productivity [6].

Among those primary condition monitoring techniques, vibration analysis is the most commonly used method for rotating machinery in industrial applications [6]. One reason is that vibration information in an operating machine is easily measured by installing an accelerometer mounted on the external casing. Another reason is the vibration information is sensitive to the failure of machinery components and could rapidly provide the state of the monitored components. Different signal processing techniques have been utilized in vibration analysis for improving the fault detection performance. These signal processing techniques could be mainly summarized into three categories: time-domain methods, frequency-domain methods and time-frequency-domain methods.

However, planetary gearbox exhibits unique challenges in both bearing and gear fault detection through applying signal processing techniques. As the explanations in [3], those planets all run with the same speeds and loads, which means healthy components have the possibilities in masking the vibration signal generated by faulty components. In addition, as the planet gears exhibit epicyclic motion about the sun gear, the location of defective parts change and propose a challenge for the externally mounted sensor in data collection. In recent years, while numbers of signal processing techniques for monitoring gears fault had been published [3, 7-11], there is still lack of practical approaches for the fault diagnosis of the planetary bearing, which could also cause the breakdown of the machinery [12]. The difficulties of the fault detection in bearing of the planetary gearbox were further illustrated in [12], the major problem of detecting and

diagnosing bearing faults is that the vibration signals were strongly masked by gear signals that covered the whole of frequency range to over 20 kHz. Another problem is that, in the planetary drive, the bearing fault signal must be transmitted to the externally mounted vibration sensor through a time-varying path.

Other than developing a signal processing procedure for enhancing the performance of bearing fault detection, another solution could be improving the sensor location. In [13], an accelerometer was mounted on the planet carrier for the gear fault diagnosis. This internally mounted sensor, which was located on the planet carrier and rotating with the planet carrier, may provide potentially better performance than the traditional externally fixed sensor. Because this internal sensor is closer to most potential fault signal sources, the collected fault signal would likely have a higher signal-to-noise ratio (SNR). In addition, the internal sensor rotates with the planet carrier, which mitigates the problem of variable transmission paths. Several tests related to the internal sensor-based measurement in planetary bearing diagnosis are presented in [14]. Both full and narrow bandwidth envelope analysis techniques were combined with several preprocessing steps and compared, and the results demonstrated partially the benefits of the internal sensor-based measurement. However, its limitations were also reflected in these tests. The main problem is the contamination of the electromagnetic interference (EMI). EMI interference is defined as any unwanted signal that is either radiated or conducted to electronic equipments [15], and the EMI signal generated by the variable frequency drive (VFD) severely affects the performance of the adopted signal processing techniques.

As the above, one of the primary motivations of this project was to improve the vibration analysis based fault detection performance in planetary gearbox by adopting an internal accelerometer and developing an efficient signal processing strategy for internal sensor-based measurement. Understanding the shortcomings of the internal sensor-based measurement and exploring the possible solutions were also the incentives for this study.

1.2 Research objectives

As the main goals of this study is the investigation of bearing fault detection performance for the internal sensor and resolving the existing problems of internal sensor-based measurement as mentioned in previous section, the thesis touches on three main areas: EMI signal filtering, bearing fault signal enhancement and developing an effective bearing fault detection procedure for internal sensor-based measurement.

For the EMI signal filtering, as the previous study [14] showed the fact that the vibration signal collected from the internal sensor was strongly corrupted by the EMI signal, thus the primary objective of this part is to understand the properties of the EMI signal and find a valid technique for filtering out the EMI signal from the bearing fault signal. A series of advanced signal processing techniques could be applied to the collected EMI signal with the objective of testing the filtering performance.

The research of bearing fault signal enhancement is also for tackling the issue related to the EMI interference from internal sensor-based measurement. The primary objective is devising a new signal processing algorithm or optimizing the current techniques for increasing the signal-to-noise ratio of the bearing fault signal and reducing the impact of the EMI signal.

The development of a bearing fault detection procedure is the further step after the EMI signal filtering and bearing fault signal enhancement. The research results from previous two parts could be supplemented to this part for constituting a systematic and efficient signal processing algorithms, and then the internal sensor-based measurement could be further comprehensively investigated for bearing fault detection in planetary gearboxes.

1.3 Thesis structure

The thesis is organized into seven chapters including this chapter. The topics discussed in each chapter are summarized as follows:

Chapter 1 introduces the background of this project, research objectives and thesis structure.

Chapter 2 reviews a series of condition monitoring methods and the existing signal processing techniques for bearing fault diagnosis. It also introduces the current signal processing techniques for the planetary gearbox fault diagnosis.

Chapter 3 presents the methodology of this project. Both the vibration data analysis and the experimental work are described in this chapter for showing how to achieve the research objectives.

Chapter 4 is for finding an effective signal processing technique for filtering out the electromagnetic interference signal (EMI) from the vibration signal collected by the internal sensor. The performances of several existing signal processing techniques, which are generally used for the separation between random and deterministic signal, are compared in this chapter.

Chapter 5 presents a novel spectral kurtosis (SK) based demodulation band selection method for the bearing fault signal masked by intense EMI. The performance of the proposed method is compared with two well-established signal processing techniques (Fast Kurtogram and Protrugram) to evaluate the performance of this newly developed technique in this chapter.

Chapter 6 presents a novel hybrid signal processing procedure for internal sensor-based measurement. This process combines several advanced signal processing techniques such as Cepstrum whitening, minimum entropy deconvolution (MED), new SK based method (mainly introduced in Chapter 5) and envelope analysis.

Chapter 7 is the conclusions and future works.

CHAPTER 2 LITERATURE REVIEW

2.1 Introduction

In this chapter, a literature review is presented on vibration-based condition monitoring, with emphasis on bearing diagnostics and in particular on diagnostics in planetary gearboxes. Section 2.2 illustrates the basic concept of condition monitoring and several common condition monitoring methods. Section 2.3 presents the existing vibration analysis techniques for diagnosing rolling element bearing faults. Firstly, a brief description of the rolling element bearing fault signal and the mathematical localized bearing fault models built by previous researchers are shown in this part. Then, signal processing techniques for three different purposes are reviewed: random signal and deterministic signal separation, bearing fault signal enhancement, bearing fault extraction. Section 2.4 mainly introduces some recent publications related to the planetary gearbox diagnosis for both gears and bearing faults.

2.2 Machine condition monitoring

2.2.1 Basic concept

Machine condition monitoring is the process that determines the operational machinery current status and predicts their future state. Condition monitoring aims at minimizing downtime, reducing maintenance costs and maximizing productivity [16]. By means of monitoring some specific parameters from operating machines, such as vibration, sound, lubricant or temperature, abnormal symptoms or the information of degradation can be detected and further arrangement can then be made for the correction before a major malfunction of a machine or specific components.

Condition monitoring is a crucial part of condition-based maintenance (CBM), in which the maintenance is based on the perceived condition of operating machines [6]. There are three available maintenance strategies, the earliest being the run to failure approach, in which machines are simply run until they breakdown. It applies in situations in which the consequences of failure are insignificant. A later maintenance strategy is preventive maintenance, which sets a periodic interval to perform preventive maintenance regardless of the health status of a physical asset [5]. In contrast to the aforementioned two maintenance strategies, CBM has several advantages [6]: a) the potential breakdown of a machine is predicted through regular condition monitoring and maintenance is carried out at the optimum time; b) CBM not only determines the current state, but also gives reasonable predictions of remaining useful life. However, CBM also has several limitations [6]. First, it is complicated to build a general method that can be correctly employed for determining the current condition and having reasonable predictions; Second, the initial cost of CBM is very large, because sufficient monitoring instruments are required to be installed in operational machinery. Given all this, currently, CBM is only used for the crucial parts of the equipment where increased reliability and safety are required.

2.2.2 Condition monitoring techniques

Aiming at monitoring the condition of operational machines, several methods are used for externally obtaining the information of the internal state of operational machine. Commonly used techniques include vibration analysis, oil analysis, acoustic emissions and infrared thermography.

Vibration analysis is the most commonly used method of machine condition monitoring [6]. Operational machinery generates vibration in any working condition, and an increasing level of some parameters of vibration signal may reveal a fault in a particular machine component. The vibration signal is measured through transducers,

such as a proximity probe, velocity sensor or accelerometer. By analyzing the vibration signature from properly located sensors, mechanical faults for instance, imbalance, misalignment, mechanical looseness, rubs, bearing defects, faults in gears, oil whirl, blades defects, local resonances, etc [17], have a high chance of being revealed.

Oil analysis is used to monitor the machinery conditions through analyzing lubricant properties, suspended contaminants and wear debris. In comparison with vibration analysis, oil analysis has the advantage of monitoring the condition of low-speed machinery where it is difficult in applying techniques of vibration analysis [18]. However, this method can only be used when the machine has a continuous oil supply, meaning that oil analysis is not practical for grease-lubricated machines [19]. In some publications [18, 20-21], the oil analysis was combined with vibration analysis. The results showed these two techniques had their respective advantages, and their integration can give a comprehensive diagnosis of machinery condition. Vibration analysis could provide fast and accurate results for the machine state while the oil analysis could provide more details about the wear rate and mechanisms [20].

Acoustic emission (AE) is a non-destructive condition monitoring technique for detecting plastic deformation and defect growth in metals and composites. The basic principle is: when the material is subjected to stress at a certain level, a rapid release of strain energy occurs in the form of elastic waves [22]. These elastic waves could then be detected by an AE sensor. In contrast with vibration analysis, which only detects faults on the material surface, AE has the advantage of identifying the growth of subsurface cracks [22]. In the application of bearing condition monitoring, the AE signal has better performance than vibration analysis in bearing fault diagnosis under the high noise environment [19]. As the bearing failure induced vibration has relatively low energy, and the bearing fault signal is hard to be directly extracted from the background noise. However, in this condition, the transient elastic waves collected by AE sensor in high-frequency regions could provide useful indications of the bearing defects [19].

Infrared thermography (IRT) is an effective condition monitoring tool for the

real-time temperature monitoring in a non-contact way [23]. Temperature is a significant parameter for reflecting the inner condition of operational machinery, because faulty machines, damaged metallic or metalloid components may cause slight temperature variations of the equipment [23]. In order to observe this temperature change, the IRT technique is utilized for transforming the thermal energy, which is emitted from objects in the infrared band of the electromagnetic spectrum, into an electronic video signal and then into the visible image represented by each energy level in different colors [24]. IRT uses a camera with an infrared detector for absorbing IR energy emitted from detecting an object and converting it into the electrical current for later processing. Compared with other condition monitoring methods, one of the primary benefits of IRT is that it has minimal instrumentation, as only an infrared camera, a tripod and a video output for showing the 2D thermal images are required during the detection process. Further, IRT enables simultaneous monitoring over a large area due to its remote and non-invasive nature [23].

2.3 Vibration-based bearing fault diagnosis

In this part, the bearing failure induced vibration signal is detailed described and existing vibration analysis techniques for diagnosing rolling element bearing faults are reviewed. Firstly, a brief description of the rolling element bearing fault signal and the mathematical localized bearing fault models built by previous researchers are shown in section 2.3.1. Secondly, the signal processing techniques with three different purposes are presented: random signal and deterministic signal separation (section 2.3.2), bearing fault signal enhancement (section 2.3.3), bearing fault extraction (section 2.3.4).

2.3.1 Vibration signal induced by the bearing fault

Rolling element bearings consist of a number of rollers or balls that sit between the two bearing rings (or ‘races’) and support the applied load. The structure of a rolling

element bearing is pictured in Fig. 2.1. The essential components of the rolling element bearing include outer race, inner race, rolling element and cage. The outer race is used for supporting and the inner race rotates with the shaft. The cage is utilized to make sure that the rolling elements are well-distributed and preventing the rolling elements from falling off. As rolling element bearings are one of the most widely applied elements in industrial machinery and their failure is one of the most common factors for machine breakdown, it is crucial to recognize the bearing fault signal at a very early stage before it causes a catastrophic failure [6].

The vibration signals of different bearing faults are illustrated in Fig. 2.2. It can be seen that when a defect in one surface of a rolling element bearing strikes another surface, an impulse is produced that may excite the resonances of the bearing or the whole mechanical system. A series of (near) periodically-spaced impulses are generated when the bearing rotates with the shaft [26]. As the repetition frequency of the impulses is determined uniquely by the location of the defect (such as defects on the inner race, outer race, cage or the rolling elements), it is essential to calculate these repetition frequencies of impulses based on several parameters of the bearing (shown in Fig. 2.3) for recognizing the bearing fault location. The formulas for the bearing fault characteristic frequencies are presented below [26].

$$\text{Outer race fault} \quad BPFO = \frac{nf_r}{2} \left\{ 1 - \frac{D_b}{D_m} \cos \alpha \right\} \quad (2.1)$$

$$\text{Inner race fault} \quad BPFI = \frac{nf_r}{2} \left\{ 1 + \frac{D_b}{D_m} \cos \alpha \right\} \quad (2.2)$$

$$\text{Cage fault} \quad FTF = \frac{f_r}{2} \left\{ 1 - \frac{D_b}{D_m} \cos \alpha \right\} \quad (2.3)$$

$$\text{Rolling elements fault} \quad BSF = \frac{Df_r}{2D_b} \left\{ 1 - \left(\frac{D_b}{D_m} \cos \alpha \right)^2 \right\} \quad (2.4)$$

Where f_r is the shaft speed, n is the number of rolling elements, α is the angle of the load from the radial plane, D_b is the rolling element diameter and D_m is the pitch diameter of the bearing.

In order to provide a further understanding of the components of the bearing fault signal and comprehending how fault symptoms are generated, several mathematical models of the localized faults in rolling element bearings are reviewed here. McFadden and Smith [29] developed a model for describing a single point defect on the inner race of a rolling element bearing under a constant radial load. The bearing defects induced impulses that were modeled as a function of the rotation of the bearing, the load distribution of the bearing, the transfer function between bearing and transducer, and the exponential decay of the resonances excited. This model, as presented in Fig. 2.4, shows that the following equation could explain the collected vibration signal $v(t)$:

$$v(t)=[d(t)\times q(t)\times a(t)]*e(t) \quad (2.5)$$

Where $d(t)$ is the bearing fault signal, $q(t)$ is the function of instantaneous load on a point on the inner race, $a(t)$ is the transfer function between the point of impact and the measuring point, and $e(t)$ is the exponential decay function.

This model was extended in [30] for describing the vibration generated by multiple point defects, the influence of the various defects in the original model is that parts of spectral lines would be cancelled or reinforced due to the differing phase angles.

Ho and Randall further updated McFadden and Smith's model in [31] in which the new model that incorporates slight random variations (a small percentage of 1-2%) in the time between pulses. The generation of random fluctuations in real cases is caused by variations in clearances in the cage and the variation in the radial load on the rolling elements when they passed through the radial load zone. The effects of the random fluctuations of the bearing fault signal are illustrated in Fig. 2.5. It is noted that the spectrum of the temporal signal without random fluctuations can clearly show the higher harmonics of bearing fault frequency while these components smear into each other in the case of 0.75% random fluctuations. This figure also illustrates the

superiority of analyzing the envelope spectrum, because the bearing fault frequency and its harmonics can be clearly recognized from the envelope spectrum in both cases, while the harmonic spacing (fault frequency) around the excited high-frequency resonance is difficult to identify in the case of 0.75% random fluctuation.

The bearing fault could also be modeled as a second order cyclostationary process [32]. By definition, a cyclostationary process is a stochastic process that exhibits some hidden periodicities in its statistical structure [33]. For the case of bearing fault signal, the occurrences of the defect induced impacts never occur at the same position from one period to another (caused by random slip of the rolling element), and these impacts are further amplitude modulated as the movement of the fault in and out of the load zone. Thus, the vibration signal from rolling element bearings shows the property of cyclostationarity [34]. The bearing fault signal could be modeled as the following expression [32]:

$$x(t) = \sum_i A_i s(t - iT - \tau_i) + n(t) \quad (2.6)$$

Where $s(t)$ is the waveform generated by a single impact, T is the mean spacing between impacts, τ_i is the time lag between the mean period due to the presence of slip, A_i is the amplitude of the i th impact force and accounts for possible periodic modulations and $n(t)$ is an additive background noise.

2.3.2 Random and deterministic signal separation

In industrial applications, the faulty bearing signals are often relatively weak and are easily masked by strong deterministic signals, such as from gears [27]. Thus, it is a wise choice to remove deterministic components as the first step in bearing fault diagnosis. A series of signal processing techniques, such as time synchronous averaging (TSA), self-adaptive noise cancellation (SANC), discrete random separation (DRS) and Cepstrum pre-whitening, are introduced in this section with the purpose of separation between the random signal and deterministic signal.

2.3.2.1 Time synchronous averaging (TSA)

TSA was first proposed in [35], and is done by averaging together a series of signal parts, each of which relates to one period of a synchronizing signal. The expression is shown as follows [27]:

$$y(t) = \frac{1}{N} \sum_{n=0}^{N-1} x(t - nT) \quad (2.7)$$

Where $x(t)$ is the synchronizing signal, T is the periodic time, and n is the number of periods used. Unlike conventional filtering, which is not effective when the signal and noise occupy the same part of the frequency spectrum, TSA attenuates the noise part. This is because noise makes a random contribution in each sample point on repetition.

TSA is modeled as the convolution of the finite train of impulses and the periodic time T of the desired signal. Therefore, it is equivalent to multiplying the Fourier transform of the noise signal by a comb filter (as shown in Fig. 2.6) in the frequency domain [27]. Increasing the number of repetitions can narrow the teeth of the comb and improve the SNR [31].

In [37], McFadden indicated that TSA can be applied to rotating machines for extracting a periodic signal such as the tooth meshing vibration of a single gear. However, the existing method of TSA needed to be modified, because digital computers can only process signals of finite length while the traditional TSA method assumes the length of the signal to be infinite. The author modified the method by applying a rectangular window to the signal in the time domain and sampling of the Fourier transform of the signal in the corresponding spectrum.

TSA was further utilized, in combination with envelope analysis, for the early detection of inner race faults in rolling element bearings in [38]. Synchronizing the envelope signal in different periods could provide more bearing fault information: by synchronizing the envelope signal with the inner race rotation speed, the influence of

the load distribution in the bearing and the effects of transfer path to the mounted sensor were obtained, and the distribution of damage on the inner race was determined.

Although TSA effectively removes deterministic components with minimum disruption of the residual signal, it can be time consuming because TSA only removes one harmonic family at a time, and so it must repeatedly be applied in the case of complex transmissions with many different gears [27].

2.3.2.2 Self-adaptive noise cancellation (SANC)

SANC is based on the technique of adaptive noise cancellation (ANC), which was first proposed in [39]. ANC utilizes two signals, one a primary input signal containing some noise, and the other a reference signal. The latter is subtracted from the former and has one of the two uncorrelated components from the primary input signal. ANC adaptively searches for the transfer function between the two signals and subtracts the modified reference signal from the primary signal, leaving the other components [27]. However, obtaining an uncontaminated reference signal is unrealistic on a planetary gearbox, because all signals are transmitted through complex transmission paths to the casing.

As presented in [31], SANC only requires one signal to obtain the effect of separation by using a delayed version of the primary signal as the reference signal. This method is valid as the adaptive filter can find the transfer function between the deterministic part of the signal and the delayed version of itself when the delay is longer than the correlation length of the random signal [6]. The process of SANC is illustrated in Fig. 2.7. However, SANC also has two limitations as presented in [40]: a) SANC requires setting parameters and having an adaptation converge; b) in order to resolve numerous harmonics buried in a high level of noise, the filter length needs to be extremely long, which means this technique is slow to adapt and may suffer from convergence problems when other parameters are not tuned properly.

2.3.2.3 Discrete random separation (DRS)

With the purpose of overcoming the drawbacks of SANC, DRS was proposed in [41]. DRS directly estimates the noise cancellation frequency gain in the frequency domain based on FFT. It uses a series of Fourier transforms of blocks of data which are averaged to determine the optimal Wiener frequency response. Compared with the method of SANC, DRS does not require an adaptation process. Furthermore, DRS can give an optimal filter in one run while SANC needs to process the same signal many times in order to obtain the optimal solution. The performance of DRS is presented in Fig. 2.8 for a signal recorded on a machine with an inner race bearing fault. The defect frequency and its harmonics dominate the envelope spectrum after the noise cancellation by DRS.

2.3.2.4 Cepstrum pre-whitening

The Cepstrum based technique (Cepstrum editing) was firstly presented in [42] for removing the selected deterministic components from the bearing fault signal. Later, the Cepstrum pre-whitening method was proposed in [43] for bearing diagnosis through lowering the energy level of all deterministic components by setting them to the same level of background noise. Comparing with other techniques such as TSA [37], DRS [41] and SANC [40], Cepstrum pre-whitening is simpler, and order tracking is not required in this operation. Besides, it can remove both harmonics and modulation sidebands. The principle of Cepstrum pre-whitening is based on the real cepstrum [43]:

$$C[n] = \text{IDFT} \left\{ \text{FFT} \left(\frac{D(F[T])}{D(F[T])} \right) \right\} \quad (2.8)$$

Based on the above expression, the periodicity in the signal could produce peaks at the quefrency in the real cepstrum. The Cepstrum pre-whitening technique sets all values to zero in the real cepstrum domain to give all deterministic components in the frequency domain the same amplitude [43]. The procedure of Cepstrum pre-whitening is shown in Fig. 2.9. This process not only almost deletes all the deterministic information in the

signal, but also retains the bearing defect related information that is a pseudo-cyclostationary random signal in essence.

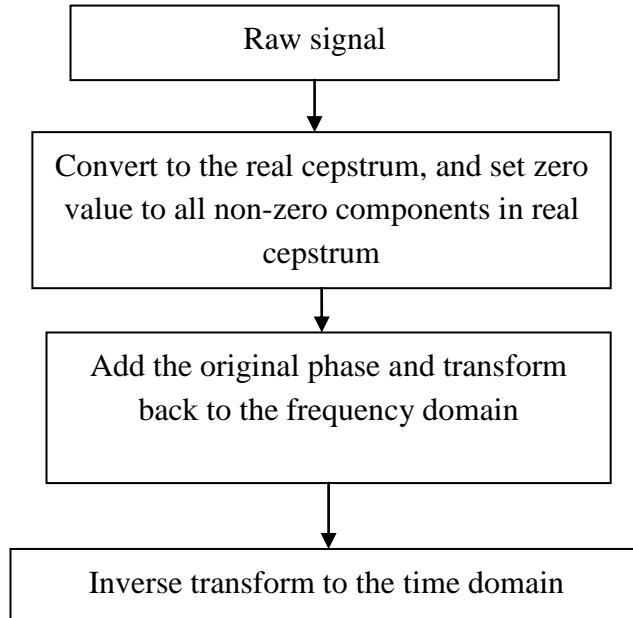


Fig. 2.1 Procedure of Cepstrum pre-whitening

In [43], the effectiveness of the Cepstrum pre-whitening in removing deterministic signal was further validated in various operating conditions, such as the steady state and the state of variable speeds. Cepstrum pre-whitening has also been compared with other filtering techniques, such as linear prediction filtering (LPF) and spectral kurtosis (SK) [43]. It has two superiorities: a) Cepstrum pre-whitening could be applied to full bandwidth envelope analysis in bearing diagnosis to avoid the risk, present in narrow bandwidth envelope analysis, of missing the fault signal; b) no additional parameters need to be set during the filtering process.

2.3.3 Bearing signal enhancement techniques

Although the deterministic components in collected vibration signal could be removed using the signal processing techniques mentioned in previous section, the bearing defect signal is often contaminated by random noise, which is difficult to filter

out [27]. Further, the individual fault pulses may be less impulsive due to the transmission path having a long impulse response. This section reviews techniques for eliminating the effect of the transmission path and enhancing the bearing fault signal with respect to residual background noise.

2.3.3.1 Minimum entropy deconvolution (MED)

The MED technique was initially developed as an auxiliary tool for extracting reflectivity information from seismic data [44]. Due to its validity in deconvolving impulsive excitations from the response signals, MED was applied by Endo and Randall [45] for enhancing the impulses generated by the local defects of gears. It was further used in [46] for optimizing bearing fault detection by increasing impulses caused by localized bearing defects.

The central idea of the MED technique is to produce an inverse filter for neutralizing the effect of the signal transmission path and searching for the best set of filter coefficients which can recover the signal with the minimum value of entropy [47]. As explained in [46], a signal becomes more disordered and less structured when the entropy value is high. Hence, minimizing the value of entropy has the effect of improving the structured information from the original signal and thus enhancing the impulsiveness (kurtosis) for the MED filter output signal. The process of forming a MED filter is outlined below [27].

Generating a FIR filter f with L coefficients:

$$y(n) = \sum_{l=1}^L f(l) v(n-l) \quad (2.9)$$

Where L is the length of the deconvolution filter f , v is the input signal and y is the output signal. The deconvolution filter f can inverse the structural filter h that achieves:

$$f * h(n) = \delta(n - l_m) \quad (2.10)$$

The inverse filter f can be causal with the delay l_m .

2.3.3.2 Empirical mode decomposition (EMD)

EMD method is a self-adaptive decomposition method that assumes that any signal is composed of several intrinsic modes of oscillations [48]. According to the algorithm of EMD, the raw signal $x(t)$ can be reconstructed as follows:

$$x(t) = \sum_{i=1}^n c_i + r_n \quad (2.11)$$

where c_1 to c_n represents each intrinsic mode function (IMF), and r_n is the final residue that shows the mean trend of $x(t)$.

Due to the ability of EMD in decomposing the non-stationary vibration signal into several IMFs, which are themselves stationary, a number of EMD-based signal processing techniques have been proposed for bearing fault detection. Through applying EMD, this method divides the raw vibration signal into three parts: noise-only part, signal-only part and trend-only part. The bearing fault can be clearly identified by using kurtosis analysis to the noise-only part of the raw signal. In [48], the EMD method was utilized with autoregressive (AR) model for the fault feature extraction of the roller bearings. In [49], the EMD method was combined with Hilbert transform to the envelope analysis for the fault detection of roller bearings. In [50], a signal processing procedure, which applied computer order tracking, EMD and Teager Kaiser energy operator (TKEO), was proposed for bearing fault detection during the run-up of a gearbox. In [51], the technique of EMD was employed with Fast Fourier Transform (FFT) for accurately capturing the bearing fault defect frequencies. In [52], EMD was applied for choosing an appropriate resonant frequency band for characterising feature frequencies of bearing faults before the envelope analysis. In [53], an EMD-based method was presented with the aim of removing the machine noise that corrupted the bearing fault signal.

2.3.3.3 Spectral Kurtosis (SK)

Kurtosis is an efficient indicator for measuring the impulsiveness of a vibration signal and has an expression as [54]:

$$kurtosis(x) = \frac{E\{ (x - \mu)^4 \}}{\sigma^4} \quad (2.12)$$

Where μ is the mean of the signal x , σ is the standard deviation of the signal x , and E stands for the expectation operation.

The application of spectral kurtosis (SK) to the condition monitoring of rotating machines was first proposed by Antoni and Randall [55]. SK is used as a defect indicator for detecting incipient faults that generate impulse-like signals, and for indicating their locations in the frequency domain. In addition, Antoni and Randall [56] also suggested that SK technique could be further used as a band-pass filter for filtering out undesired stationary noise, and the demodulation process (envelope analysis) could then be applied to the filtered signal for extracting the mechanical signature of the bearing fault.

SK was estimated based on the short-time Fourier transform (STFT) in [57] that can be expressed as follows:

$$K(f) = \frac{\langle |X(t, f)|^4 \rangle}{\langle |X(t, f)|^2 \rangle^2} - 2 \quad (2.13)$$

Where $X(t, f)$ is the time/frequency envelope of the original signal and the square of its amplitude means the power spectrum values at each time. $\langle \cdot \rangle$ is the time-averaging operator.

The procedure for the STFT based SK in bearing fault detection is presented in Fig. 2.10. The STFT of a bearing fault signal is obtained by moving a window (Hanning window in this case) along the record and drawing a series of amplitude spectra for each position of the window and then the resulting time/frequency envelope $H(t, f)$ could be obtained. The kurtosis value can be calculated by taking the fourth power of $H(t, f)$ at

each time and averaging its value along the record, then normalizing it by the square of the mean square value.

As the SK value varies with both the frequency f and frequency resolution Δf , a representation of SK in the plane $(f, \Delta f)$ is required for finding the maximum value of SK. However, the full exploration of each SK value from the $(f, \Delta f)$ plane is infeasible as it is time-consuming and thus hard to be applied in industrial applications. For solving the issues mentioned above, the Fast Kurtogram (shown in Fig. 2.11) was presented in [58] as a further development of the SK method for efficiently computing the SK values over a dyadic grid in the $(f, \Delta f)$ plane. The performance of the Fast Kurtogram and the "Full" Kurtogram are compared in Fig. 2.12. It demonstrates that the Fast Kurtogram (a) has a similar result to the "Full" Kurtogram (b) in picking the frequency band with high kurtosis, and it significantly reduces the required CPU load.

In several publications, the SK technique was combined with other techniques for the bearing fault diagnosis. In [59], the Fast Kurtogram was utilized with genetic algorithms to select the optimum band-pass filter. This genetic algorithm-based spectral kurtosis has a strong ability for optimizing the parameter with minimal constraints on the center frequency and bandwidth, and the speed of the Fast Kurtogram rapidly give better initial analysis parameters for the genetic algorithm. In [60], a hybrid signal processing method was presented, which combined SK technique and ensemble empirical mode decomposition (EEMD), for the faulty bearing signal recovery from intense noise. The result showed that the hybrid approach can recover faulty bearing signal from large noise and increase the kurtosis of analyzed signal to a remarkable degree. In [46], the techniques of minimum entropy deconvolution (MED) and AR-based linear prediction were employed with the SK for improving the result of envelope analysis and aiding the fault diagnosis.

The original SK technique was also further developed by some researchers for

enhancing its fault detection abilities in bearing diagnosis. Liang and Wang [54] presented an adaptive spectral kurtosis technique for the bearing fault detection. The improvements of this method is the adaptive determination of the bandwidth and center frequency for the SK based bandpass filter through right-expanding a given window along the frequency axis and merging it with its subsequent neighboring windows for maximizing the kurtosis. Compared to the SK method, this adaptive SK technique can optimize the filter bandwidth and reliably locate the filter center frequency, and thus provide a better amplitude demodulation result. Lei et al. [61] adopted wavelet packet transform (WPT) as the filter of Kurtogram with the purpose of overcoming the drawbacks of STFT or finite impulse response (FIR) filters. Chen et al. [62] proposed an improved spectral kurtosis method based on adaptive redundant multiwavelet packet. This new approach could improve the accuracy of frequency band selection and enhance the ability of rotating machinery fault detection.

Arguing at the temporal-based SK techniques does not deal well with the cases with the appearance of strong non-Gaussian noise, some researchers utilizes the kurtosis of the spectrum as the bearing fault indicator. Barszcz and Jabłoński [63] proposed a novel approach called Protrugram which selects the kurtosis of narrowband envelope spectrum rather than the kurtosis of band pass filtered temporal signal. The Protrugram method has the advantage of detecting the bearing fault signal in the presence of high-level noise. Wang et al. [64] proposed an enhanced Kurtogram by using the technique of WPT as the filter structure and the kurtosis of the power spectrum of the envelope of the signals as the fault indicator.

2.3.4 Bearing faults feature extraction techniques

2.3.4.1 Time domain methods

Time domain feature extraction methods directly utilize certain statistical parameters of the time waveform for distinguishing between good and faulty bearings. Common

statistical parameters including root mean square (RMS), stand deviation (σ), crest factor, and kurtosis, and their corresponding expressions are listed below [26]:

$$\text{Root mean square:} \quad RMS = \sqrt{\frac{1}{N} \sum_{i=1}^N (x(i))^2} \quad (2.14)$$

$$\text{Standard deviation:} \quad \sigma = \sqrt{\frac{1}{N} \sum_{i=1}^N (x(i) - \bar{x})^2} \quad (2.15)$$

$$\text{Crest factor:} \quad CF = \frac{peak}{RMS} \quad (2.16)$$

$$\text{Kurtosis:} \quad kurtosis = \frac{\frac{1}{N} \sum_{i=1}^N (x(i) - \bar{x})^4}{\sigma^4} \quad (2.17)$$

RMS is the simplest feature extraction parameter in the time domain. It measures the RMS average of the overall vibration level in the whole time domain and compares the result with established reference values for determining the bearing status. Although this parameter is simple and quick, several limitations were presented in [16]: RMS could only be useful in very simple configurations and the bearing damage in an early stage is difficult to recognize by RMS. Another parameter for testing the bearing condition is crest factor by measuring the ratio of the peak value to RMS. As the defect occurs in the bearing, the level of the peak value in time domain increases more rapidly than the RMS level due to the resulting short bursts, which means crest factor is relatively sensitive to the bearing failure at an early stage. However, according to [65], this indicator is easily affected by the interference from other vibration sources. Kurtosis was firstly proposed in [66] for rolling element bearing fault diagnosis. The kurtosis is sensitive to the impulsive signal and shows a very low value for the stationary signal. In general, the kurtosis value of a good bearing with the Gaussian distribution is close to 3. Thus kurtosis value greater than three could indicate the impending failure [67].

Based on test results and conclusions in [16] via applying the time domain feature extraction methods, the aforementioned time domain fault indicators could only

successfully detect the bearing defects where significant impulsiveness occurs, while it is hard to extract bearing fault information when bearings are subjected to the cases of overload or loss of oil.

Another limitation of these time domain indicators is that the original vibration signal is masked by the background noise and other components interactions that lead to the non-consistent pattern for all the time domain indicators [26].

2.3.4.2 Frequency domain methods

Frequency domain methods are based on spectrum analysis for analyzing either the whole frequency domain or the certain frequency components of interest, and then extracting the bearing fault feature [5]. Spectrum analysis can easily identify and isolate specific frequency components for comparison and analysis [5].

In the aspect of bearing diagnosis, the interaction of defects in rolling element bearings generates pulses, and these pulses will excite the natural frequencies of bearing elements or the housing structures. The vibration energy level at these frequencies may then increase [67].

Constant-percentage-bandwidth (CPB) spectrum comparison is one of the commonly used frequency domain methods for extracting the bearing fault information. Based on [65], constant-percentage-resolution in the frequency axis not only provides a sufficiently wide frequency range for detecting bearing faults, but also allows the detection of other low-frequency defects.

2.3.4.3 Time-Frequency Domain methods

Time-frequency analysis is a powerful tool for extracting the bearing fault feature. While the frequency domain methods fail in analyzing the non-stationary signal,

time-frequency analysis, which processes the vibration signal in both time and frequency domains, could better reveal the transient fault feature for more accurate detection. Primarily, three time-frequency methods have been utilized for bearing diagnosis: short-time Fourier transform (STFT) [68], Wigner-Ville Distribution (WVD) [69] and wavelet analysis [27].

The principle of STFT is dividing the whole vibration signal into segments with short-time window and using the Fourier transform to each segment [5]. The main drawback of the STFT is that it provides a constant resolution to all frequencies, that means if a wide window is used for obtaining good frequency resolution, it is impossible to get a good time resolution for analyzing high-frequency components [69].

WVD is another time-frequency representation obtained by transforming the autocorrelation with respect to the time-lag variable [27]. Although WVD has good concentrations in the plane of time-frequency, it may mislead the signal analysis due to the possibility of negative energy levels and non-physical interference [26].

Compared to the previous two time-frequency domain methods, wavelet analysis is more efficient in dealing with non-stationary signal, as the multi-scale analysis could be provided in wavelet analysis through dilating or translating the wavelets in time [69].

2.3.4.4 Envelope analysis

Envelope analysis is regarded as one of the most efficient methods in bearing diagnosis [27]. The characteristic defect symptoms are apt to be recognized by envelope spectrum in comparison with frequency spectrum, as the wide distribution of energy of the impulse response leads to very small values at the fault repetition frequencies, while the fault impulses are amplified by structural resonances in higher frequency bands. Therefore, analyzing the envelope signal is more effective in obtaining the desired diagnostic information [36].

The Hilbert transform has been used to carry out the amplitude demodulation in

envelope analysis [27] (Fig. 2.13). By applying Hilbert transform to the vibration signal $x(t)$ to calculate its analytic form, the imaginary part of the analytic signal is obtained as:

$$H[x(t)] = \frac{1}{\pi} \int_{-\infty}^{\infty} x(\tau) / (t - \tau) d\tau \quad (2.18)$$

The analytical signal $z(t)$ can be constructed as:

$$z(t) = x(t) + jH[x(t)] \quad (2.19)$$

Then $e(t)$, which is the envelope of $z(t)$, is calculated as:

$$e(t) = \sqrt{x^2(t) + H^2[x(t)]} \quad (2.20)$$

The performance of the envelope analysis is further improved by squaring the envelope signal. This is because the squaring process has the benefit of enhancing the bearing frequency components from envelope spectrum and degrading the background noise [31].

2.4 Planetary gearbox fault diagnosis

2.4.1 Gear fault diagnosis

As summarized in [70], vibration signals from the planetary gearbox are complicated, and the gear fault detection and diagnosis impose several challenges. a) As the multiple planet gears mesh simultaneously with the ring gear and the sun gear, and the vibrations with a different meshing phases couple with each other, parts of the vibrations are neutralized or canceled. b) The time-varying transmission path may attenuate the signal from the faulty components. c) The distribution of frequency components for the vibration signals in a planetary gearbox are different from a fixed-axis gearbox, which may mislead the fault feature extraction. d) Low-frequency fault characteristics are difficult to recognise due to often intense background noise.

There has been extensive research on condition monitoring and fault diagnosis of

gears in planetary gearboxes aimed at overcoming the issues above. McFadden and Howard [71] applied the technique of time synchronous averaging (TSA) for diagnosing the localized defects in the planet gear and the sun gear. They showed that the signal averages of the planet gears and the sun gear could successfully detect the artificially seeded damage in sun gear and planet gear tooth. However, the challenge of TSA technique for the planetary gearbox gear fault detection were also mentioned in [72], the vibration signal of the faulty planet gear may be masked by the vibration signal of the other planet gears due to the variable transmission path between the fault location and the location of the externally mounted sensor. Feng et al. [73] presented a joint amplitude and frequency demodulation method for gear fault diagnosis of planetary gearboxes and proved its effectiveness in the detection of artificially seeded planet pitting faults and naturally developed gear wear for both the ring gear and planet gear. Feng et al. [74] combined the methods of ensemble empirical mode decomposition (EEMD) and energy separation for detecting the sun gear faults of the planetary gearbox. Barszcz and Randall [75] applied the spectral kurtosis based technique to the ring gear tooth crack detection of a planetary gearbox, this method could detect the existence of tooth crack several weeks before the gear fault. Yu et al. [7] combined wavelet analysis with TSA technique to the collected fault signal for further optimizing the planet gear fault detection. Lei et al. [76] proposed an adaptive stochastic resonance method (ASR) for the defects feature extraction of the sun gear. The ant colony algorithms determine the stochastic resonance parameters. In [77], Feng and Liang presented a time-frequency analysis method based on the algorithm of the adaptive optimal kernel (AOK), for recognizing the time-varying gear fault features in the non-stationary signal. A wide range of gear faults in planetary gearbox could be effectively identified, which include the localized faults and distributed faults for both sun gear fault and planet gear. Feng and Zuo [78] analyzed the gear fault signal via employing the torsional vibration signal instead of the acceleration signal, as the torsional signal is free from the amplitude modulation effect caused by the time-varying transmission path in theory.

The results demonstrated that both the single gear faults and multiple gear faults could be clearly detected. Feng and Liang [79] applied the technique of iterative atomic decomposition thresholding (IADT) method for suppressing the background noise and enhancing gear characteristic frequencies in the gear fault detection of the planetary gearbox. Hong and Dhupia [80] proposed a time domain approach for the gear fault detection in the planetary gearbox. This method combines the fast dynamic time wrapping (Fast DTW) and the correlated kurtosis (CK), fast DTW are utilized for extracting the periodic impulse excitations generated by the defective gear tooth and the CK technique is used for identifying the defect location of the gear. Smidt and Ryan [13] mounted an internal sensor on the planet carrier for data collection and applied the TSA technique to the internal vibration signal for the fault detection of planetary gears. The results showed that the most distinct advantage of internal sensor-based measurement was that the raw signal can be directly converted to the useful damage indicator for gear faults, such as kurtosis or root-mean-square (RMS) values, without any preprocessing steps.

2.4.2 Bearing fault diagnosis

As with gear diagnostics in planetary gearboxes, bearing diagnostics also reveal some unique challenges. As explained in [81], this is because the bearing fault vibration signals are strongly masked by gear signals. In addition, the signal from planet gear bearing is transmitted through the ring gear to the fixed external sensor via a time-varying transmission path which means that the fault signal is subject to both noise contamination and modulation.

In [82], the techniques of self-adaptive noise cancellation (SANC) and discrete random separation (DRS) were applied for separating the bearing fault signals from gear signals in the planetary gearbox. Thus, the bearing signals could be further extracted by using envelope analysis. Three cases of different bearing faults (rolling element faults

on input pinion support bearing, rolling element faults on planet gear bearing, inner race spall on input pinion small end bearing) were tested and the result showed the characteristic fault frequencies could be successfully obtained in the envelope spectrum for previous two cases, while the envelope analysis did not reveal any frequency components related to BPFI in the third case. The possible reason could be that BPFI may only be noticeable at the early stage when small pits excite sharp impacts. In [83], Sawalhi and Randall utilized a series of techniques, such as power spectral density (PSD) comparisons, CPB, SK, envelope analysis, order tracking and autoregressive model (AR), for the planet bearing fault detection in helicopter gearbox. The results showed that the inner race fault could be recognized with envelope analysis. In [84], Jiang et al. proposed a denoising technique based on the adaptive Morlet wavelet and singular value decomposition (SVD), for the feature extraction of wind turbine vibration signal. They showed that the proposed method could extract the weak outer race fault features submerged in strong background noise. In [47], Barszcz and Sawalhi applied the technique of Minimum Entropy Deconvolution (MED) for improving the performance of bearing fault diagnosis. Wang et al. [85] integrated the EEMD (ensemble empirical mode decomposition) with the independent component analysis (ICA) techniques for the support bearing fault detection in wind turbine gearbox. In [14], Smith et al. applied an internal accelerometer for the planet gear bearing diagnosis. The result showed that the internal sensor had the potential superiority in detecting the inner race fault, but it also presented the limitation of this novel sensor mounting location that the internal vibration signal is more easily affected by the electromagnetic interference (EMI) from due to the use of slip ring for signal transmission. These EMI signals mainly come from the variable frequency drive (VFD), and the frequency components are determined by several key parameters, such as switching frequency, input shaft rotating frequency and power frequency. These EMI signals strongly affect the bearing fault detection performance of some signal processing techniques.

2.5 Summary

In this chapter, background information for the bearing fault diagnosis of the planetary gearbox is reviewed. As the vibration based condition monitoring technique is the main focus of this project, a wide range of existing advanced signal processing techniques is specifically introduced in this chapter as well as their applications in bearing fault diagnosis.

For fault diagnosis in planetary gearboxes, while researchers proposed a number of effective signal processing procedures for the gear faults detection, there is still lack of valuable techniques for bearing fault detection in planetary gearbox [81]. Thus, it is essential to develop a more efficient signal processing algorithm for faults information recognition in planet bearings, which is the primary target of the thesis and further details would be presented in the following chapters.

CHAPTER 3 METHODOLOGY

3.1 Introduction

As the main goals for this study were the investigation of the internal sensor-based measurement for planetary bearing diagnosis and resolving the electromagnetic interference (EMI) issue generated from variable frequency drive (VFD) of the test rig, a systematic and efficient methodology is required. In this chapter, the methodology for achieving the objectives is presented, and the reasons for selecting the described steps and techniques are also explained. For the rest of this chapter, section 3.2 gives an overview of the methodology in this study. The details of two main tasks in methodology (experimental setup and data analysis) are provided in section 3.3 and section 3.4.

3.2 An overview of the methodology

The flowchart of the methodology is plotted in Fig. 3.1. In particular, the methodology primarily contains two tasks including (a) experimental setup and vibration data collection (section 3.3), and (b) data analysis for resolving EMI issues and developing a signal processing procedure for the internal sensor-based measurement (section 3.4). Experimental setup includes test equipment preparation, bearing fault seeding and test parameters setting. The step of data collection can then be implemented after the experimental setup. About the data analysis, as the previous research [14] showed that the bearing fault signal collected by an internal sensor was strongly masked by the EMI signal and bearing fault features were difficult to be directly extracted in some cases. Thus, one of the main tasks is to filter out the EMI signal and other deterministic components from the raw vibration signal. Another task is to develop a

valid demodulation band selection method in dealing with the EMI contaminated vibration signal, as the envelope analysis is a crucial step for bearing fault extraction in planetary gearbox and it has a major challenge in the selection of the optimal demodulation band in harsh EMI environment. Combined with the experimental results of the aforementioned two tasks in data analysis, a hybrid signal processing strategy is proposed for internal sensor-based measurement and the validity of this presented signal processing procedure could be further tested by checking if the bearing fault features could be successfully extracted from the collected vibration data.

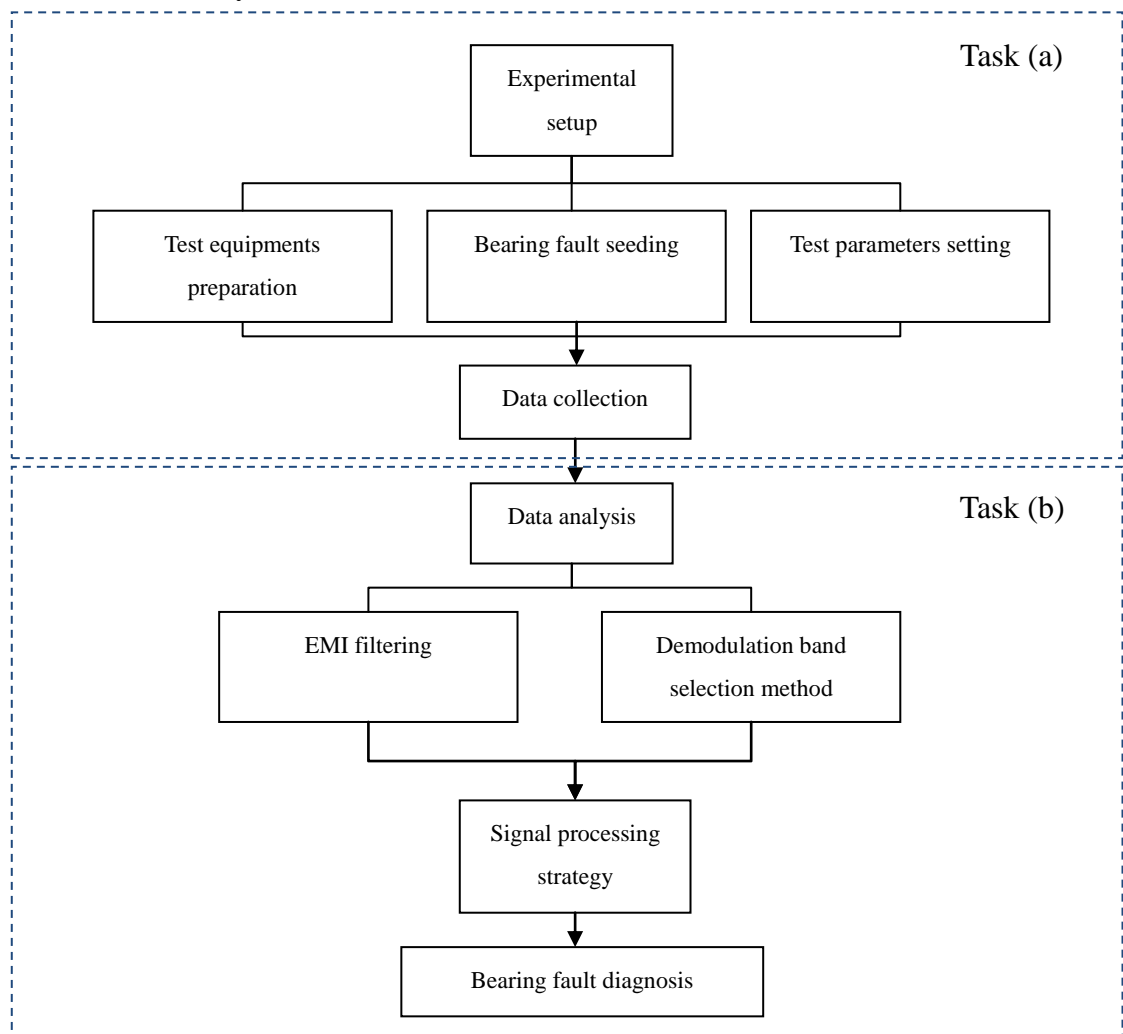


Fig. 3.1 The flowchart of methodology in this study

3.3 Experimental setup and data collection

In order to conduct the experiments for internal accelerometer based measurement and collect the vibration signal for further signal processing step, several preparatory work were required to be implemented. The primary aim of this section is illustrating the crucial steps for experimental setup, which include test equipments preparation, bearing fault seeding and test parameter setting. In the section 3.3.1, the basic information of experimental facilities, which include planetary gearbox test rig, data collection system and the novel sensor mounting location, are detailed introduced, and the purposes are also presented. The bearing fault seeding information is presented in section 3.3.2. The work of test parameter setting would be introduced in later chapters.

3.3.1 Test equipment preparation

3.3.1.1 Planetary gearbox test rig

The UNSW gearbox test rig was designed by Sweeny for the purpose of investigating misalignment effects to gear vibration. The basic layout of the test rig is presented in Fig. 3.2. The speed of the driving shaft was controlled by a 3 Phase AC induction motor with soft-start frequency controller. This rig had the limitations of the running speed of 12 Hz and the torque loads of 100 Nm. The frequency controller also allowed the speed of the rig to be accurately modulated during operation. A hydraulic system (hydraulic motor and hydraulic pump) was utilized in this rig for providing a resistance torque to the gearbox. The applied torque load was for accurately simulating the operational gearbox in industrial cases, which ensured the adequate load on the gears teeth and bearings in the system, and the torque load induced vibration and transmission error could be monitored for the machine faults detection.

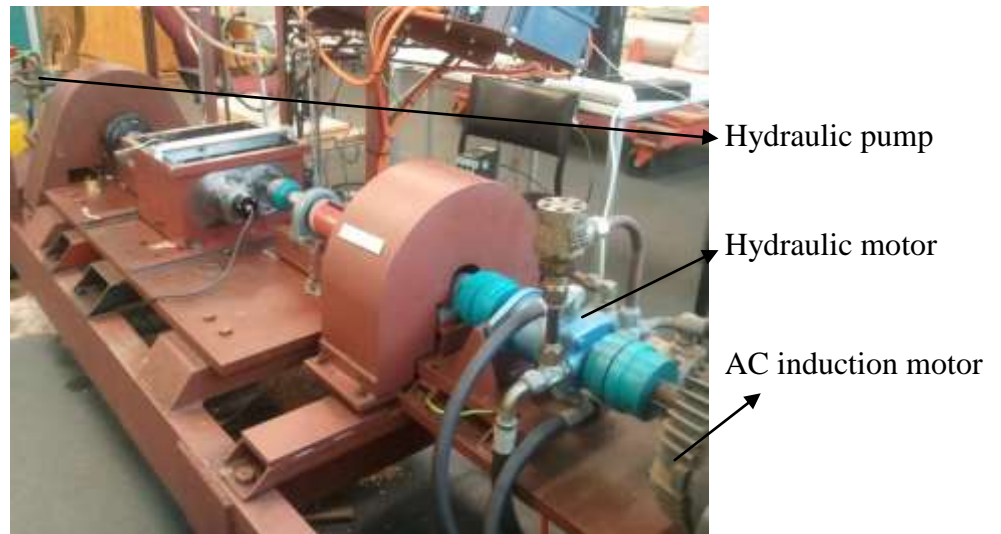


Fig. 3.2 UNSW gearbox test rig

As shown in Fig. 3.3, the test control panel was utilized for adjusting shaft speeds and torque loads. The input shaft speed was controlled by the variable frequency drive (VFD) which was connected with the AC induction motor. The torque load could be adjusted by the valves from hydraulic systems, and the torque range is 0-100 Nm.

Variable frequency drive



Fig. 3.3 Test rig control panel

The non-hunting tooth planetary gearbox was designed by Andrew Bligh, and the vibration data collected in this gearbox would be further introduced and analyzed in chapter 6 for validating the effectiveness of the proposed method 'Kurtrugram'. A

schematic of the planetary gearbox is shown in Fig. 3.4. It consisted of the one-stage parallel shaft and one-stage planetary (details are presented in Fig. 3.5). The parallel shaft stage included a pinion gear of 32 teeth meshing with a large spur gear of 90 teeth, which was connected directly to the planet carrier. The planetary stage included an 80 tooth ring gear, three 20 tooth planetary gears, and a 40 tooth sun gear to give the planetary stage a gear ratio of 1:3. The ring gear was fixed while the three planet gears meshed with the ring gear and the sun gear simultaneously. An overall gear ratio of the gearbox was 1:1.0667. The slip ring (shown in Fig. 3.4) was for the transmission of vibration signal collected by internally mounted the accelerometer. Grease lubrication was used in the gearbox to allow the slip ring to be placed inside the housing. It is worth noting that, due to this non-hunting tooth design, it is difficult to establish an average meshing pattern for individual meshing pairs through using the conventional signal processing techniques for gear faults detection. Because the meshing pairs occur at exactly the same point in each cycle of the planetary stage.

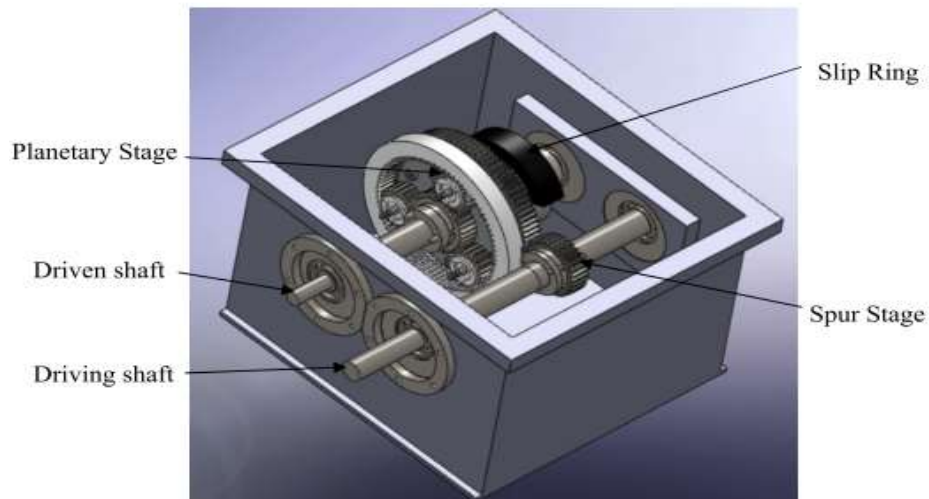
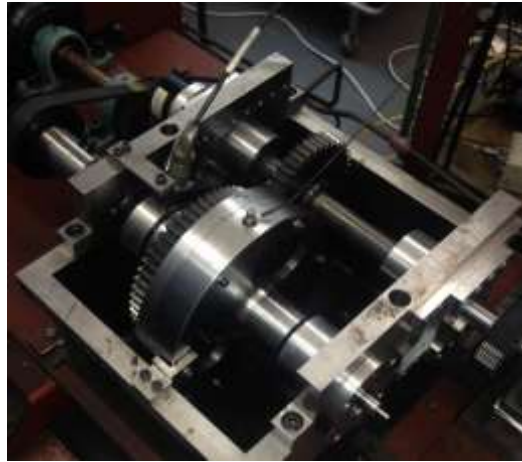


Fig. 3.4 CAD model of the planetary gearbox

Another planetary gearbox for testing was mainly designed by Mr Vincenzo Carnevale, and this hunting tooth planetary gearbox is plotted in Fig. 3.6. The vibration data collected in this gearbox would be further introduced and analyzed in chapter 7 for

testing the fault detection performance of the hybrid signal processing procedure. Similar as the non-hunting tooth planetary gearbox, this gearbox also consisted of the one-stage parallel shaft and one-stage planetary. The parallel shaft stage included a pinion gear of 42 teeth meshing with a large spur gear of 55 teeth, which was connected directly to the planet carrier. The planetary stage included an 80 tooth ring gear, three 23 tooth planetary gears, and a 34 tooth sun gear. The ring gear was fixed while the three planet gears meshed with the ring gear and the sun gear simultaneously. An overall gear ratio of the gearbox was 1:2.56. Differing from the planetary gearbox shown in Fig. 3.4, this one solved the non-hunting tooth problem by the changes of tooth number for gears (except the ring gear). In addition, for this gearbox, the center distance between the input and output shafts could be adjusted in a certain range, which allowed the experiments to be conducted in more variety of gear arrangements.

(a)



(b)

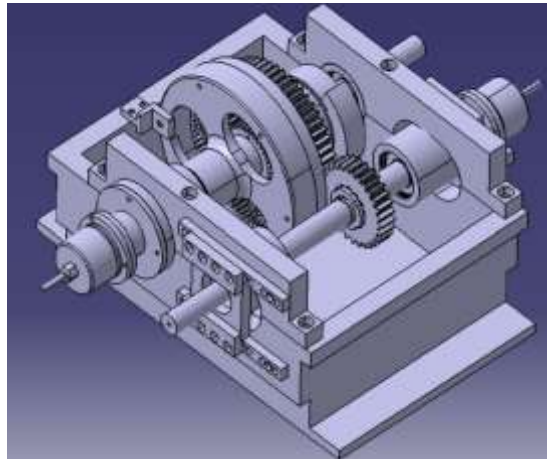


Fig. 3.5 (a) Hunting tooth planetary gearbox; (b) CAD model of the planetary gearbox

3.3.1.2 Data collection system

The Brüel & Kjær 4394 IEPE-type accelerometer (Fig. 3.7 (a)) was used for vibration measurements. This accelerometer has a built-in CCLD preamplifier, and it has the advantage of low sensitivity to the environmental influences (such as temperature variation). Two Brüel & Kjær 4394 IEPE-type accelerometers were utilized for the vibration data collection. One was mounted on the planet carrier in the axial direction for investigating the potential advantages of internal vibration measurements. Since the accelerometer rotated with the planet carrier, a Michigan Scientific B6-2 slip ring (Fig. 3.7 (b)) was used for transmitting the internal vibration signal. Another sensor was externally mounted for presenting the performance of external sensor-based measurement.

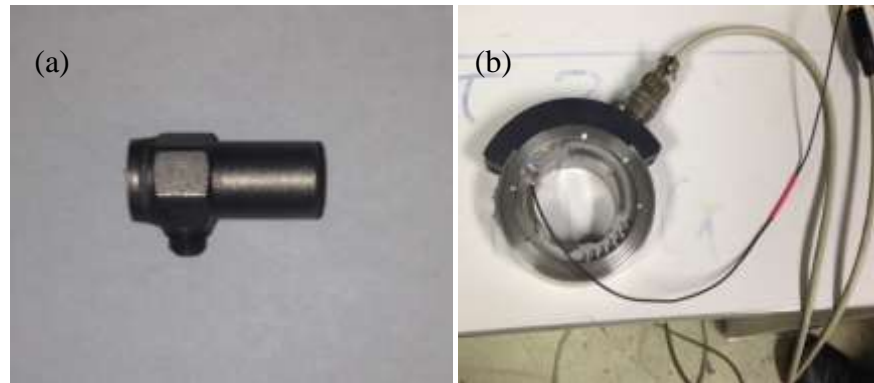


Fig. 3.6 (a) Brüel & Kjær 4394 IEPE-type accelerometer; (b) Michigan Scientific B6-2 slip ring

The Hiedhan 426-36000 shaft encoder was installed at the shaft end of the input shaft for accurately tracking the rotating speed. A torque transducer was mounted on input shaft between the hydraulic motor and gearbox housing. This torque load tracking was for regulating the hydraulic control valve and setting the torque value during the

experiment. The plots of shaft encoder and torque transducer are presented in Fig. 3.8.

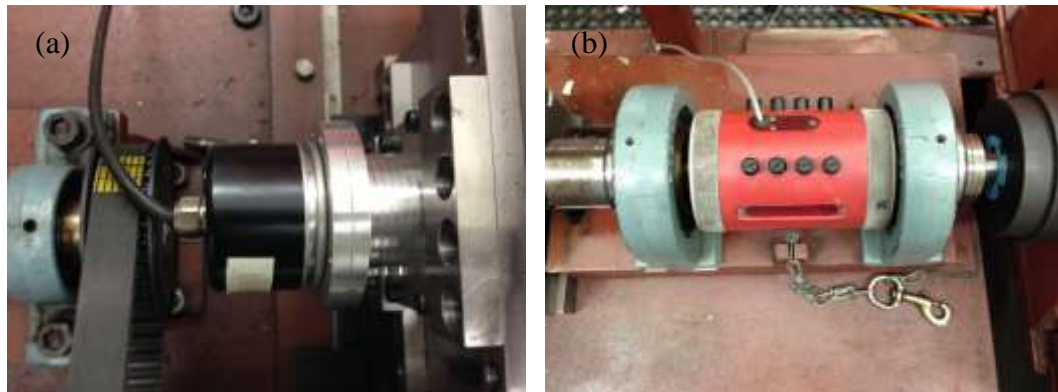


Fig. 3.7 (a) Hiedhan 426-36000 shaft encoder; (b) Torque transducer

As shown in Fig. 3.9, Brüel & Kjær PULSE analyzer (PULSE front-end) was connected to a laptop running Brüel & Kjær Labshop software for data recording. The recorded vibration data included the vibration signals collected from the internal sensor and external sensor, and the tacho signal collected by the shaft encoder. These recorded data were then exported to MATLAB for further signal processing. The signal obtained from the torque transducer could be displayed through using the Westlands S2 signal conditioner (shown in Fig. 3.9).

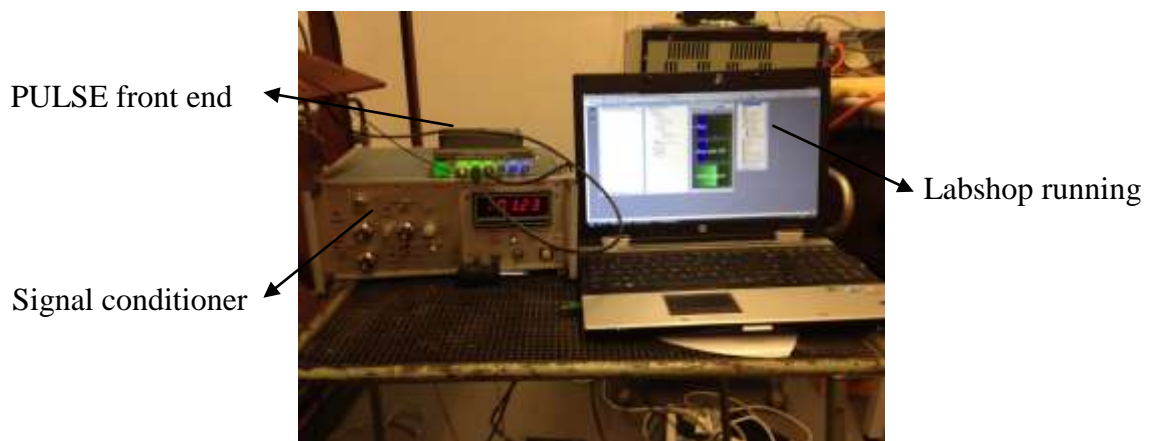


Fig. 3.8 Planetary gearbox test rig data capture system

3.3.1.3 Sensing by using internal vibration sensor

As briefly introduced in section 2.4.1, the idea of using an internal sensor for vibration data collection and machinery fault diagnosis was firstly presented in [13]. Smidt and Ryan mounted an internal accelerometer on the planet carrier (shown in Fig. 3.10) for data collection and applied the TSA technique to the collected internal vibration signal for the fault detection of the planetary gears. The results showed the advantage of internal sensor-based measurement was that the raw signal could be directly converted to the useful damage indicator for gear faults, such as kurtosis or root-mean-square (RMS) values, without any preprocessing steps. However, there are also some restrictions of internal measurement, the gearbox is required to be specialized modified for installing accelerometer internally and these modifications may reduce the strength of the shaft and generates the possibility of leakage of the gearbox lubricant.

The internal sensor-based measurement was investigated in for the bearing diagnosis in planet gear. Smith et al. [14] utilized an internally-mounted accelerometer for identifying planetary bearing defects in the non-hunting tooth planetary gearbox that is previously introduced in section 3.3.1.1. Also, the traditional externally mounted sensor was applied as a comparison. The sensor locations are shown in Fig. 3.11.

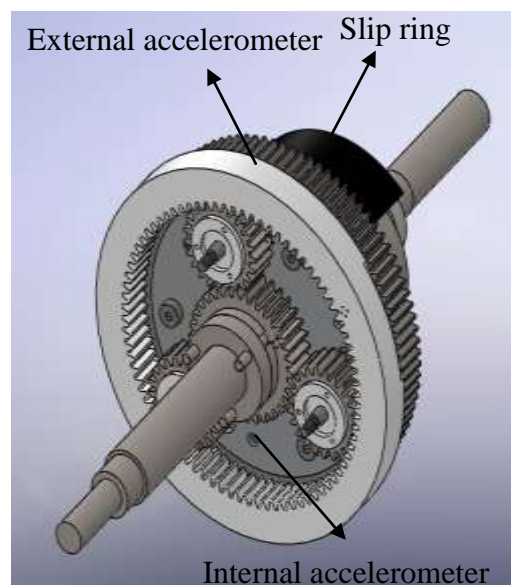
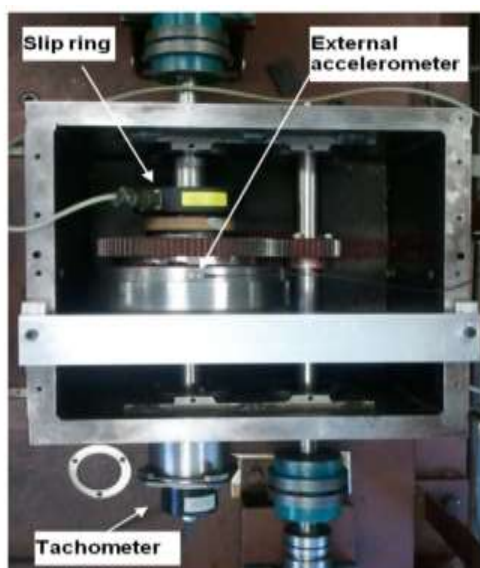


Fig. 3.9 (a) Top view of UNSW planetary gearbox [14]; (b) A CAD model for showing the locations of transducers

As the study in this thesis is a further investigation of the internal sensor-based measurement in bearing faults detection of planetary gearbox, the mounting location of the internal accelerometer in both the non-hunting tooth planetary gearbox and hunting tooth planetary gearbox is similar as the one in [14]. Also, another accelerometer is fixed on the gearbox casing for externally collecting the vibration signal.

3.3.2 Bearing faults seeding

As illustrated in [87], there are three main types of fatigue in the bearing: fatigue spalling, fatigue pitting and surface distress. This study is mainly focused on the bearing fault detection of spalling in inner and outer races of the rolling element bearing, which appears as cavities with a depth of 20-100 μm [87]. In order to simulate the spalls in both the inner race and outer race, the technique of electric spark erosion was used for producing the rectangular gaps in both the inner and outer races. The plots in Fig. 3.12 are examples of showing the simulated bearing faults in part of the study (chapter 6). More descriptions of the bearing information and the defects information in each test are presented in chapters 5 and 6.



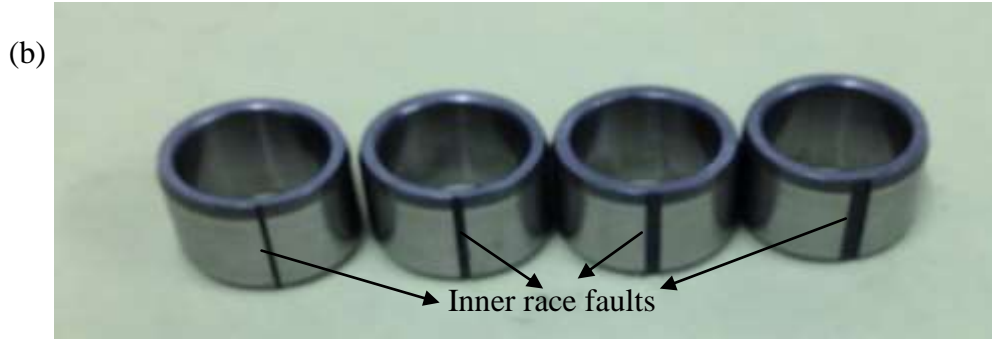


Fig. 3.10 (a) Simulated outer race fault; (b) Simulated inner race fault

3.4 Data analysis

Data analysis in this study is for extracting the bearing faults features from the collected vibration signal via using a series of signal processing techniques. Based on the results in [27,83,88-89], as the bearing fault signal in planetary gearbox is strongly masked by the background random noise and the deterministic signal, an effective bearing diagnosis procedure should contain three crucial steps: a). Preprocessing step for filtering out the deterministic components in the raw signal. b). Step for enhancing bearing fault related impulsive signal. c). Step for extracting bearing fault signature. The basic layout of this procedure is presented in Fig. 3.13.

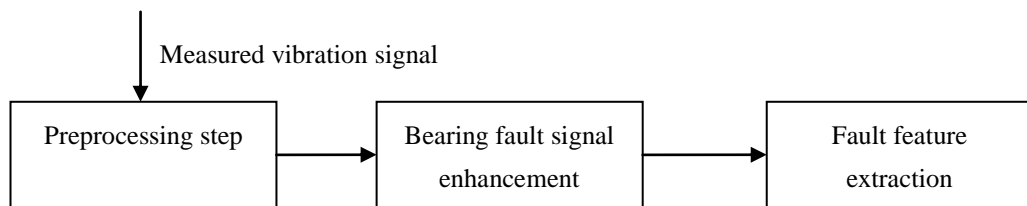


Fig. 3.11 Layout of the bearing fault detection procedure

For the internal sensor-based measurement, the collected vibration signal is strongly corrupted by EMI signal from VFD and this EMI signal makes the bearing fault features more difficult to be extracted [14]. Thus, the aforementioned basic bearing diagnosis procedure needs to be further updated for diagnosing the bearing faults under the condition of intense EMI. For the preprocessing step (introduced in section 3.4.1), some

efforts are made for the selection of EMI filtering technique and the experimental results are presented in chapter 4. For the step of bearing fault signal enhancement (introduced in section 3.4.2), a novel spectral kurtosis (SK) based technique 'Kurtrugram' is proposed in order to select the optimal demodulation band accurately for the bearing fault signal corrupted by the EMI. The experimental results are presented in chapter 5. After the completion of steps above, a new signal processing procedure (introduced in section 3.4.3) could be utilized for comprehensively investigating the bearing faults detection performance of the internal sensor-based measurement. The experimental results are presented in chapter 6.

3.4.1 EMI signal filtering

In this part, the components of EMI signal are clarified by analyzing the spectrum and the power spectrum of the collected vibration data with the appearance of intense EMI generated from the VFD. Since the EMI interference in the signals manifested itself most clearly as families of discrete frequency components around harmonics of the VFD switching frequency (shown in chapter 4), applying some sort of discrete/random separation technique to remove the EMI seems appropriate. Several advanced signal processing techniques, such as DRS, Cepstrum editing and Cepstrum pre-whitening, are also implemented to the testing signal for comparing their performances in removing the EMI components from the original signal. The reason for selecting aforesaid techniques is due to their good performance in removing the deterministic components as presented in [41, 43, 90]. More details of this part are given in chapter 4.

3.4.2 Optimum demodulation band selection

In this part, a simple demodulation band selection method 'Kurtrugram' is proposed with the aim of accurately extracting bearing fault-related impulsive content from

vibration signals contaminated with strong EMI. this Kurtrugram takes advantage of core ideas from both the techniques of Fast Kurtogram and Protrugram: the overall process is basically identical to the Protrugram, but the fault indicator – the kurtosis of the envelope (time) signal – is taken from the Fast Kurtogram. The Kurtrugram is then applied to vibration signals obtained from the non-tooth hunting planetary gearbox with planet bearings seeded with inner and outer race faults. Results from the Fast Kurtogram and Protrugram methods are also included for comparison. More details and experimental results are presented chapter 5.

3.4.3 A hybrid signal processing procedure

Based on the experimental results from sections 3.4.1 and 3.4.2, a hybrid signal processing approach is developed in this part with the aims of solving the problems raised by the internal sensor-based measurement and further investigating the performance of internal sensor-based measurement in planetary bearing faults detection, This approach combines several advanced signal processing techniques, such as Cepstrum whitening, minimum entropy deconvolution (MED), Kurtrugram and envelope analysis. Cepstrum pre-whitening (discussed in chapter 4) is selected as the first step for removing the discrete frequencies from the raw vibration signal. Minimum entropy deconvolution (MED) is then used to remove the effect of the transmission path and to enhance the bearing fault related impulsiveness. Since the well-known Fast Kurtogram is easily affected by the large spectral kurtosis (SK) value associated with the electrical interference (discussed in chapter 5), the selection of the demodulation band may be confused by the results of the Fast Kurtogram. Instead, the novel method Kurtrugram is utilized as the third step for the selection of the demodulation band under the condition of intense EMI. Envelope analysis is the final step for the extraction of bearing fault information in the envelope spectrum. The vibration data collected from tooth hunting planetary gearbox is utilized for validating the effectiveness of the presented signal processing procedure for the internal sensor-based measurement, and

an externally mounted sensor is also applied in this study as a comparison. More details and experimental results of this signal processing procedure are presented in chapter 6.

3.5 Summary

This chapter is mainly focused on the methodology in this study, which mainly contains two parts: experimental setup and data analysis. For the experimental setup, the basic information of the test equipments, such as planetary gearbox test rig, data collection system and the novel sensor mounting location, are detailed described, and their purposes are also explained. In addition, the common types of bearing fault in real cases and the technique for seeding the defects in this study are briefly introduced. The process of data analysis is also illustrated in this chapter, three main tasks, which include EMI signal filtering, optimum demodulation band selection and the development of a systematic and efficient signal processing procedure, are briefly presented in this chapter for tackling the EMI interference problems in internal sensor-based measurement and for further investigating of the internal sensor-based measurement in this study. The details of the data analysis part are further illustrated in next three chapters.

CHAPTER 4 ELECTROMAGNETIC INTERFERENCE

ISSUE AND THE FILTERING SOLUTIONS

4.1 Introduction

Electromagnetic Interference (EMI) is defined as an unwanted signal that is either radiated or conducted through electrical equipments that may obstruct the proper performance of the equipments [15]. EMI is caused by current and voltages in the functioning electrical or electronic devices. It is usually received or transmitted by wire conductors carrying signals or by the power supply conductor or both.

Variable Frequency Drive (VFD), which is also called AC drive, is a motor controller for driving an electrical motor by varying the frequency supplied to the motor. This drive also can regulate the output voltage in proportion to the output frequency for providing a constant ratio of voltage to frequency. The basic working process of VFD is shown in Fig 4.1, the VFD firstly converts the AC supply voltage into DC through applying a rectifier, and the filter capacitors is also utilized here for smoothing voltage ripples. Then the DC voltage is transformed back to AC by using the technique of Pulse Width Modulation (PWM).

With the benefit of reducing energy costs, increasing production, extending equipment life and reducing maintenance, the VFD is widely applied in the industrial applications. However, abrupt voltage transitions on the output terminals of VFD may cause the radiated and conducted EMI, which has been noticed to be a serious problem that may affects the receivers for detecting the desired signals or adversely influences the operation of other electronic or system [93–95] . The main source of EMI noise from VFD is the high dv/dt of pulse-width modulated (PWM) output voltage waveforms. These PWM signals can be generated by comparing a reference signal $r(t)$ – an AC signal of the required frequency f_r to obtain the correct motor speed – with a carrier signal $c(t)$,

as follows [95]:

$$x_{PWM}(t) = \text{sgn}[r(t) - c(t)] \quad (4.1)$$

The carrier signal is generally a sawtooth or triangle waveform, and the carrier frequency f_c called the switching frequency. The frequency f_r of the reference signal has been called the ‘pseudo line frequency’ [96], and this terminology is adopted here. When integrated, a PWM signal creates an approximate sinusoid at the pseudo line frequency, but with higher frequency content. Fig. 4.2 shows an example of this process, where the effect of switching frequency on the generated sinusoid is clearly visible.

As outlined by Sun [95], the Fourier analysis of PWM signals is quite complex, and certainly beyond the scope of this paper, but the spectra of PWM waveforms are known to include the following discrete components:

- 1). Harmonics of the pseudo line frequency f_r
- 2). The carrier (switching) frequency and its harmonics, at $f = nf_c, n = 1, 2, \dots, \infty$
- 3). Sidebands spaced at pseudo line frequency around the carrier harmonics, at $f = nf_c \pm mf_r, m = 1, 2, \dots, \infty$, with distribution dependent on the precise nature of modulation [95].

4.2 Review of the EMI issue in bearing fault diagnosis

In specific to the area of machinery fault detection, EMI signal may interfere the surrounding transducers for data collection and affects the faults signal recognition.

Smith et al. [14] found that the internal sensor-based measurement for planetary bearing diagnosis is easily obstructed by EMI from VFD. The results demonstrated that when the full bandwidth based signal processing procedure (Cepstrum pre-whitening and envelope analysis) was applied to the vibration data collected from internal sensor, the electrical interference related components and their sidebands dominated the whole envelope spectrum in the some cases, and the bearing fault related components were hard to be extracted. When the narrow bandwidth demodulation based signal processing procedure (order tracking, TSA, Fast Kurtogram and envelope analysis) was applied, although the signal-to-noise ratio (SNR) increased and the bearing fault related components were easier to be extracted, the existence of EMI strongly affected the performance of Fast Kurtogram technique and the wrong demodulation band with no bearing fault information was selected in part of tests.

4.3 Further examination of EMI issue and EMI components

With the aim of clarifying the frequency components of VFD generated EMI signal, a test was introduced in this part: In this experiment, an 8-pole AC induction motor controlled by VFD was operated as the main EMI source. two B&K 4394 accelerometers were installed to be impending for receiving EMI signal. A tubular slip ring, which was believed to be the main reason for introducing the EMI signal into internal sensor based measurement in [14], was used to connect one of the accelerometer and the B&K PULSE data collection system. Slip ring is an electromechanical device that allows the transmission of power and electrical signals from a stationary to a rotating structure. The switching frequency of VFD was set to be 8 kHz and the shaft speed was 6 Hz. The sampling frequency was set as 65536 Hz.

The time waveforms of the collected vibration data, which come from both the accelerometers with slip ring and the one without slip ring, are displayed in Fig. 4.3, It is seen that no EMI information could be extracted from the time signal. Their spectrum

domains are presented in Fig. 4.4 which present that while the accelerometer without the slip ring is not sensitive to the EMI information from VFD, the VFD switching frequency and its harmonics dominate the whole frequency domain for the case of accelerometer with the slip ring. A zoom in spectrum analysis around the switching frequency 8 kHz, which is for the vibration signal collected by accelerometer with slip ring, is shown in Fig. 4.5. The sidebands of the carrier frequency are 24 Hz, 100 Hz and their harmonics. The components of 24 Hz and its harmonics are related to the motor speed, and the components of 100 Hz and its harmonics are related to the power frequency. As a result, it can be concluded that the EMI signal generated from VFD is an amplitude-modulated signal in which the switching frequency determines the carrier frequency and the modulation frequency is determined by both the input frequency and output frequency of VFD. In addition, the result also proves that the slip ring is the key factor that introduce the EMI signal into the data collection system.

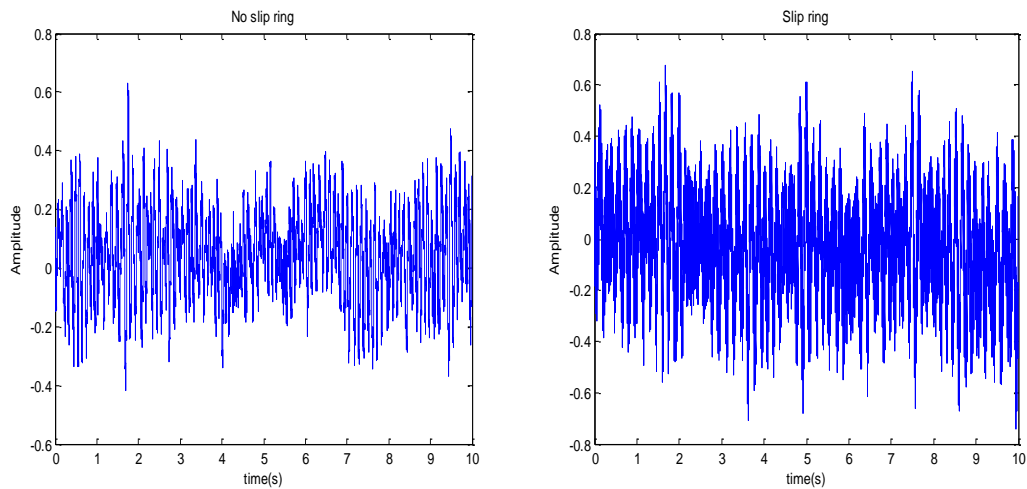


Fig. 4.1 Time domain of the EMI signal. (a) No slip ring; (b) Slip ring

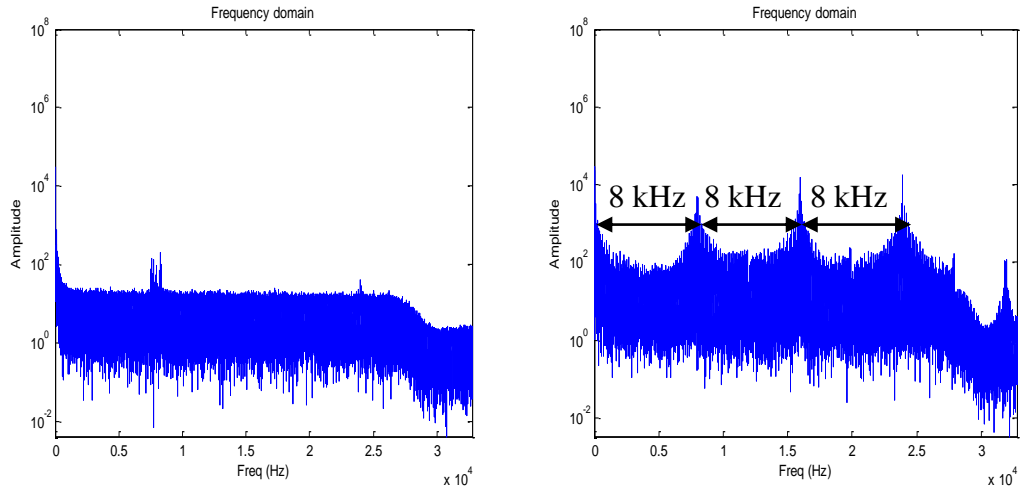


Fig. 4.2 Frequency domain of the EMI signal. (a) No slip ring; (b) Slip ring

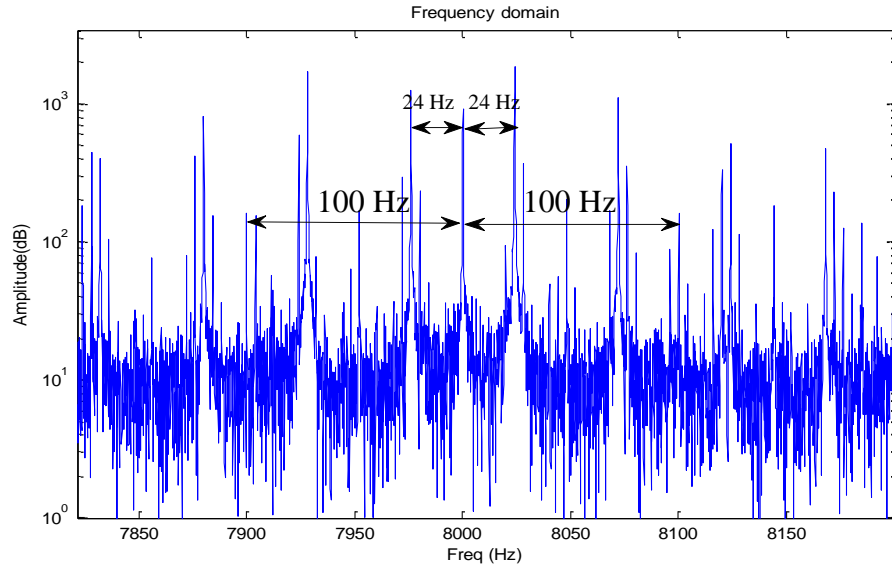


Fig. 4.3 Zoomed spectrum of the EMI around 8000 Hz

4.4 EMI signal filtering strategies

As the preceding EMI issue, the vibration signal, which is collected by the internal sensor, is problematical to be utilized for the planetary bearing fault detection. For this reason, it is essential to develop an efficient strategy for filtering the EMI signal. In this section, several advanced signal processing techniques, such as Discrete/random separation (DRS), Cepstrum editing and Cepstrum pre-whitening, are employed here in

an attempt to remove the EMI components from original signal. The collected EMI signal with the slip ring, which is detailed introduced in the previous part, is used as a testing signal.

4.4.1 DRS based filtering

The basic principle of the DRS technique is to find a filter $H(f)$ which can predict the current value of the signal from its delayed version through calculating the frequency response function (FRF) in frequency domain. The FRF value could be obtained from large amounts of blocks of data which are windowed before Fourier transform. The filter is presented as follow [27]:

$$H(f) = \frac{(\rho N / 2) |W(f)|^2}{(\rho N / 2) |W(f)|^2 + 1} \quad (4.2)$$

Where ρ is the signal-to-noise ratio, N is the transform size, $W(f)$ is the Fourier transform of the selected window.

The DRS filter was applied to the testing data for removing the EMI signal. The time waveforms of the raw signal and filtered signal are compared in Fig. 4.6 and their spectrums are compared in Fig. 4.7. It is noted from the spectrum that while there is some decline for protrusions of the carrier frequency (8 kHz) and its harmonics. Most of the EMI components remains. A further comparison of the zoom for the PSD around the carrier frequency is plotted in Fig. 4.8. The result shows that the DRS filter removes parts of the sidebands around the carrier frequency. However, it is also noted that the filtered signal is distorted near the carrier frequency. The narrow bandwidth envelope spectrums (demodulation center frequency 8000 Hz, demodulation bandwidth 1024 Hz) of both the raw signal and the filtered signal are presented in Fig. 4.9. In Fig. 4.9 (a), it is evident that the envelope spectrum mainly exhibits peaks related to the motor speed frequency, power frequency and their harmonics. After the DRS filtering process, the Fig. 4.9 (b) presents that part of the EMI components are attenuated. However, after the filtering process, the envelope spectrum is dominated by some other frequency

components that could not be clearly identified.

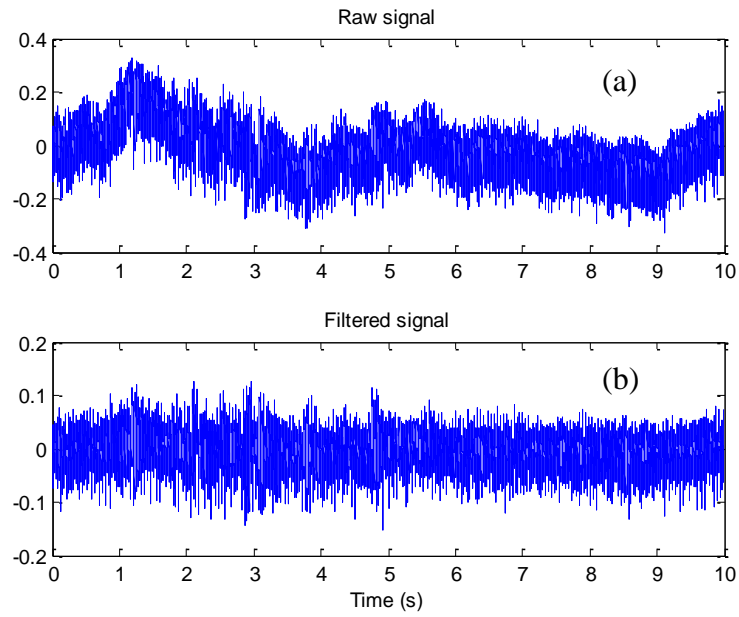


Fig. 4.4 Time waveform: (a) raw signal, and (b) DRS filtered signal

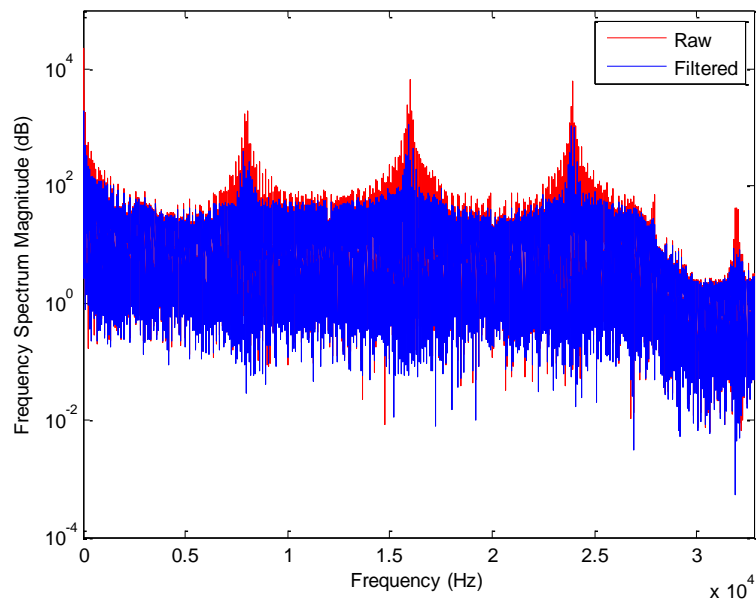


Fig. 4.5 Comparison between the spectrum of raw signal and DRS filtered signal

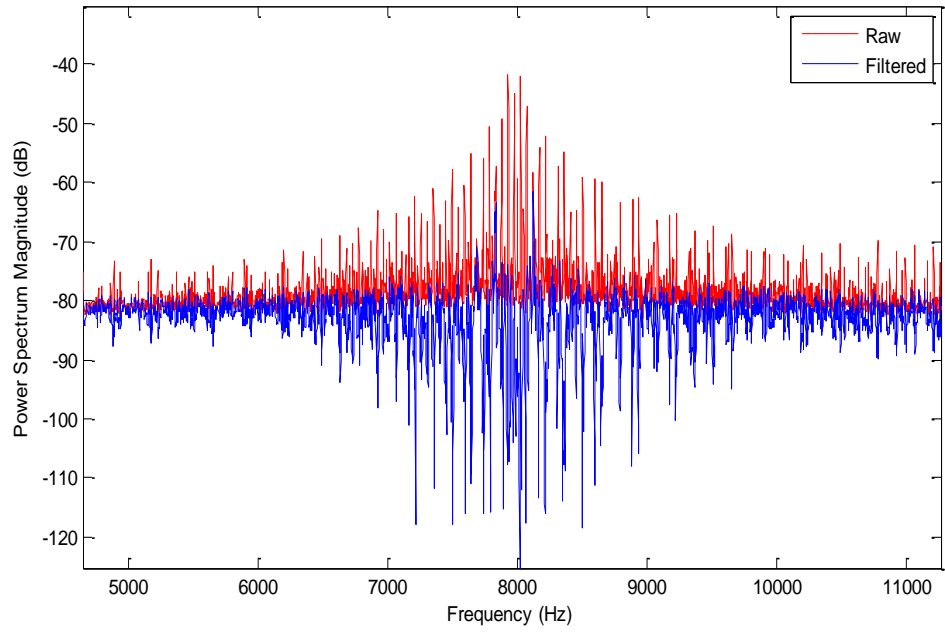


Fig. 4.6 Comparison between the zoom of PSD of raw signal and DRS filtered signal (around 8000 Hz)

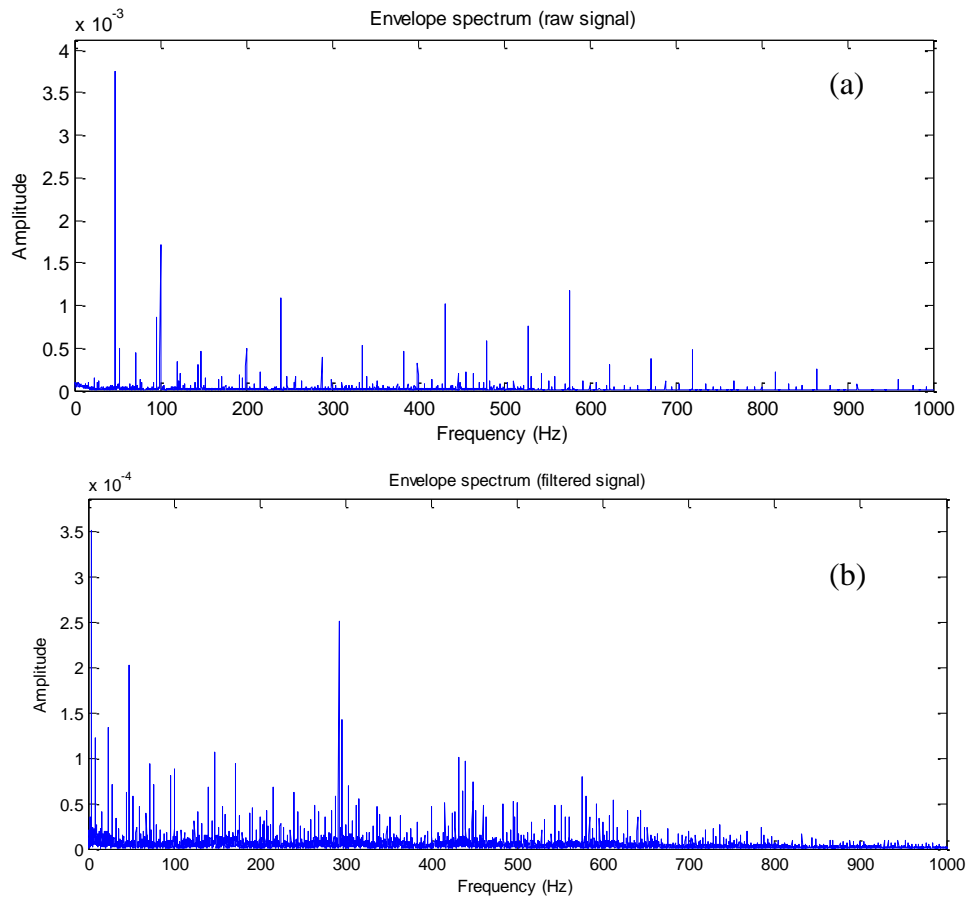


Fig. 4.7 Envelope spectrum: (a) raw signal, and (b) DRS filtered signal

4.4.2 Cepstrum editing based filtering

This filtering technique is based on editing the components in the Cepstrum domain of the original signal. The definition of the Cepstrum is the inverse Fourier transform of a logarithmic spectrum that can be presented as follows [97]:

$$C(\tau) = \mathcal{F}^{-1} [\log |X(f)|] \quad (4.3)$$

As the $X(f)$ could be expressed as:

$$X(f) = \mathcal{F} [x(t)] = A(f) e^{j\phi(f)} \quad (4.4)$$

Thus:

$$\log |X(f)| = \ln(A(f)) \quad (4.5)$$

Based on the equations above, it can be deduced that the peaks of the Cepstrum domain could indicate the appearance of the periodic structure in the frequency domain, which includes both harmonics and sidebands. Hence, In order to remove the specific harmonics or sideband families, it is an efficient way to simply edit real Cepstrum (The phase information is not contained) by setting the magnitude of correlated harmonics to zero. For instance, if the deterministic components are 25 Hz and its harmonics, the related quefrency in real Cepstrum is 40 ms and setting zero value around this quefrency could almost completely delete the effect of this family of harmonics in the original signal.

The Cepstrum editing was utilized to the testing data for filtering the EMI signal. The time waveforms of the raw signal and filtered signal are compared in Fig. 4.10 and their spectrums are compared in Fig. 4.11. It is noted from the spectrum that, although the protrusions of the carrier frequency and its harmonics remains, most of the EMI components are removed. A further comparison of the zoom for the PSD around the carrier frequency is plotted in Fig. 4.12. The result shows that almost all the sidebands around the carrier frequency are removed through Cepstrum editing. The narrow bandwidth envelope spectrums (demodulation center frequency 8000 Hz, demodulation

bandwidth 1024 Hz) of both the raw signal and the filtered signal are presented in Fig. 4.13. In Fig. 4.13 (a), it is evident that the envelope spectrum is dominated by the motor speed frequency, power frequency and their harmonics. After the procedure of Cepstrum editing, Fig. 4.13 (b) presents that EMI related components are largely removed, but the 24 Hz, 100 Hz, 144 Hz frequency lines remain and could not be filtered out.

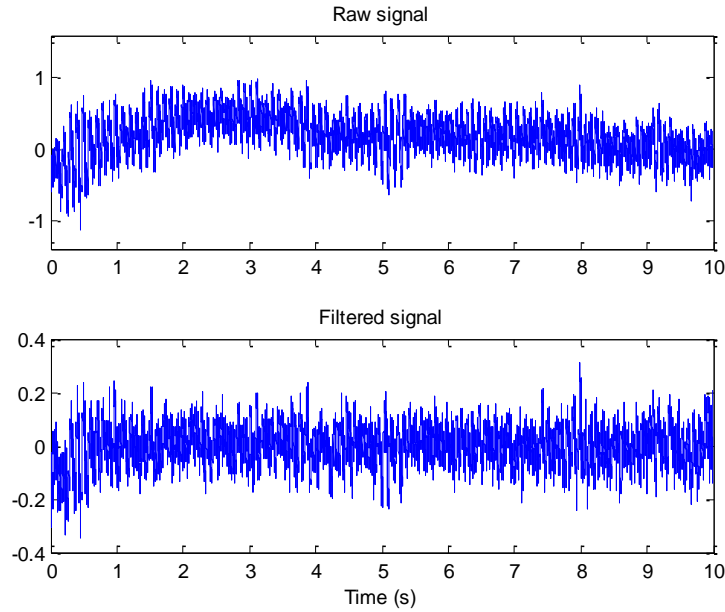


Fig. 4.8 Time waveform: (a) raw signal, and (b) Cepstrum editing filtered signal

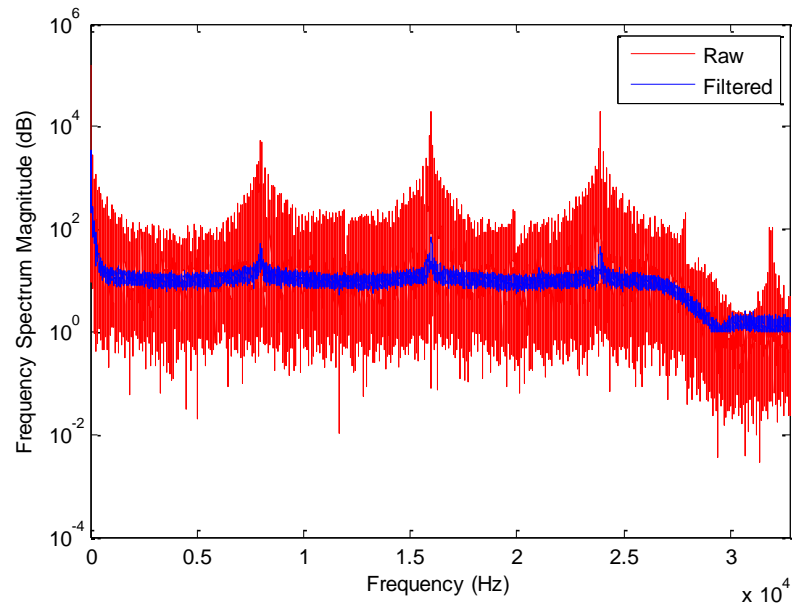


Fig. 4.9 Comparison between the spectrum of raw signal and cepstrum editing filtered signal

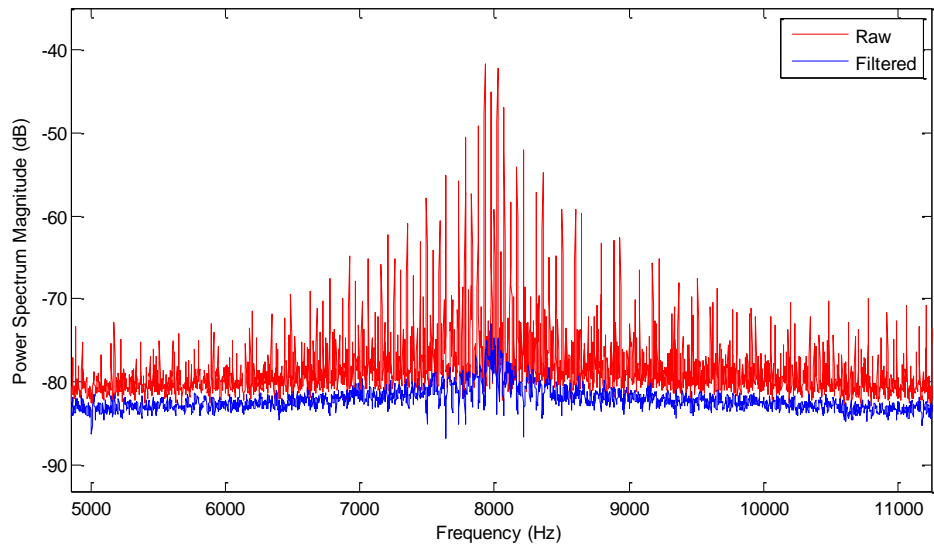


Fig. 4.10 Comparison between the zoom of PSD of raw signal and cepstrum editing filtered signal (around 8000 Hz)

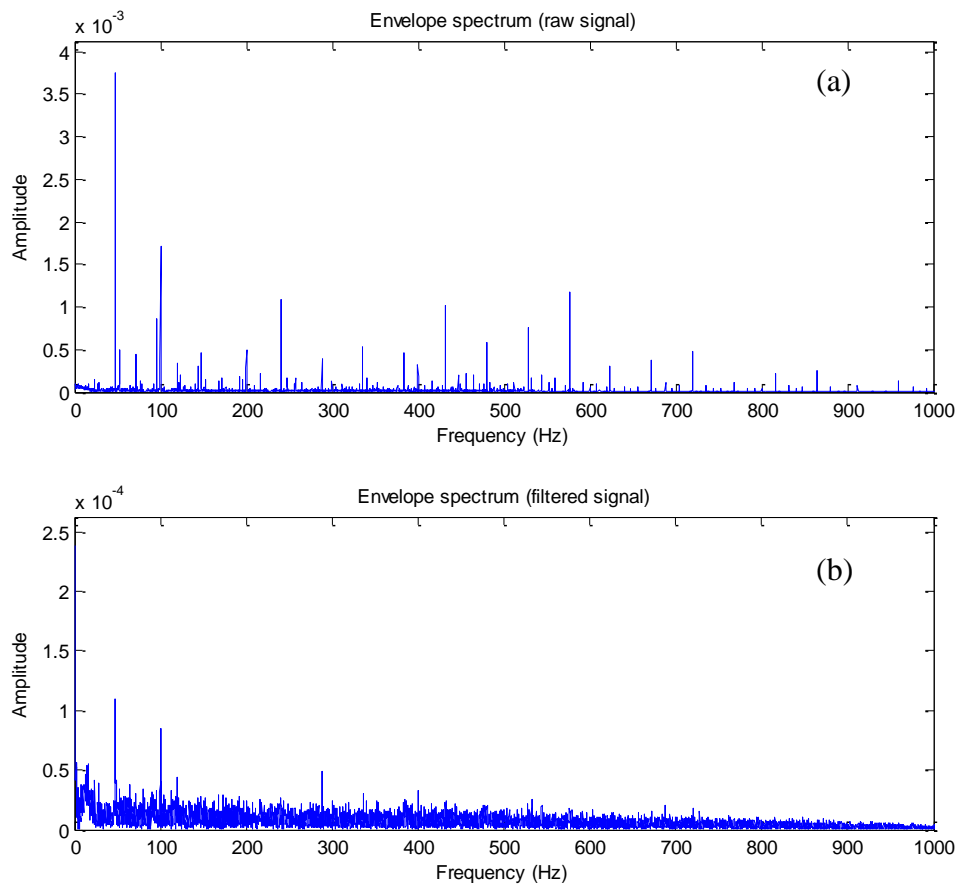


Fig. 4.11 Envelope spectrum: (a) raw signal, and (b) Cepstrum editing filtered signal

4.4.3 Cepstrum whitening based filtering

The principle of Cepstrum whitening is detailed introduced in the section 2.3.2. The basic procedure is setting a zero value in the whole real Cepstrum for the raw signal, the obtained signal is transformed back to the spectrum and recombined with the phase of the raw signal, the filtered signal is obtained through inverse transforming to the time signal to the time domain [43]. It is worth noting that the filtering method of Cepstrum pre-whitening is the extreme case of the Cepstrum editing that sets all the components in the real Cepstrum to zero instead of several specific harmonics or sidebands families, which means the all the deterministic components in frequency domain have the same amplitude and no longer protrude from noise values and are dominated by the latter.

The Cepstrum pre-whitening was utilized to the testing data for filtering the EMI signal. The time domain signals for the raw signal and the method of pre-whitening are compared in Fig. 4.14 and their spectrums are compared in Fig. 4.15. It shows that this filtering method completely flattens the whole spectrum. A further comparison of the zoom for the PSD around the carrier frequency is plotted in Fig. 4.16. The narrow bandwidth envelope spectrums (demodulation center frequency 8000 Hz, demodulation bandwidth 1024 Hz) of both the raw signal and the filtered signal are presented in Fig. 4.17. In Fig. 4.17 (a), the envelope spectrum is dominated by the motor speed frequency, power frequency and their harmonics. After the procedure of Cepstrum whitening as shown in Fig. 4.17 (b), EMI related components are largely removed, but the 24 Hz, 100 Hz, and 144 Hz frequency lines remain and could not be filtered out.

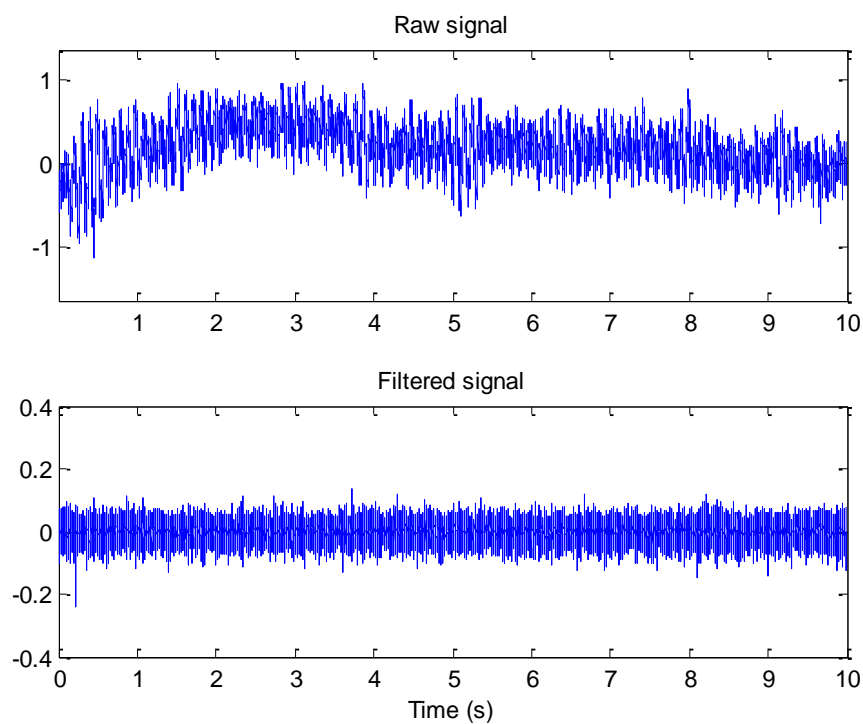


Fig. 4.12 Time waveform: (a) raw signal, and (b) Cepstrum whitening Filtered signal

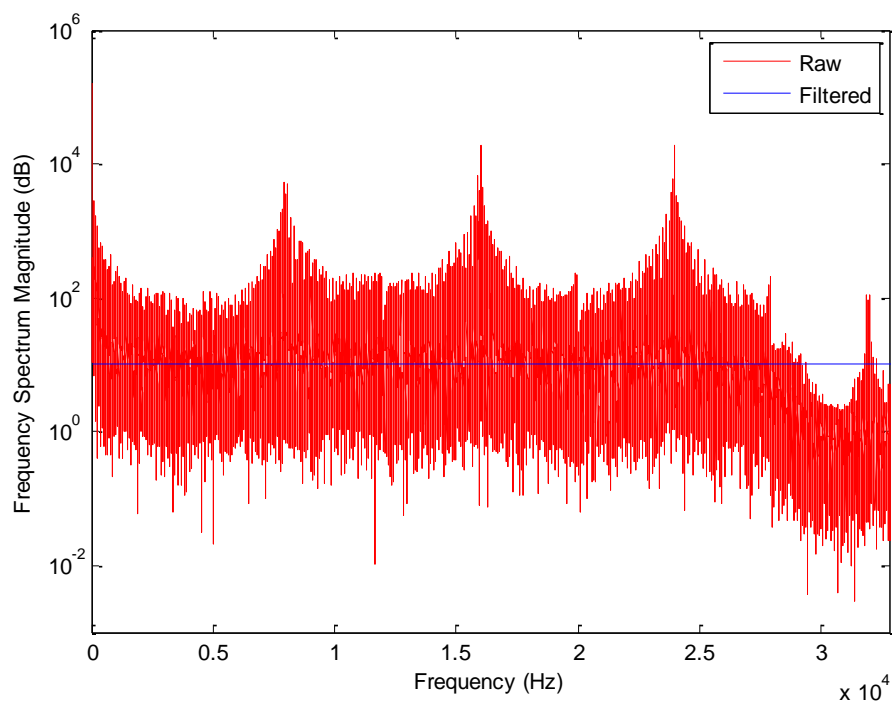


Fig. 4.13 Comparison between the spectrum of raw signal and Cepstrum whitening filtered signal

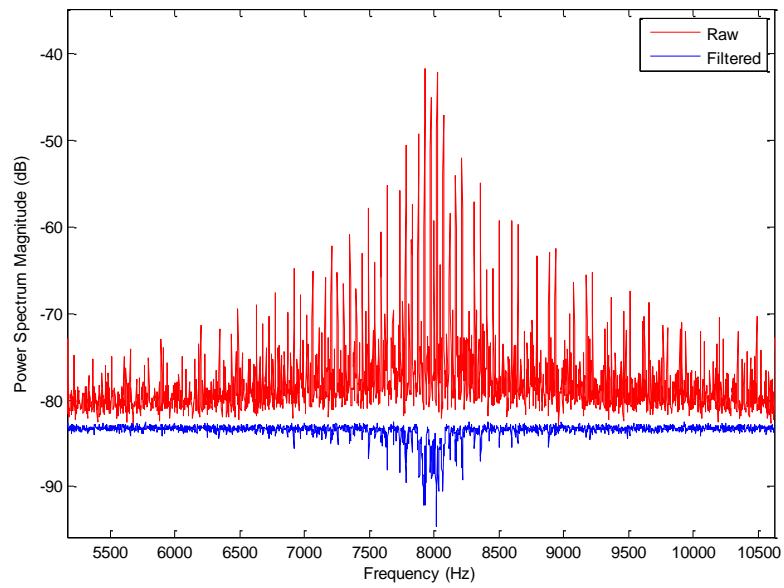


Fig. 4.14 Comparison between the zoom of PSD of raw signal and cepstrum whitening filtered signal (around 8000 Hz)

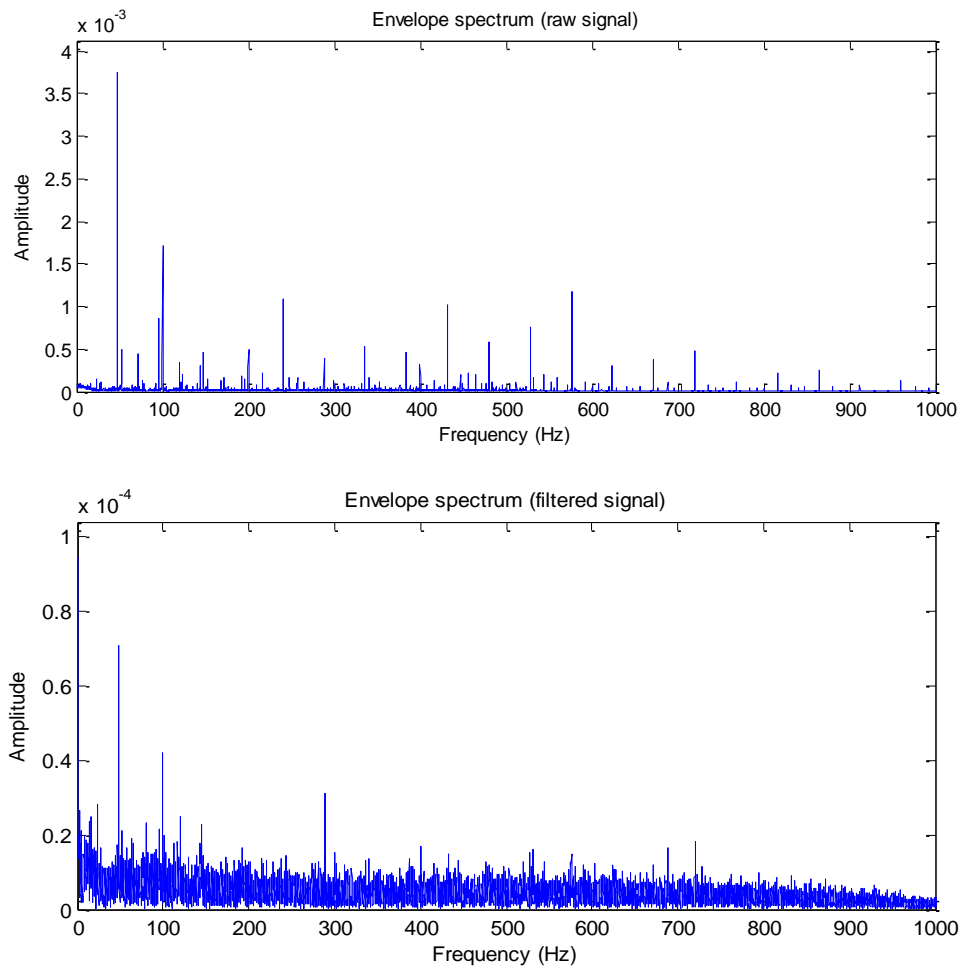


Fig. 4.15 Envelope spectrum: (a) raw signal, and (b) Cepstrum whitening filtered signal

4.5 Discussion

As the comparisons of the envelope spectrum between the three selected EMI filtering techniques, the results demonstrate that none of these techniques could completely filter out the EMI signal. However, it is also interesting to notice that the filtering performances of the Cepstrum editing and Cepstrum pre-whitening are much better than the technique of DRS. In addition, as shown in the envelope spectrums from Fig 4.13 and Fig 4.17, it is noticeable that the filtering effects of both the Cepstrum editing and Cepstrum pre-whitening are almost the same. However, comparing to the Cepstrum editing, Cepstrum pre-whitening is less time consuming, because it simply sets all cepstral components to zero instead of searching for the particular deterministic components in frequency domain and removing them in the real Cepstrum domain as the Cepstrum editing. Thus, applying the technique of Cepstrum pre-whitening could be used as the preprocessing step for removing a large portion of EMI signal.

4.6 Summary

In this chapter, the EMI issue is detailed introduced, and the components of EMI signal are analyzed via the collected vibration data with the appearance of intense EMI generated from the VFD. Several advanced processing techniques, such as DRS, Cepstrum editing and Cepstrum pre-whitening, are implemented to the testing signal for removing the EMI components from the original signal. The results show that the Cepstrum pre-whitening has the best filtering performance among these three techniques. Therefore, the Cepstrum pre-whitening is selected as the preprocessing step for the bearing fault diagnosis procedure presented in chapter 6.

CHAPTER 5 A NOVEL SPECTRAL KURTOSIS METHOD FOR DEMODULATION BAND SELECTION

5.1 Introduction

The selection of the optimal demodulation frequency band is a significant step in bearing fault diagnosis. This is because the selected demodulation frequency band determines whether the fault information can be extracted from the demodulated signal during the process of the envelope analysis. The technique of Fast Kurtogram, which uses as a fault indicator the kurtosis of the filtered time signal, has been shown to be very efficient in choosing the demodulation band for bearing diagnostics, even in the presence of strong background Gaussian noise. However, this technique may still fail in a specific environment, such as in the presence of electromagnetic interference [14].

In this chapter, a simple demodulation band selection method called 'Kurtrugram' is proposed with the aim of accurately extracting bearing fault-related impulsive content from vibration signals contaminated with strong EMI. This new presented approach combines the core ideas of the technique of Fast Kurtogram and another demodulation band selection method called Protrugram, which utilized the defect indicator of kurtosis of the envelope (amplitude) spectrum rather than time signal and has demonstrated superiority in detecting bearing faults for the condition where the signal-to-noise ratio (SNR) is relatively low [63]. The method of Kurtrugram is then applied to vibration signals obtained from a planetary gearbox test rig with planet bearings seeded with inner and outer race faults. Results from the Fast Kurtogram and Protrugram methods are also presented in this chapter as comparison.

This chapter is organized in the following structure: an overview of two existing demodulation band selection methods, namely, Fast Kurtogram and Protrugram, is presented in section 5.2. The basic information of the collected vibration signal for tests

is introduced in section 5.3. The experimental results of the two established methods (Fast Kurtogram and Protrugram) are shown in section 5.4. The introduction of the new proposed method 'Kurtrugram' and the corresponding experimental results are illustrated in section 5.5 and section 5.6. Discussions are presented in section 5.7 for comparing the bearing faults detection performances between the two established methods and the new proposed method, and showing the effectiveness and limitations of the proposed method.

5.2 Review of Fast Kurtogram and Protrugram

As previously mentioned in section 5.1, the Fast Kurtogram and Protrugram are two well-recognized tools for bearing fault diagnosis. Further details of these two techniques are reviewed below.

5.2.1 Fast Kurtogram

The Fast Kurtogram was first proposed in [58] as an efficient algorithm for detecting the existence of non-stationarity in signals and showing its location in the frequency domain. This method is based on spectral kurtosis, which is a fourth-order statistical tool and is very sensitive to impulsive signals. SK was estimated based on the short-time Fourier transform (STFT) in [57] and can be expressed as follows:

$$K(f) = \left\langle |X(t, f)|^4 \right\rangle / \left\langle |X(t, f)|^2 \right\rangle^2 - 2 \quad (5.1)$$

Where $X(t, f)$ is the (complex) time/frequency envelope of the original signal and the square of its amplitude gives the power spectrum at each time t . $\langle . \rangle$ is the time-averaging operator.

Due to the fact that the SK value varies with both the frequency f and frequency resolution Δf , a representation of SK in the plane $(f, \Delta f)$ is convenient for finding

the maximum value of SK. However, the full exploration of SK over the entire $(f, \Delta f)$ plane is infeasible as it is time-consuming and thus difficult to apply in industrial applications [58]. The Fast Kurtogram solves this issue by applying a 1/3-binary tree structure for designing band-pass filters and investigating the SK value of the filtered signal from selected bandwidths. The Fast Kurtogram has a visual form of a 2D plane in which the horizontal axis represents the frequency and the vertical axis represents the frequency resolution. A colour scale shows SK values for a certain bandwidth. The frequency band (or part of the Kurtogram grid) with the maximum SK value is then chosen as the optimal demodulation band for subsequent envelope analysis.

Although the Fast Kurtogram has proven to be effective in many cases [27,99], including in the presence of strong Gaussian noise, it has been found to be ineffective in several conditions, as illustrated in [43,61,63,64]. The performance of the Fast Kurtogram may be poor when the signal-to-noise ratio is relatively low or strong non-Gaussian noise appears.

5.2.2 Protrugram

Intending to overcome the drawbacks of the Fast Kurtogram, the Protrugram [63] was developed based on the kurtosis of the narrowband envelope (amplitude) spectrum rather than the kurtosis of the envelope of the bandpass filtered time signal. Another innovation of the Protrugram is in setting the bandwidth (frequency resolution) to a fixed value, which is typically selected based on the mechanical parameters of the monitored machine, such as the bearing characteristic defect frequencies for bearing diagnosis. The Protrugram is therefore not a blind technique (unlike the Fast Kurtogram) since the knowledge of the system parameters is required.

For the method of Protrugram, the selected bandwidth should include 1-5 harmonics of the characteristic frequencies of the bearing(s) under study. Too narrow a bandwidth (less than the fundamentally sought frequency) would fail in reflecting the fault

information in the envelope spectrum. If the bandwidth is too wide, more noise will be included in the filtered signal and the bearing fault information may be difficult to extract from the noise. Barszcz and Jabłoński [63] ultimately suggest using a bandwidth including the first three fault frequency harmonics.

After the bandwidth is chosen, the optimal demodulation band is determined by stepping through the candidate centre frequencies (across the available frequency range), generating the envelope spectrum for each and calculating its kurtosis, and then selecting the band returning the highest kurtosis value. As noted in [63], the selection of centre frequency step size involves a trade-off between computation time and accuracy (frequency resolution), and Barszcz and Jabłoński found that a step size of about 100 Hz was a reasonable choice in their application.

Despite this advantage, the Protrugram was found here to be unsuccessful in diagnosing bearing faults in the presence of strong EMI contamination of the vibration signal (results are presented in section 5.4). This prompted the development of a new optimal demodulation band selection method 'Kurtrugram' in this study, which combines the fault indicator of the Kurtogram (kurtosis of the temporal signal) with the Protrugram's pre-set bandwidth and its capability to finely select the optimal centre frequency. Further details are outlined in section 5.5.

5.3 Vibration signal description

The bearing fault signal is collected by Dr Wade Smith from the non-hunting tooth planetary gearbox in UNSW gearbox test rig. This section mainly shows the basic information of the collected vibration signal, which include test equipments, faulty bearings, test conditions and the bearing fault frequencies

5.3.1 Test equipments

The planetary gearbox test rig and the non-hunting tooth planetary gearbox used for this experiments are detailed introduced in chapter 3. In this study, A Brüel & Kjær 4394 IEPE-type accelerometer was used for vibration measurements. The accelerometer was mounted on the planet carrier in the axial direction, as part of a study to investigate the potential advantages of internal vibration measurements. Since the accelerometer rotates with the planet carrier, a Michigan Scientific B6-2 slip ring was used for transmitting the vibration signal to the signal conditioner. A Brüel & Kjær PULSE analyser was connected to a laptop running Brüel & Kjær Labshop software for data recording. The recorded data was then exported to MATLAB for further signal processing.

5.3.2 Bearing fault information

Faults were seeded in both the inner and outer races of the planet gear bearings in this study. IKO NAF 122413 needle roller bearings (see Table 5.1) were used, each containing 15 rollers of 2 mm diameter, and the bearing pitch diameter was 18 mm. Electric spark erosion was used for seeding the faults, which were of depth 0.4 mm and widths 1.2 and 1.0 mm for the outer and inner races, respectively.

Table 5.1 Planet gear bearing parameters

Type	IKO NAF 122413
Needle roller diameter (d)	2 mm
Pitch circle diameter (D)	18 mm
Number of rolling elements (n)	15
Contact angle (β)	0°

5.3.3 Test conditions

During the operation of the gearbox rig, testing was conducted at a constant input shaft speed of about 6 Hz, with torque loads of 30, 50 and 70 Nm. Separate testing was performed with the inner and outer race faults. The matrix of test conditions for the test rig is shown in Table 5.2. The sampling frequency was set at 131,072 Hz, the switching frequency of the VFD was set at 14 kHz, and the control (pseudo line) frequency of the VFD was 24 Hz (to provide a nominal 6 Hz input shaft speed for the 8-pole induction motor).

Table 5.2 Test conditions of the gearbox rig

Case	Input shaft speed (Hz)	Load (Nm)	Bearing fault location
1	5.78	70	Outer race
2	5.84	50	Outer race
3	5.89	30	Outer race
4	5.78	70	Inner race
5	5.84	50	Inner race
6	5.89	30	Inner race

5.3.4 Bearing fault frequencies

As explained in [29], for a rolling element bearing with a localised defect on one of the races, a series of impacts are generated when each rolling element strikes the defect. Unlike a conventional bearing configuration where the outer race is stationary and the inner race rotates at the shaft speed, for a planetary bearing, the outer race rotates at the speed of the planet gear while the inner race rotates in the opposite direction at the speed of the planet carrier (but with a fixed orientation with respect to the load). The kinematic equations for the bearing characteristic defect frequencies, in this case, are:

Ball pass frequency, outer race (*BPFO*):

$$BPFO = \frac{n}{2} \left[(f_i - f_o) \left(1 - \frac{d}{D} \cos \phi \right) \right] \quad (5.2)$$

Ball pass frequency, inner race (*BPFI*):

$$BPFI = \frac{n}{2} \left[(f_i - f_o) \left(1 + \frac{d}{D} \cos \phi \right) \right] \quad (5.3)$$

Where n is the number of rolling elements, ϕ is the angle of the load from the radial plane ($\phi=0$ here), d is the diameter of the roller, and D is the pitch diameter of the bearing. f_o and f_i are the planets bearing outer and inner race speeds. In this case, with an input shaft speed of just under 6 Hz, the approximate fault frequencies are: $BPFO=55$ Hz and $BPFI=69$ Hz. The inner race fault signal is expected to consist of a series of impulse responses fairly uniform in amplitude (not modulated by rotation of the gear), while the impulse responses in the outer race fault signal are expected to be modulated by the relative frequency of the inner and outer races, the rate at which the fault passes through the load zone.

5.4 Results with established methods

In this section, the collected bearing fault signals (found to be contaminated with EMI) from the experimentation described above are processed by the two established demodulation band selection methods, the Fast Kurtogram and the Protrugram (reviewed in section 5.2), and the performance of the two techniques is discussed. The Fast Kurtogram was applied down to a bandwidth of 512 Hz (Level 7), and the Protrugram was applied with a step size of 100 Hz and bandwidth of 512 Hz. Results from the 30 Nm load cases are omitted for brevity, but the diagnostic outcomes for all tests are summarised in section 5.7.

5.4.1 Outer race fault detection

For the bearing outer race fault with torque loads of 70, 50 and 30 Nm, the raw time signals are plotted in Fig. 5.1 and their power spectral densities are shown in Fig. 5.2. From the power spectra, it is clear that these three signals are contaminated by intense EMI generated by the VFD. The spectra contains discrete components at harmonics of the VFD switching frequency (8 kHz), with families of sidebands around these harmonics, spaced at the pseudo line frequency (24 Hz) and twice mains frequency (100 Hz), as explained in chapter 4. The EMI components, in fact, occupy a very wide frequency range, with these sidebands distributed over several kilohertz.

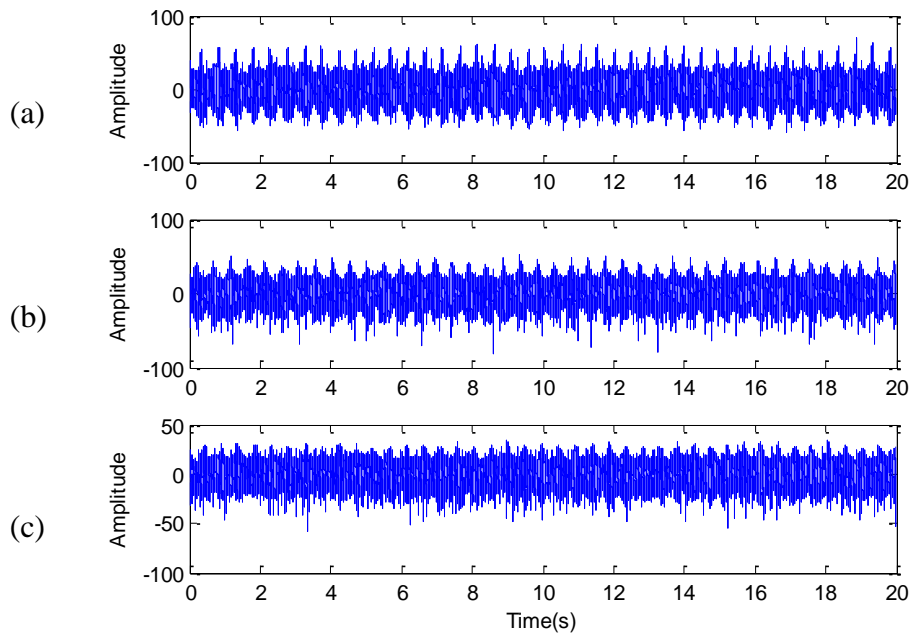


Fig. 5.1 Time waveforms of ORF signals at torque loads of (a) 70 Nm, (b) 50 Nm, and (c) 30 Nm

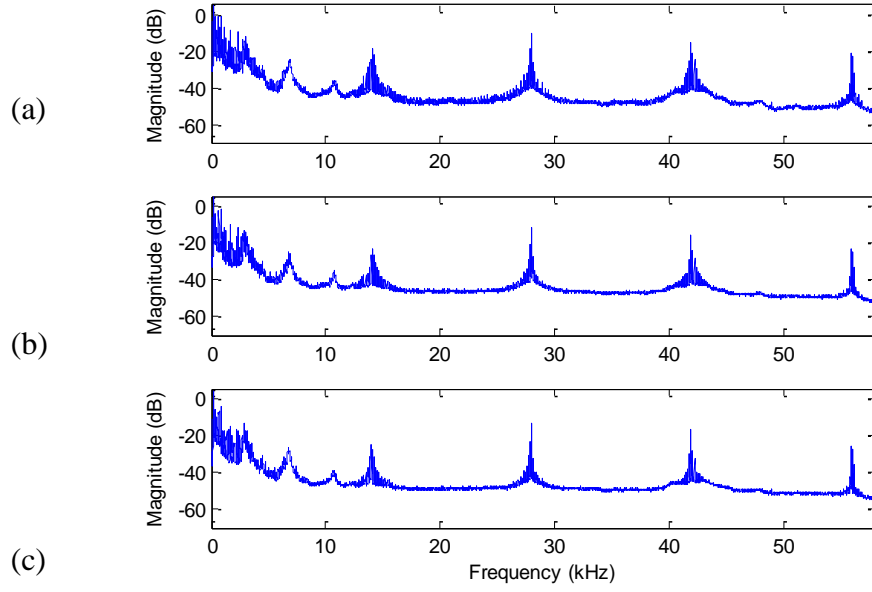


Fig. 5.2 PSDs of ORF signals at torque loads of (a) 70 Nm, (b) 50 Nm, and (c) 30 Nm

The Fast Kurtogram and Protrugram methods were first applied to the bearing fault signal for Case 1 (70 Nm torque, outer race fault). The paving of the Fast Kurtogram is shown in Fig. 5.3, where the determined demodulation band parameters are: center frequency (CF) of 64 kHz, and bandwidth (BW) of 1024 Hz. From the corresponding envelope spectrum in Fig. 5.4, the outer race fault information can be clearly identified. It is perhaps worth noting here that this frequency band, very close to the Nyquist frequency (65536 Hz), would certainly contain aliased components. However, as observed in [14], aliasing should not adversely affect envelope analysis since the repetition frequency of the impulses is sought, and not their individual frequency content.

A plot of the Protrugram for Case 1 is given in Fig. 5.5, giving an optimal CF of 14456 Hz, which is near the VFD switching frequency of 14 kHz. As shown in Fig. 5.6, the related envelope spectrum fails to diagnose the bearing fault, and is dominated instead by EMI-related components of 24 and 100 Hz, and their harmonics. Hence, in this case, the Fast Kurtogram succeeds in selecting a suitable demodulation band to detect the fault, while the Protrugram does not.

It is interesting to note that the region of the Kurtogram corresponding to the band selected by the Protrugram (14200-14712 Hz) is one of relatively low kurtosis (dark blue on the color scale). Likewise, the band selected by the Kurtogram (63488–64512 Hz) shows a very low kurtosis in the Protrugram. It appears that the problem for the Protrugram, in this case, is that the EMI signal is very well structured, giving strong, discrete components (and thus high kurtosis) in the envelope spectrum. This is clearly reflected in the Protrugram itself, which shows spikes in kurtosis at the VFD switching frequency harmonics. The authors in [63] illustrated that the maximum with steep edges in Protrugram should be ignored, because this is caused by harmonic components rather than the repetitive fault signature, which should be indicated by 'gentle slope' structure. However, this selection criterion is ambiguous for choosing the demodulation band in the cases that are corrupted by intense wideband interference. As shown in Fig. 5.5, there are a series of hill-like shapes in Protrugram distributed in a broad frequency range, which could be treated as the candidates for further demodulation. Thus, the authors here still pick the *CF* with the maximum kurtosis value in Protrugram instead of checking each hill-like shape.

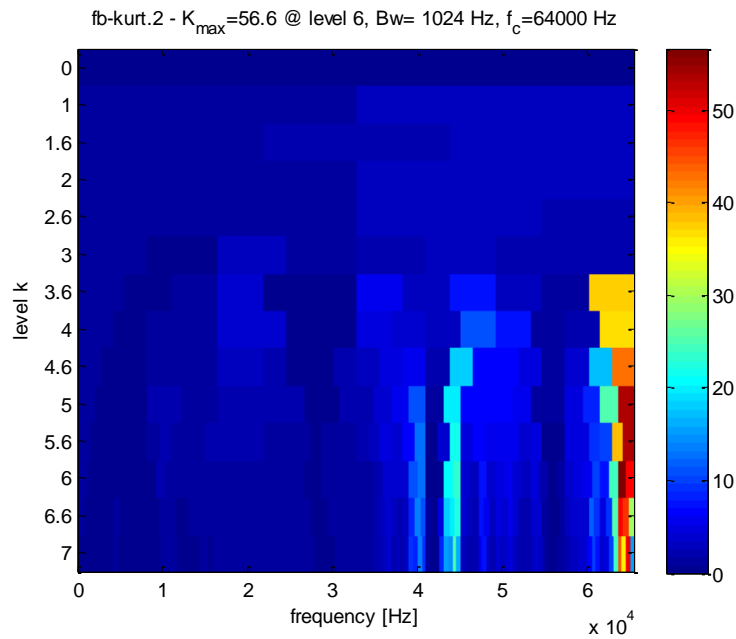


Fig. 5.3 Fast Kurtogram for Case 1 (70 Nm, outer race fault)

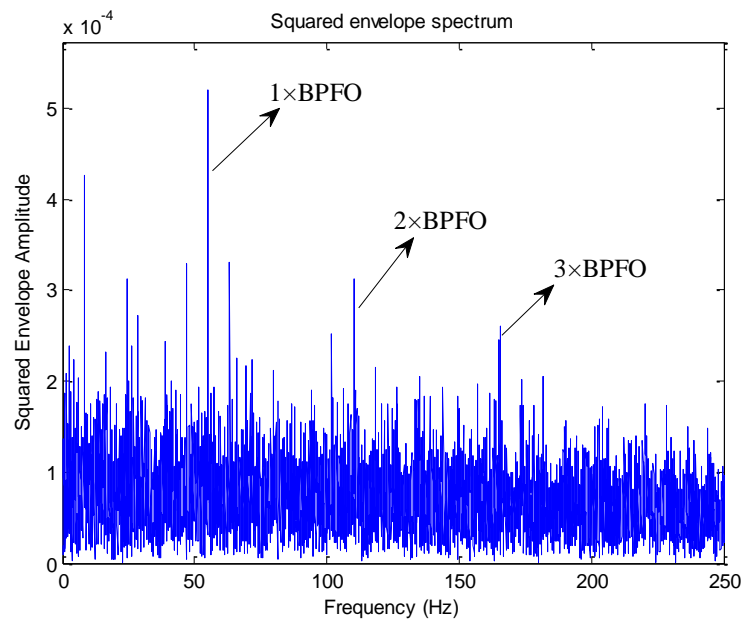


Fig. 5.4 Squared envelope spectrum from Fast Kurtogram for Case 1 (70 Nm, outer race fault)

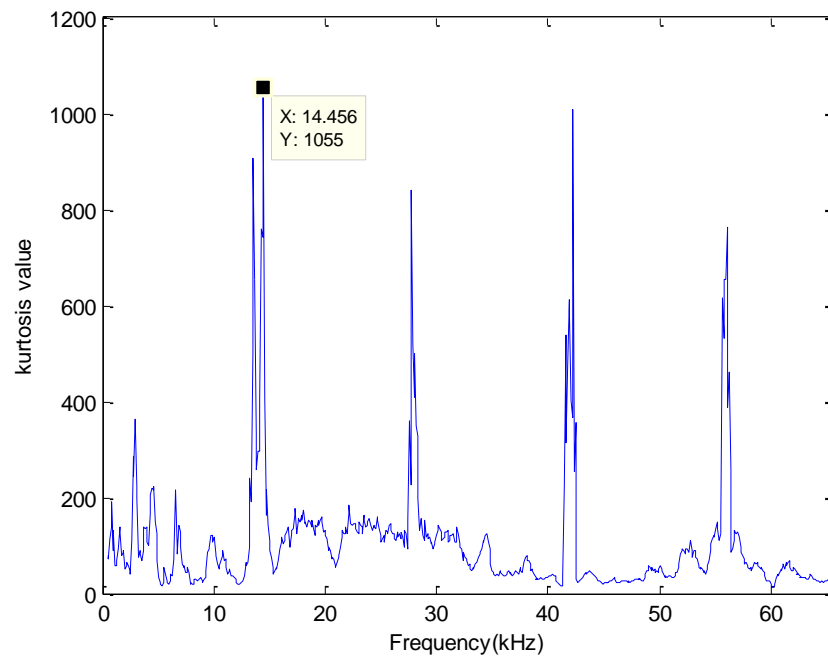


Fig. 5.5 Protrugram for Case 1 (70 Nm, outer race fault)

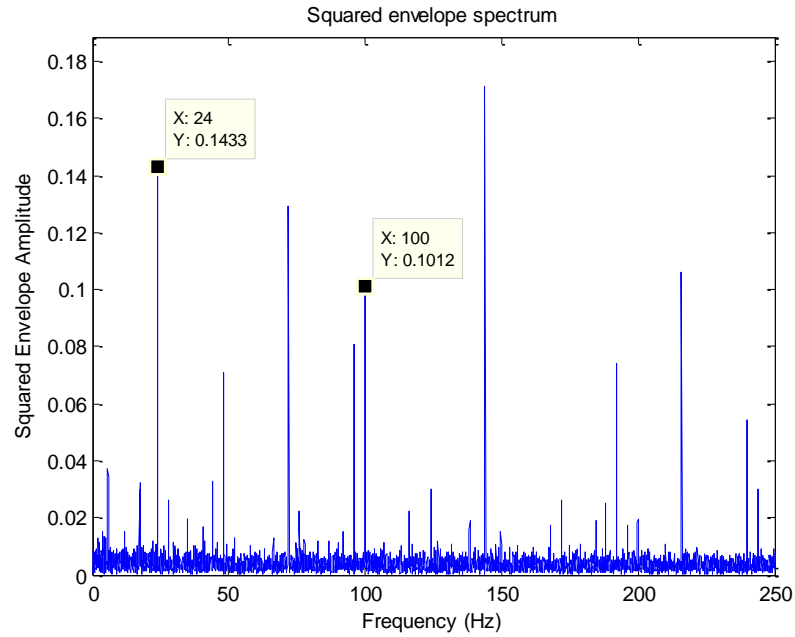


Fig. 5.6 Squared envelope spectrum from Protrugram for Case 1 (70 Nm, Outer race fault)

Shown in Fig. 5.7 is the Fast Kurtogram for Case 2 (50 Nm torque, outer race fault), which gives optimal demodulation band parameters of $CF = 19115$ Hz and $BW = 5461$ Hz. However, as shown in Fig. 5.8, the squared envelope spectrum is dominated by the EMI component at 100 Hz (twice mains frequency 50 Hz) and its second harmonic, and thus fails to reveal the bearing fault. Components at the input shaft speed, about 6 Hz, can also be seen throughout the spectrum.

The plot of Protrugram in Case 2 is presented in Fig. 5.9 and the optimal CF of 26256 Hz is selected. As shown in Fig. 5.10, the corresponding envelope spectrum fails in recognizing the bearing fault signature, and is dominated by EMI-related components of 100 Hz and their harmonics. Thus, in this case, both the Fast Kurtogram and Protrugram fail in selecting a suitable demodulation band to detect the fault.

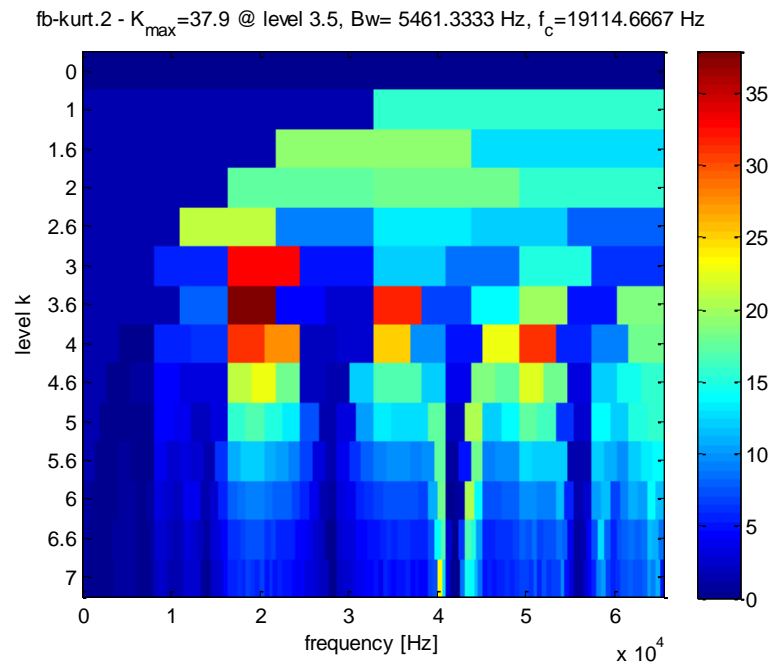


Fig. 5.7 Fast Kurtogram for Case 2 (50 Nm, outer race fault)

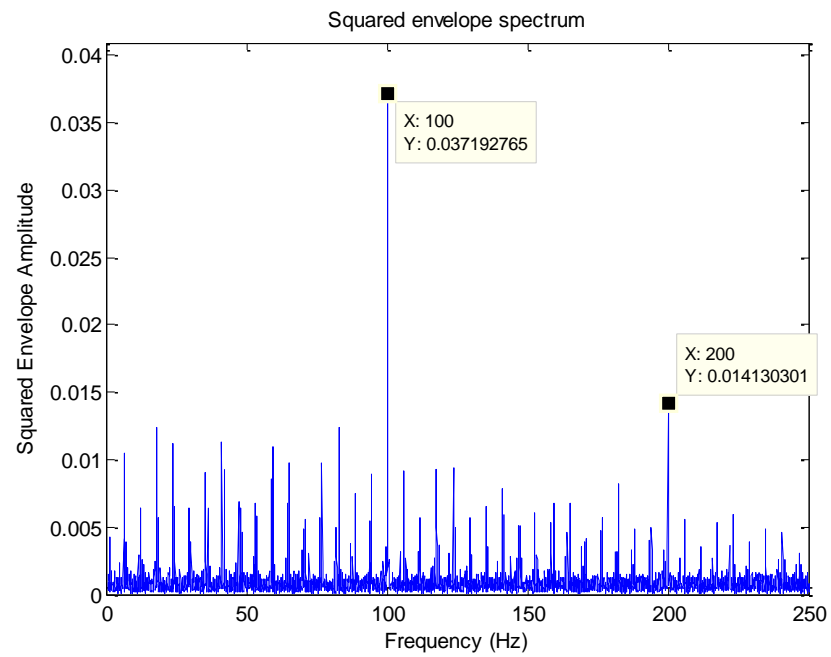


Fig. 5.8 Squared envelope spectrum from Fast Kurtogram for Case 2 (50 Nm, outer race fault)

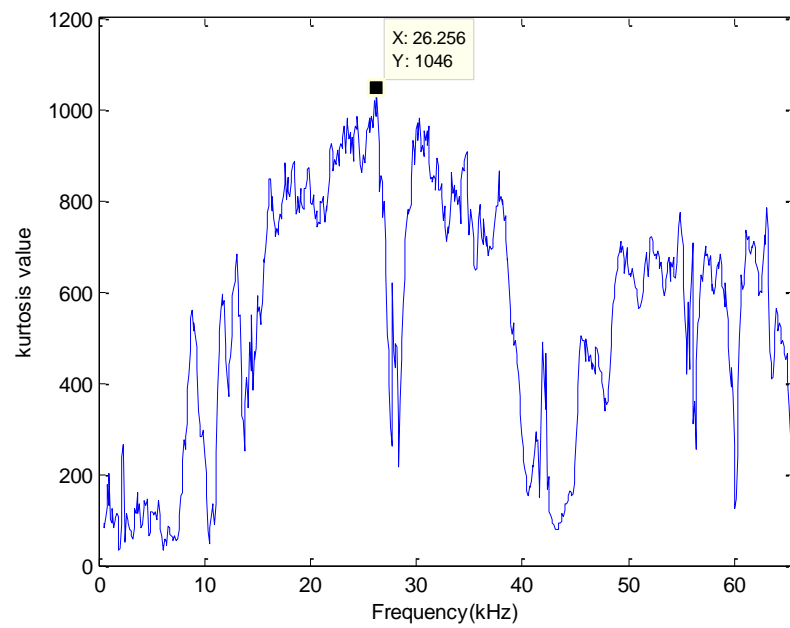


Fig. 5.9 Protrugram for Case 2 (50 Nm, outer race fault)

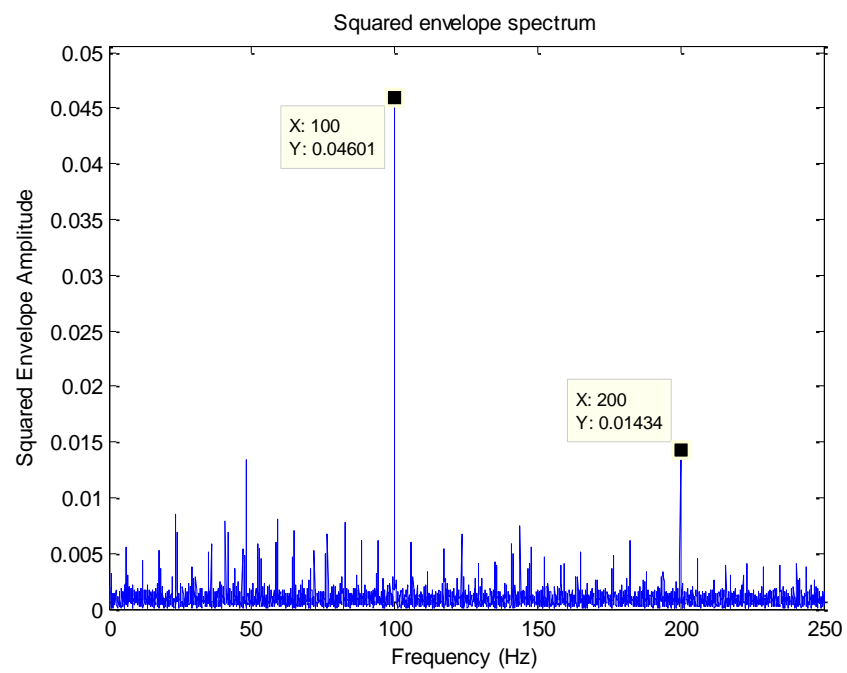


Fig. 5.10 Squared envelope spectrum from Protrugram for Case 2 (50 Nm, ORF)

5.4.2 Inner race fault detection

For the bearing inner race fault with torque loads of 70, 50 and 30 Nm, the raw time signals are plotted in Fig. 5.11 and their power spectral densities are shown in Fig. 5.12. Again, the power spectra show clearly that all signals are contaminated by intense EMI generated by the VFD.

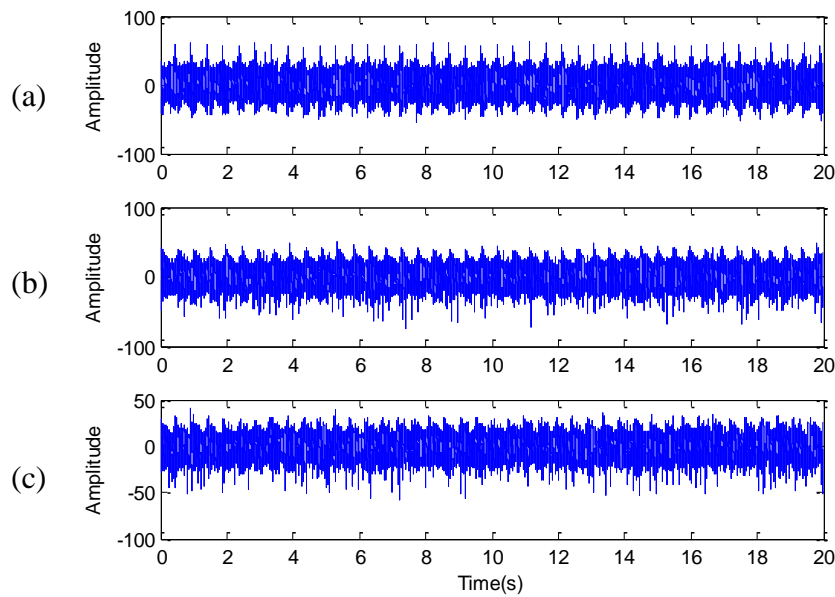


Fig. 5.11 Time waveforms of IRF signals at torque loads of (a) 70 Nm, (b) 50 Nm, and (c) 30 Nm

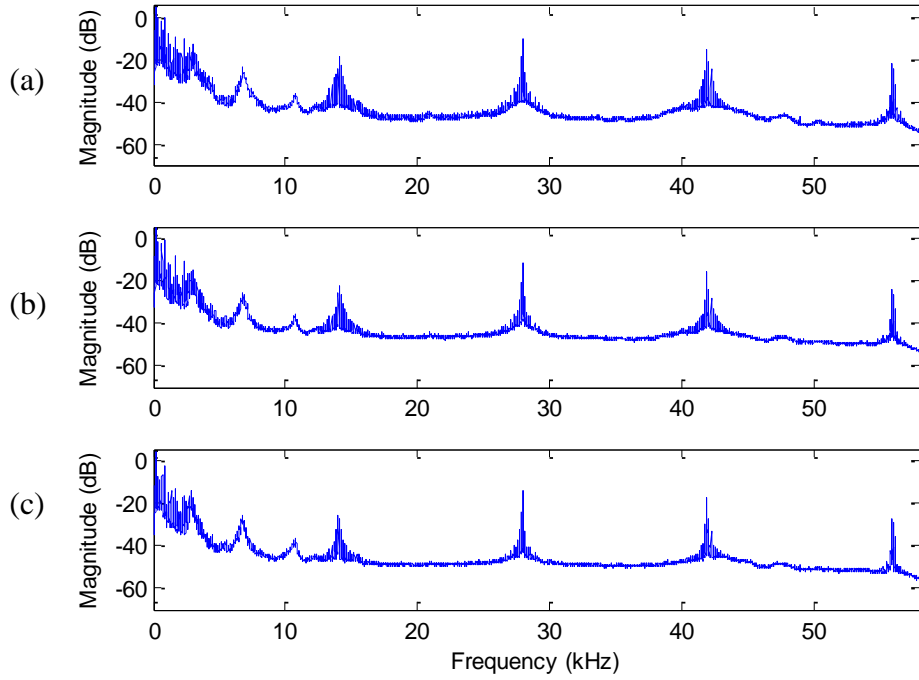


Fig. 5.12 PSDs of IRF signals at torque loads of (a) 70 Nm, (b) 50 Nm, and (c) 30 Nm

Shown in Fig. 5.13 is the Fast Kurtogram for Case 4 (70 Nm torque, inner race fault), which gives optimal demodulation band parameters of $CF = 64512$ Hz and $BW = 2048$ Hz, similar to Case 1 with the outer race fault. The corresponding envelope spectrum in Fig. 5.14 gives a clear inner race fault diagnosis. The BPFI harmonics in the spectrum are modulated by the planet carrier speed (2.05 Hz).

The Protrugram results are shown in Fig. 5.15, The optimal CF is chosen as 42256 Hz which is near the third harmonic of switching frequency (42 kHz), and the related envelope spectrum (Fig. 5.16) is dominated by the EMI components of 24 Hz, 100 Hz and their harmonics. However, in Case 4, it is also noted that two visible 'humps', which was suggested in [63] as the consequence of sought bearing fault, could be recognized between 35 kHz-45 kHz in the plot of Protrugram (Fig. 5.15). As presented in Fig. 5.17, the bearing fault frequency could be extracted from the envelope spectrum (Demodulation band is recommended by the peak of 'hump', CF is 43656 Hz)

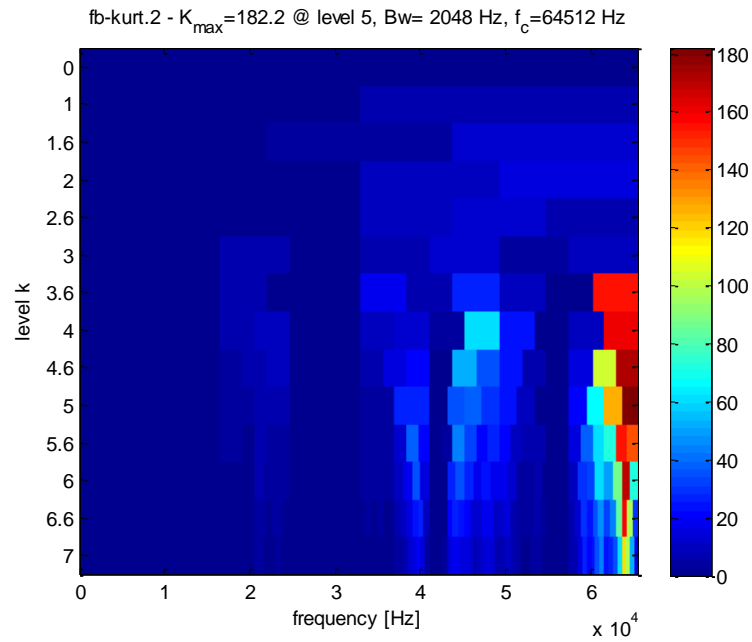


Fig. 5.13 Fast Kurtogram for Case 4 (70 Nm, inner race fault)

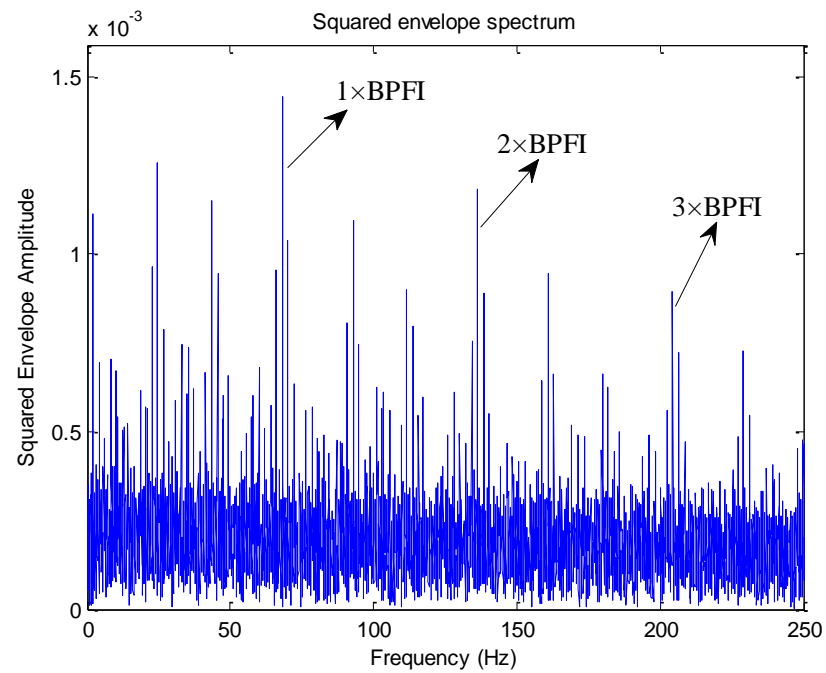


Fig. 5.14 Squared envelope spectrum from Fast Kurtogram for Case 4 (70 Nm, inner race fault)

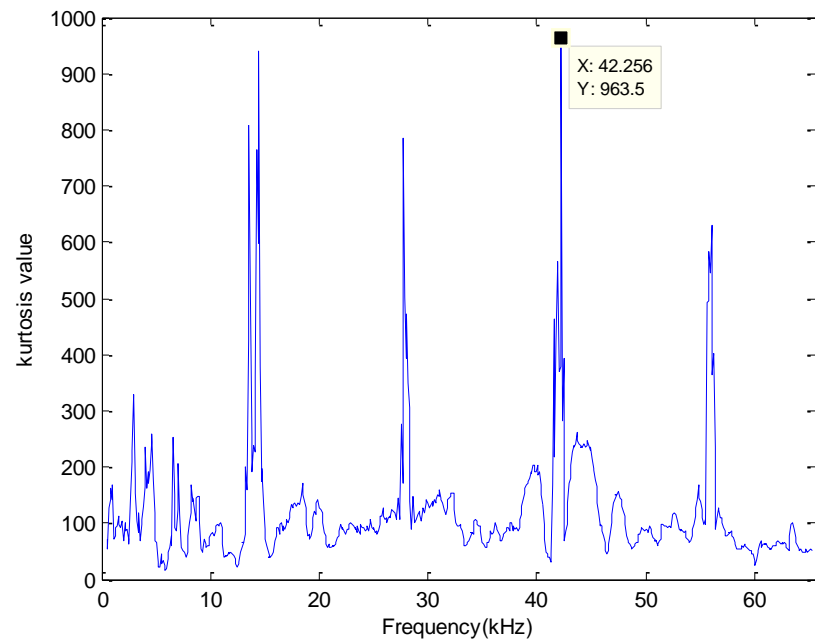


Fig. 5.15 Protrugram for Case 4 (70 Nm, inner race fault)

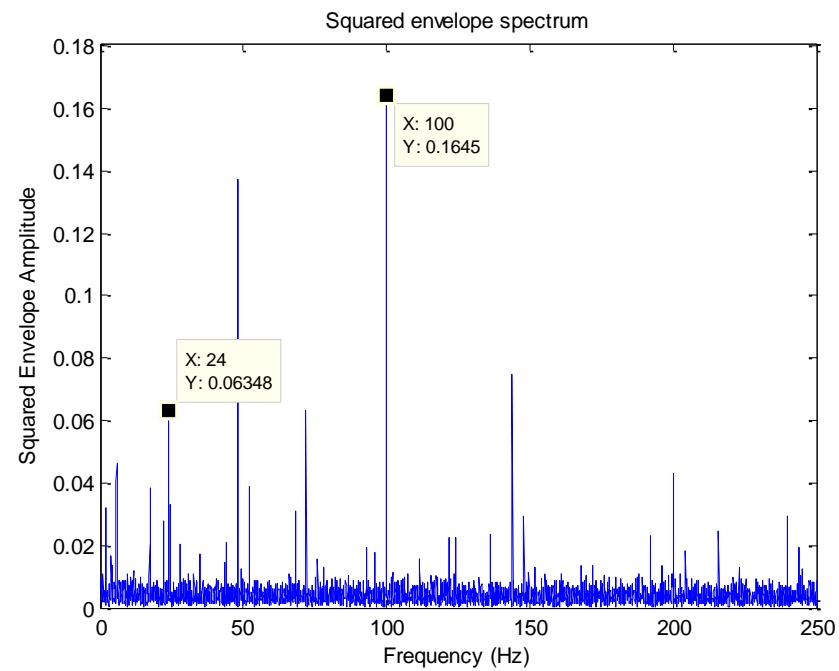


Fig. 5.16 Squared envelope spectrum from Protrugram for Case 4 (70 Nm, inner race fault)

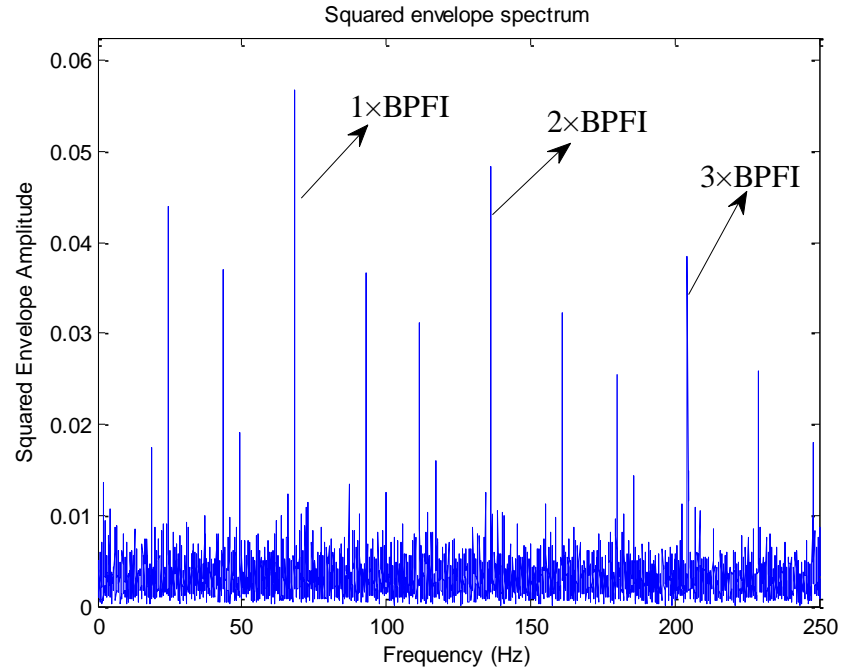


Fig. 5.17 Squared envelope spectrum from Protrugram (The maximum of the 'hump') for Case 4 (70 Nm, inner race fault)

Fig. 5.18 shows the Fast Kurtogram for Case 5 (50 Nm torque, inner race fault), which gives optimal demodulation band parameters of $CF = 47104$ Hz and $BW = 4096$ Hz. As shown in Fig. 5.19, the fault information can be extracted from the envelope spectrum, but the EMI component at 100 Hz is dominant, and the diagnosis is not particularly clear.

Fig. 5.20 presents the Protrugram for Case 5 (50 Nm torque, inner race fault), the optimal CF is chosen as 27756 Hz which is near the second harmonic of switching frequency (28 kHz), and the related envelope spectrum (Fig. 5.21) is dominated by the EMI components of 24 Hz, 100 Hz and their harmonics.

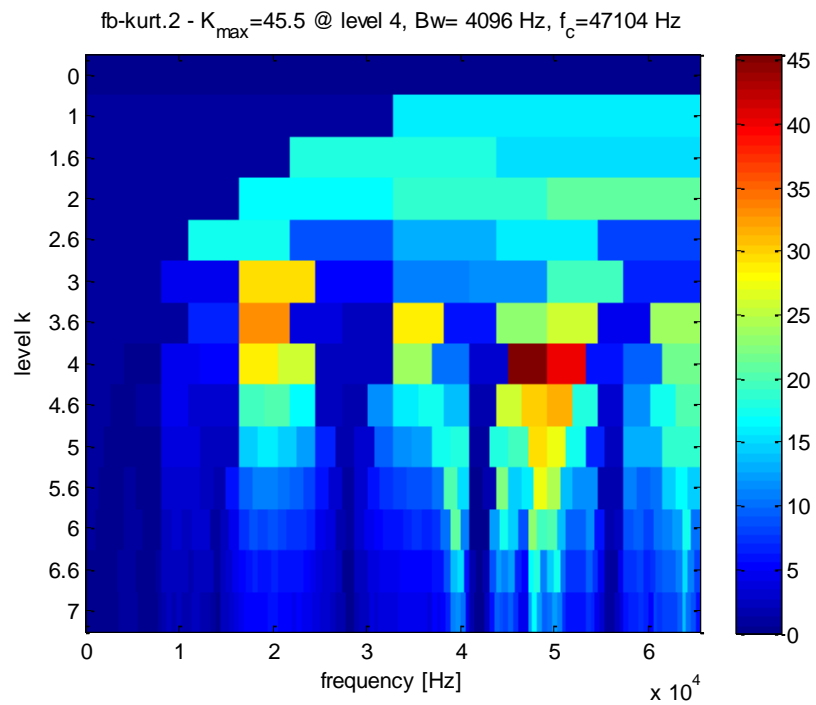


Fig. 5.18 Fast Kurtogram for Case 5 (50 Nm, inner race fault)

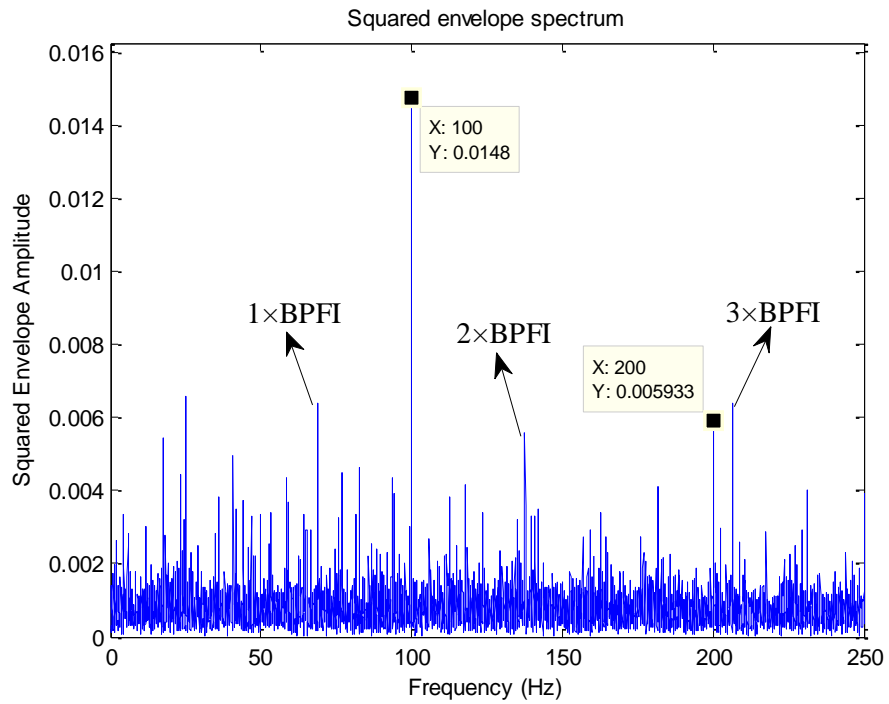


Fig. 5.19 Squared envelope spectrum from Fast Kurtogram for Case 5 (50 Nm, inner race fault)

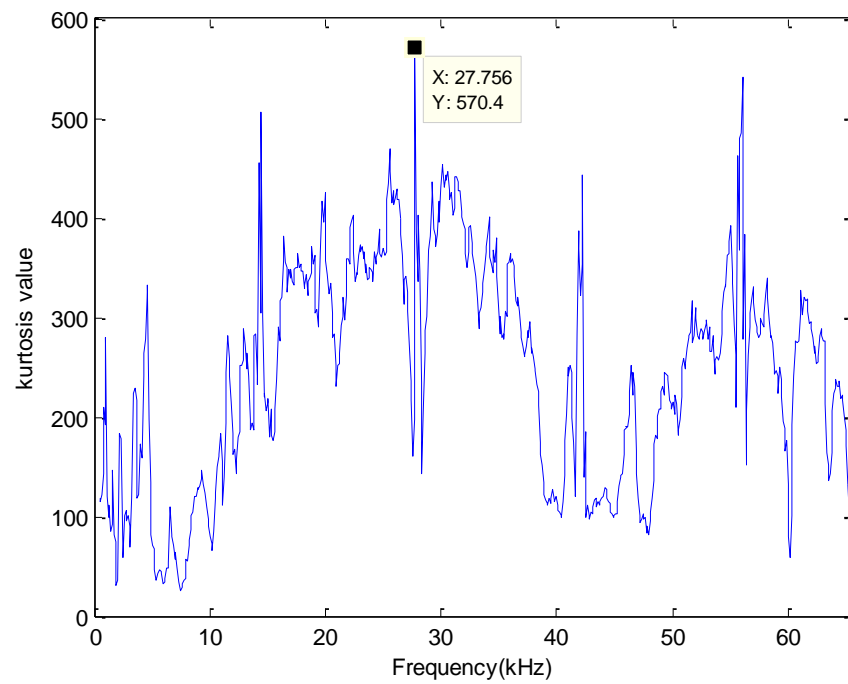


Fig. 5.20 Protrugram for Case 5 (50 Nm, inner race fault)

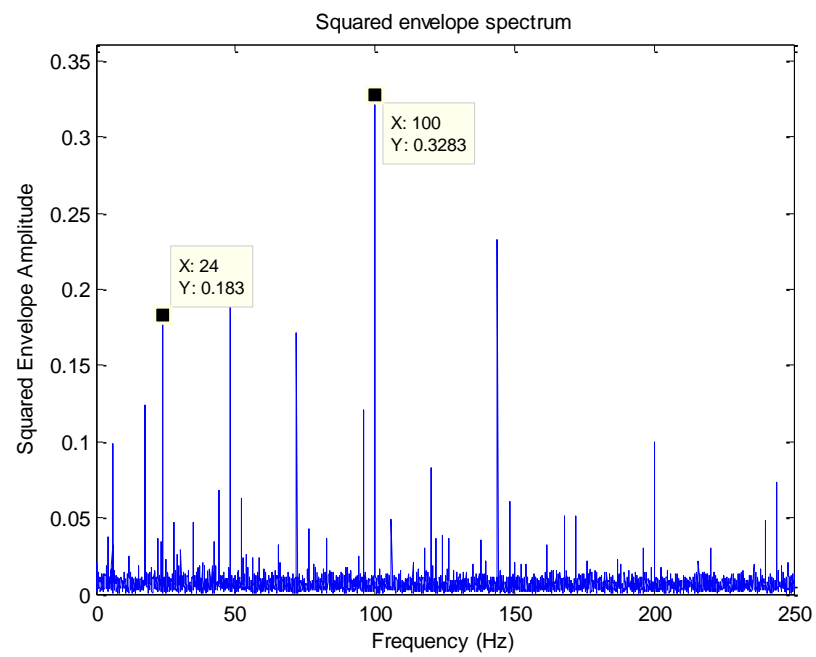


Fig. 5.21 Squared envelope spectrum from Protrugram for Case 5 (50 Nm, inner race fault)

5.5 Introduction of the new presented method 'Kurtrugram'

The poor diagnostic performance of the Kurtogram in some cases and the Protrugram in all cases, as presented above, led to the development of an improved optimal band selection method called the Kurtrugram in this study. It was found here to select demodulation bands with proper bearing fault information, even though, the raw vibration signals were strongly masked by EMI. The method is thought to be sufficiently general to apply to any situation where wideband masking signals are present, where the Kurtogram and Protrugram may prove unsuccessful.

A flow chart of the Kurtrugram method is shown in Fig. 5.22. As with the Protrugram, the method first requires setting of the desired bandwidth for demodulation. Based on the suggestions in [63], it is recommended here to set the bandwidth as narrow as possible but to include at least the first three harmonics of the bearing characteristic fault frequency. The idea here is that because the EMI occupies such a wide frequency range (several kilohertz), minimizing the bandwidth maximizes the signal-to-noise ratio. This may not be correct if the bandwidth of the resonance(s) excited by the bearing fault signal is itself very broad, but even in such cases, the use of a narrow bandwidth gives the possibility of extracting those parts of broad resonances least contaminated by interference.

Next, again like the Protrugram, the optimal center frequency is investigated using a stepping process. The center frequency CF is shifted through a predefined step sp in the range $[BW/2, f_s/2 - BW/2]$, where f_s represents the sampling frequency. For each CF , the signal is bandpass filtered over the range $[CF - BW/2, CF + BW/2]$. The resulting (one-sided) signal is then transformed back to the time domain to obtain the envelope, the kurtosis of which is then calculated and stored. After calculating the kurtosis values for every CF in the range, the optimal center frequency is chosen as the CF with the maximum kurtosis value.

It is worth reiterating that this method takes advantage of core ideas from both the

Fast Kurtogram and Protrugram: the overall process is basically identical to the Protrugram, but the fault indicator – the kurtosis of the envelope (time) signal – is taken from the Fast Kurtogram. This is used here because the fault indicator of the Protrugram (kurtosis of the envelope (amplitude) spectrum) was found to be very sensitive to EMI contamination and is prone to select frequency bands where EMI is dominant (see section 5.4). Thus the process could be described as ‘looking along one row of the Kurtogram’, but with the important point that the step size for determining successive *CF* candidates can be set as desired and is not limited by the bandwidth as it is with the Fast Kurtogram.

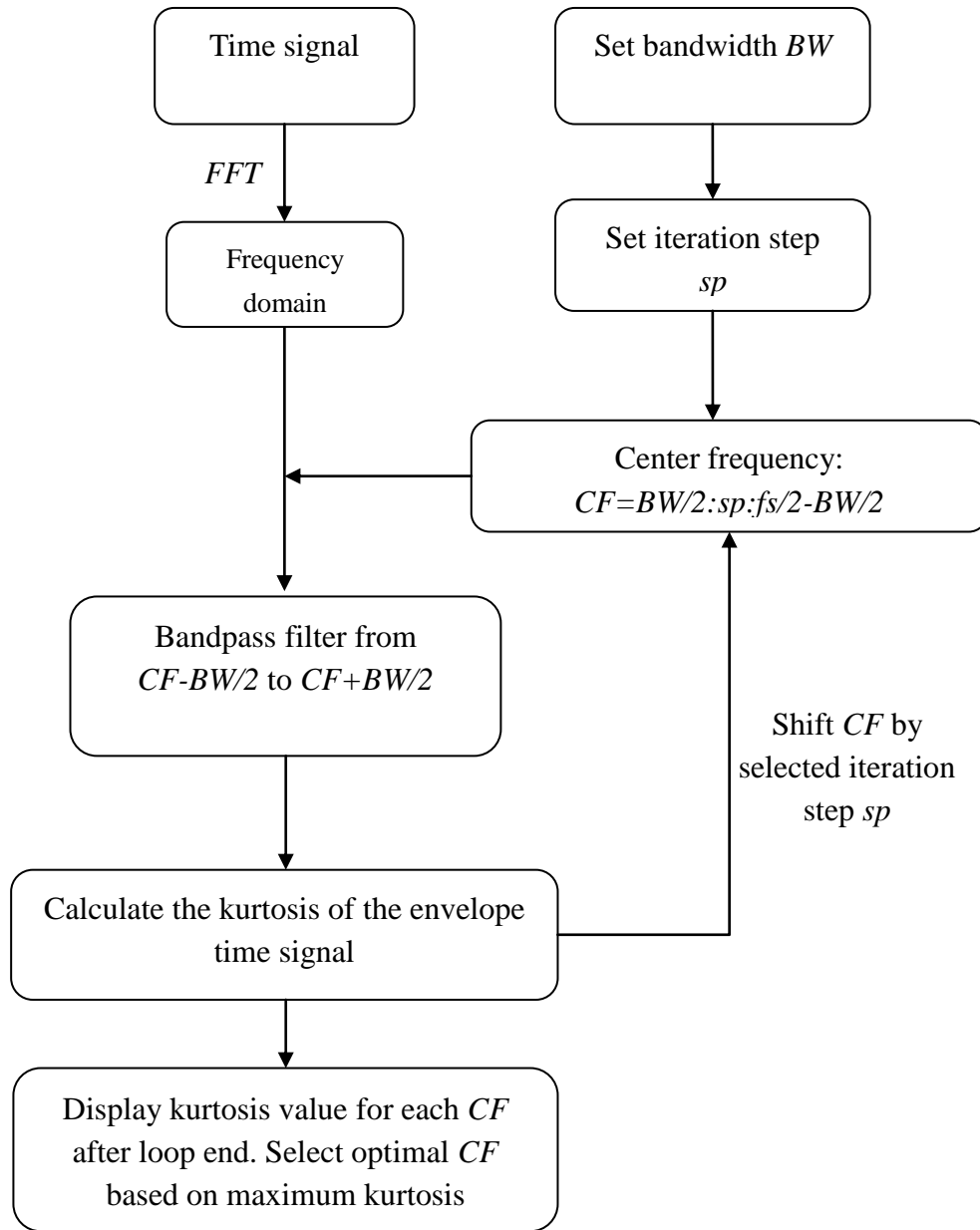


Fig. 5.22 Flow chart of the Kurtrugram

5.6 Results with Kurtrugram

In this section, the effectiveness of the Kurtrugram in detecting bearing faults in the presence of strong EMI is demonstrated using the same data as in section 5.4. For all cases, the bandwidth is set to 512 Hz (which, at approximately $9 \times \text{BPFO}$, is broader than strictly required) and the step size to 100 Hz.

5.6.1 Outer race fault detection

The resulting Kurtrugram for Case 1 (70 Nm torque, outer race fault) is shown in Fig. 5.23, giving a CF of 64656 Hz, which is very close to the band selected by the Fast Kurtogram ($CF=64$ kHz and $BW=1024$ Hz) in section 5.4. The corresponding envelope spectrum is presented in Fig. 5.24, with BPFO harmonics, clearly seen. The envelope spectrum is very similar to that obtained using the Fast Kurtogram (Fig. 5.4).

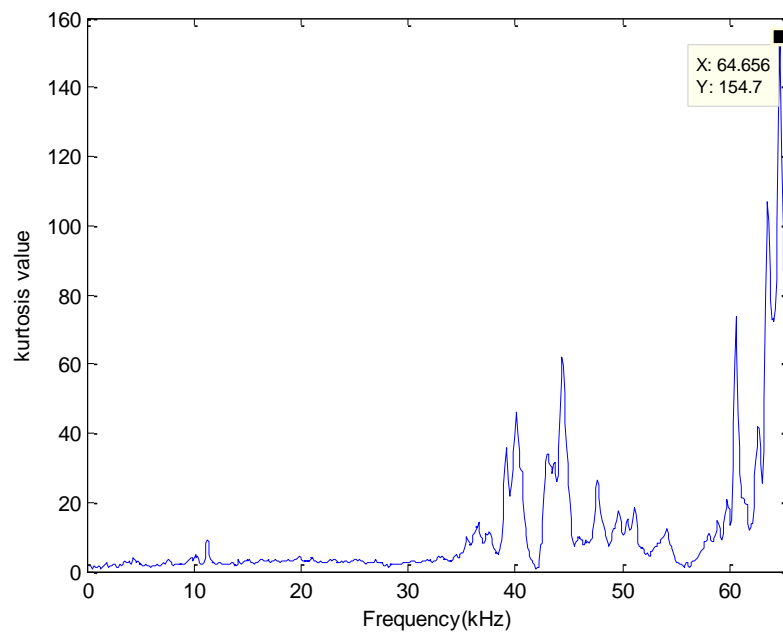


Fig. 5.23 Kurtrugram for Case 1 (70 Nm, outer race fault)

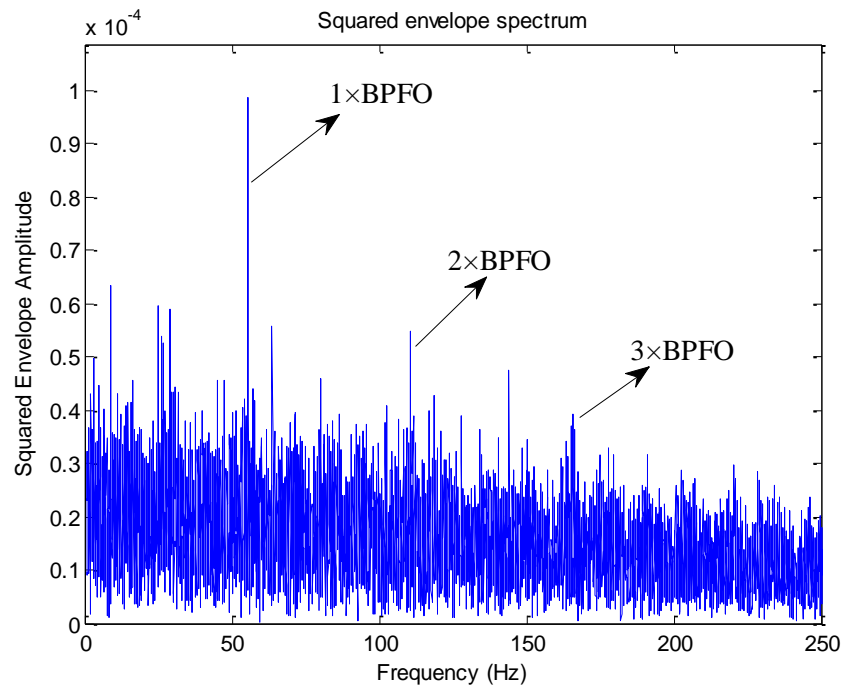


Fig. 5.24 Squared envelope spectrum from Kurtrugram for Case 1 (70 Nm, outer race fault)

Shown in Fig. 5.25 is the Kurtrugram for Case 2 (50 Nm torque, outer race fault), which gives an optimal CF of 40356 Hz, in contrast to the Kurtogram values of $CF=19115$ Hz and $BW=5461$ Hz found in section 4. The Kurtrugram in Fig. 5.25, with a very sharp spike, highlights the value of being able to fine-tune the centre frequency selection by using small step sizes.

The envelope spectrum, in Fig. 5.26, shows clear harmonics of BPFO, albeit with a strong 100 Hz EMI component. By comparison, the envelope spectrum obtained using the Fast Kurtogram (Fig. 5.8) was completely unsuccessful in diagnosing the fault. On closer inspection, it is interesting to note, however, that the Fast Kurtogram of Fig. 5.7 would have delivered a band just over 40 kHz if it had been restricted to a Level 7 bandwidth ($BW=512$ Hz) – i.e. ‘looking along one row’ – and this probably would have given a successful diagnosis. It seems the Kurtogram’s problem in this application is in not restricting the bandwidth and thus allowing too much interference to pass through.

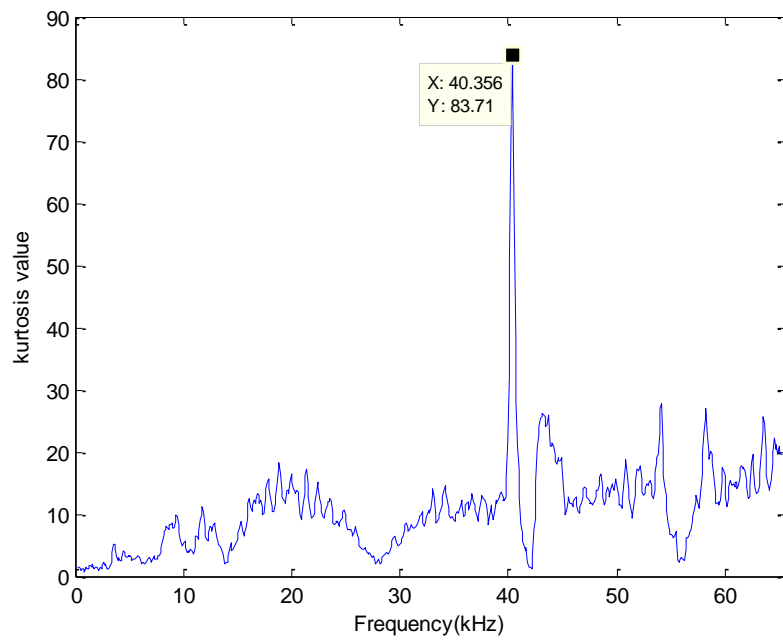


Fig. 5.25 Kurtrugram for Case 2 (50 Nm, outer race fault)

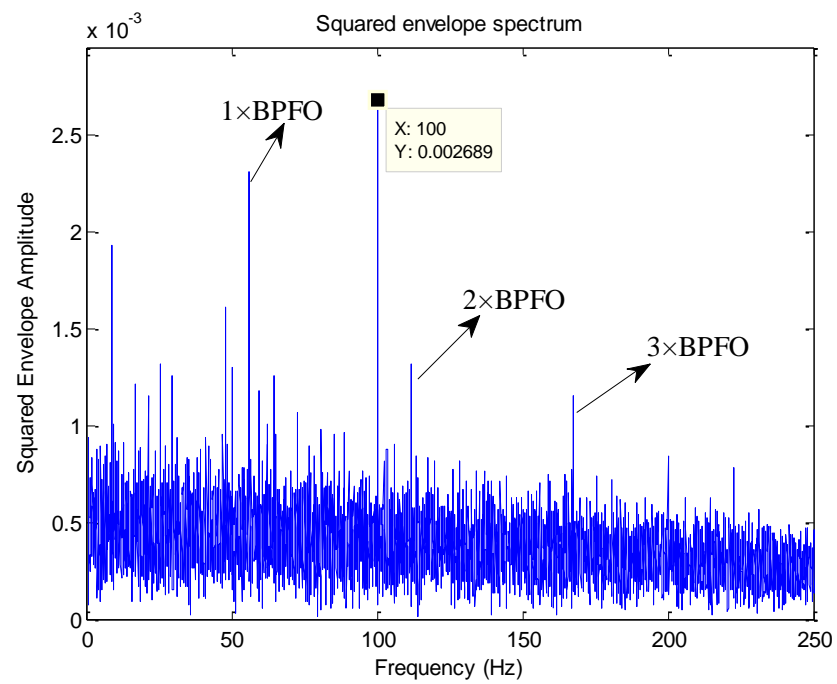


Fig. 5.26 Squared envelope spectrum from Kurtrugram for Case 2 (50 Nm, outer race fault)

5.6.2 Inner race fault detection

As in the section above, the Kurtrugram is applied here with the bandwidth set to 512 Hz and step size to 100 Hz.

The Kurtrugram for Case 4 (70 Nm torque, inner race fault) is shown in Fig. 5.27, giving a CF of 63656 Hz, which, as with Case 1, is very close to the band selected by the Fast Kurtogram ($CF=64512$ Hz and $BW=2048$ Hz) in section 5.4. The corresponding envelope spectrum is presented in Fig. 5.28, with BPFI harmonics clearly seen, surrounded by sidebands at $1\times$ and $12\times$ the planet carrier speed, much like that obtained using the Fast Kurtogram (Fig. 5.14).

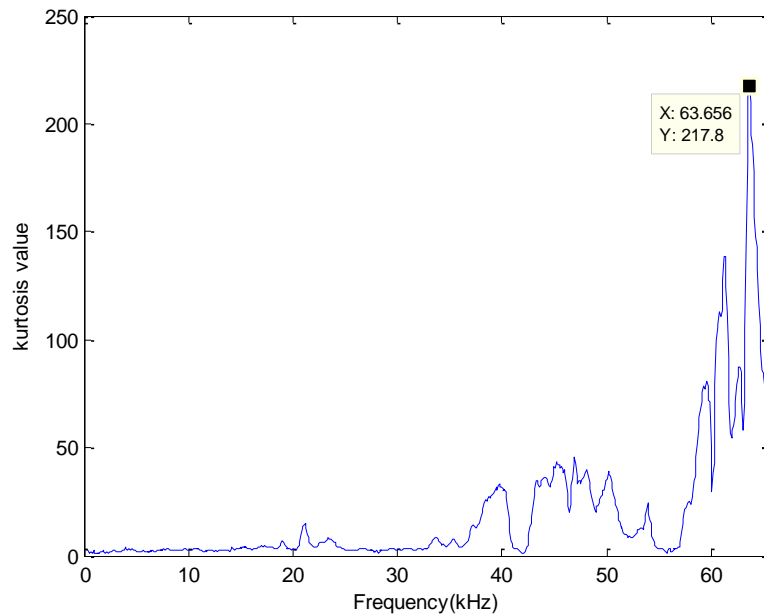


Fig. 5.27 Kurtrugram for Case 4 (70 Nm, inner race fault)

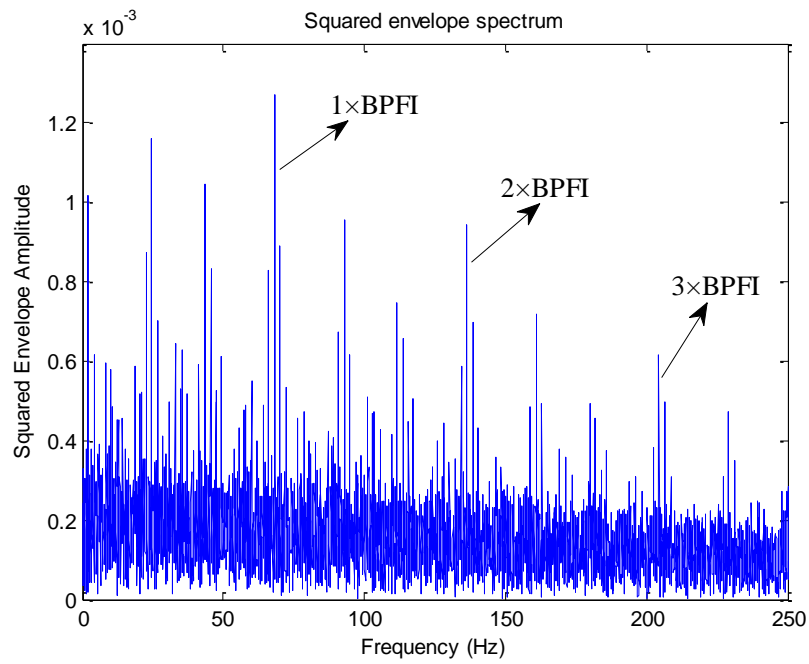


Fig. 5.28 Squared envelope spectrum from Kurtrugram for Case 4 (70 Nm, inner race fault)

The Kurtrugram and envelope spectrum for Case 5 (50 Nm torque, inner race fault) are shown in Fig. 5.29 and Fig. 5.30, respectively. The determined *CF* of 47756 Hz corresponds closely to that obtained with the Fast Kurtogram (*CF*=47104 Hz; *BW* = 4096 Hz). Interestingly, although EMI components of 24 and 100 Hz are still dominant in the envelope spectrum of Fig. 5.30, it gives a much clearer diagnosis than that provided by the Fast Kurtogram (Fig. 5.19). This strengthens the argument that minimising the bandwidth maximises the SNR with this sort of interference.

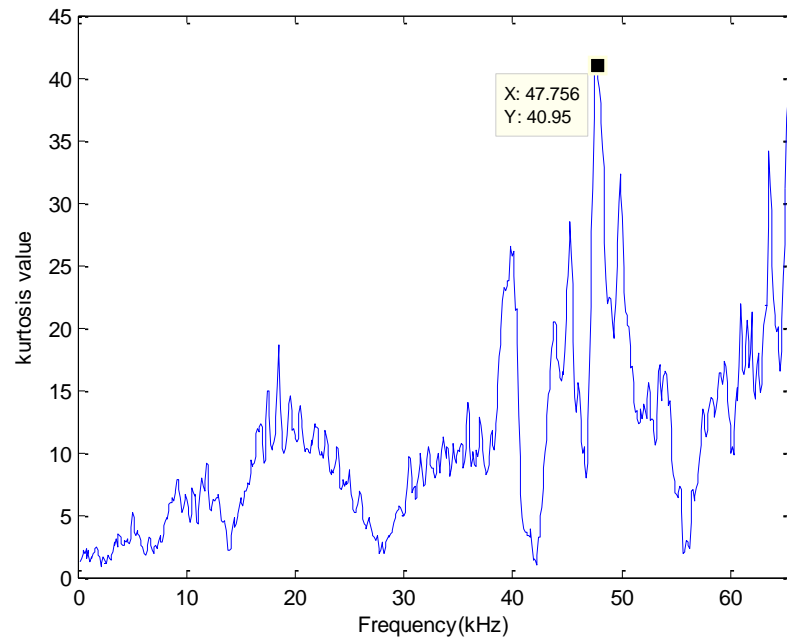


Fig. 5.29 Kurtogram for Case 5 (50 Nm, inner race fault)

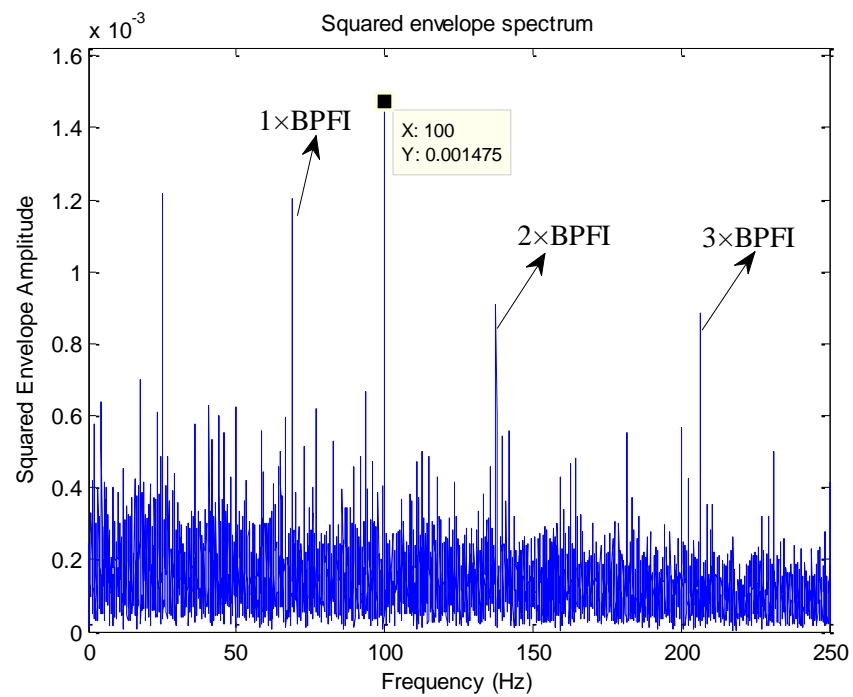


Fig. 5.30 Squared envelope spectrum from Kurtogram for Case 5 (50 Nm, inner race fault)

5.7 Discussions

5.7.1 Comparison of methods

Table 5.3 shows a comparison of the diagnostic performance of the three investigated methods. Cases 1-3 represent the outer race fault with torque loads of 70, 50 and 30 Nm; Cases 4-6 are for the inner race fault with torque loads of 70, 50 and 30 Nm (see Table 5.2). It can be seen that the Kurtrugram diagnosed the fault successfully in all cases, the Fast Kurtogram was successful in half the cases (those with higher load), and the Protrugram was unsuccessful in all cases. The determined optimal demodulation bands are also shown, and it can be seen that all successful diagnoses were based on demodulating very high-frequency bands, in a range of 40-65 kHz. This is perhaps due to the very small size of the bearings (with needle rollers of 2 mm diameter) exciting resonances only at very high frequencies.

Table 5.3 Performance comparisons of the Kurtrugram, Fast Kurtogram and Protrugram

Case	Fault detection performance			Selected optimal demodulation band (kHz)		
	Kurtrugram	Fast Kurtogram	Protrugram	Kurtrugram	Fast Kurtogram	Protrugram
1	Success	Success	Fail	64.4 - 64.9	63.5 - 64.5	14.2 - 14.7
2	Success	Fail	Fail	40.1 - 40.6	16.4 - 21.8	26.0 - 26.5
3	Success	Fail	Fail	43.9 - 44.4	16.4 - 21.8	55.4- 55.9
4	Success	Success	Fail	63.4 - 63.9	63.5 - 65.5	42.0 - 42.5
5	Success	Success	Fail	47.5 - 48.0	45.1 - 49.2	27.5 - 28.0
6	Success	Fail	Fail	44.3 - 44.8	16.4 - 21.8	55.4- 55.9

It is perhaps worth mentioning here the drawbacks of the established methods in this application. The studied EMI-contaminated signals were found to have periodically impulsive (high kurtosis) interference distributed over a broad frequency range. This broadness proved problematic for the Fast Kurtogram because it does not restrict

bandwidth when blindly choosing a demodulation band. Hence it tended to pass rather than filter out the interference. The periodic structure of the impulsivity in the interference caused problems for the Protrugram, whose fault indicator is very sensitive to periodic modulation, which gives an envelope spectrum represented by discrete lines at the modulation frequency and thus a very high kurtosis. These two drawbacks are overcome with the Kurtrugram, as reflected in the results in Table 5.3.

5.7.2 Computation time

When introducing the Protrugram, Barszcz and Jabłoński [63] discussed the trade-off between computation time and step size (which affects the potential accuracy of the *CF* result). This same trade-off exists with the Kurtrugram, yet because it is based on the envelope time signal and not the envelope spectrum, one FFT operation is saved in each loop, giving a slight efficiency gain. Overall, the Kurtrugram was found to give about a 2% reduction in computation time compared with the Protrugram. On the other hand, with a step size of 100 Hz and bandwidth of 512 Hz, the Kurtrugram increased the computation time by about 20% compared with the Fast Kurtogram (the Fast Kurtogram code was used only up to Level 7 ($BW=512$ Hz), and with the parameters (*Fast decimated filterbank tree* and *classical kurtosis based on fourth-order statistics*)).

5.7.3 Limitations of the presented method

As with the Protrugram, the Kurtrugram is not a blind method; the demodulation bandwidth must be set based on certain knowledge of the system. It was suggested in Section 5.5 that in the presence of wideband interference, the bandwidth should be as narrow as possible but should include at least the first three harmonics of the bearing characteristic fault frequency. On the other hand, in the presence of narrowband

interference, a large bandwidth may be advantageous, and this would be very straightforward with the Kurtrugram.

5.8 Summary

The Fast Kurtogram and Protrugram are well-established bearing diagnostics tools, but it has been shown here that they do not deal well with forms of wideband interference, in this case, electromagnetic interference (EMI) from a variable frequency drive (VFD). This chapter proposes a new method called the Kurtrugram, designed to overcome the shortcomings of the other methods in dealing with EMI-contaminated signals. The Kurtrugram procedure uses the same basic architecture as the Protrugram, in which the desired demodulation bandwidth is first set and then the optimal center frequency is selected through a stepping process. However, like the Fast Kurtogram, the Kurtrugram uses as a fault indicator the kurtosis of the envelope time signal rather than the kurtosis of the envelope spectrum. The main idea behind the method is that because the interference is wideband, by specifying as narrow a bandwidth as possible, the signal to noise ratio is maximised, which then allows identification of the bearing fault information. The effectiveness of the method was demonstrated using EMI-contaminated vibration signals collected from a planetary gearbox test rig with planet bearings seeded with outer and inner race faults, and the new method was found to outperform the Fast Kurtogram and Protrugram in all cases, suggesting great potential for bearing diagnostics in cases with intense EMI or other wideband masking signals.

CHAPTER 6 A HYBRID BEARING DIAGNOSTIC APPROACH BASED ON INTERNAL SENSOR MEASUREMENT

6.1 Introduction

In chapter 5, a new SK based demodulation band selection method 'Kurtrugram' was introduced and proved to be successful in demodulation band selection under the condition of intense EMI. In this chapter, this new method is further utilized with several advanced signal processing techniques for detecting a series of planetary bearing faults seeded in the hunting tooth planetary gearbox. As previously reviewed in chapter 2, the bearing fault detection in the planetary gearbox (especially for inner race fault and rolling element fault) is complex due to several reasons. They are (a) the bearing fault signals is masked by deterministic signals (gear signals) in a wide frequency range, (b) signals from the planet gear bearings must be transmitted through a time-varying path to an externally mounted sensor. As the application of an internally mounted sensor, the issues of time-varying transmission path and the masking with the deterministic signal can be largely solved [14], but this internal sensor-based measurement introduces strong EMI into the collected vibration data and this EMI signal negatively affects the bearing fault detection. For instance, based on some primary experimental results presented in chapter 5, the narrow bandwidth demodulation based signal processing techniques (such as Fast Kurtogram) were difficult to be utilized in this case. Although the signal to noise ratio (SNR) was greatly increased through narrowing the demodulation bandwidth and the bearing fault related components were easier to be extracted, the intense EMI misled the selection of the demodulation band. This means there is no bearing fault information in the automatically selected demodulation band, and thus the bearing fault may not be recognized.

With the aims of solving the aforementioned EMI problems raised by the internal sensor-based measurement and further highlighting the performance of internal sensor-based measurement in planetary bearing faults detection, this chapter presents a hybrid signal processing approach for fault diagnosis of planetary bearings using an internally mounted accelerometer. This approach combines several advanced signal processing techniques, such as Cepstrum whitening, minimum entropy deconvolution (MED), Kurtrugram (mainly introduced in chapter 5) and envelope analysis. The adverse effect of EMI is mainly tackled by the new SK based technique 'Kurtrugram'. The vibration data collected by the externally mounted accelerometer is also employed in this chapter as a comparison.

For the rest of this chapter, section 6.2 mainly introduces the procedure for the presented bearing diagnostic approach and illustrates the purposes for utilizing each signal processing technique. Section 6.3 describes the basic information about the measured vibration signal including the experimental tools, faulty bearings, setting of test conditions and the calculations of some key frequency components. Section 6.4 shows the experimental results of the proposed signal processing approach for both the inner race faults and the outer race faults. A further discussion is presented in section 6.5 for showing the effectiveness of the presented approach, the fault detection performances of both internal and external accelerometers are compared in this section.

6.2 Planetary bearing diagnostic procedures

As shown in Fig. 6.1, the captured internal vibration signal for bearing fault detection consists of several main components including deterministic gear signals, random noise, electromagnetic interference and the bearing fault signal.

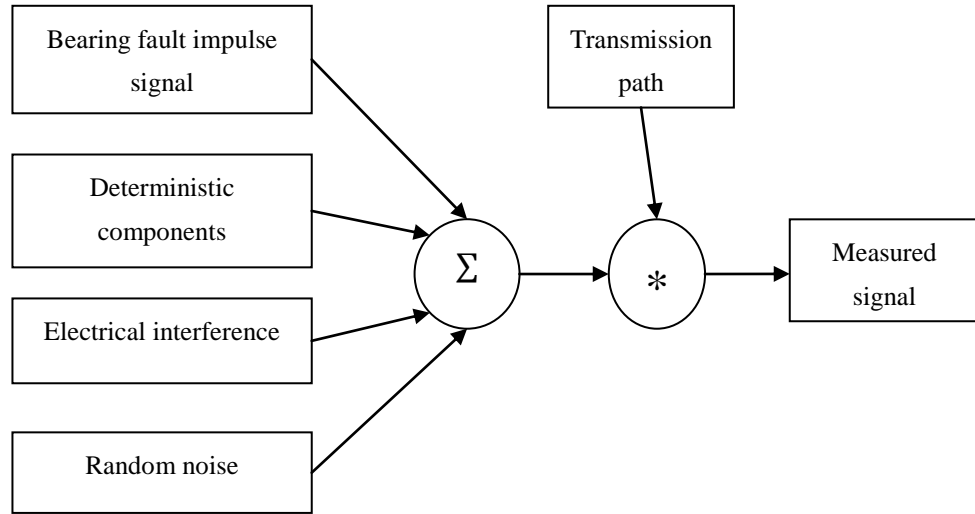


Fig. 6.1 Main components of a measured signal using an internal accelerometer

To filter out undesired components in the measured signal and to improve the signal to noise ratio (SNR) for bearing fault diagnosis, a hybrid signal processing approach is developed as shown in Fig. 6.2. Through the comparison of different techniques for separating the deterministic and random signal in chapter 4, Cepstrum pre-whitening, which has the best performance in lowering the energy level of EMI signal, is selected as the first step for removing the discrete frequencies from the raw vibration signal. Minimum entropy deconvolution (MED) is then used to remove the effect of the transmission path and to enhance the bearing fault related impulsiveness. Since the well-known Fast Kurtogram is easily affected by the large spectral kurtosis (SK) value associated with the electrical interference (detailed introduced in chapter 5), the selection of the demodulation band may be confused by the results of the Fast Kurtogram. Instead, the novel method Kurtrugram is utilized as the third step for the selection of the demodulation band under the condition of intense EMI. Envelope analysis is the final step in the extraction of bearing fault information in the envelope spectrum.

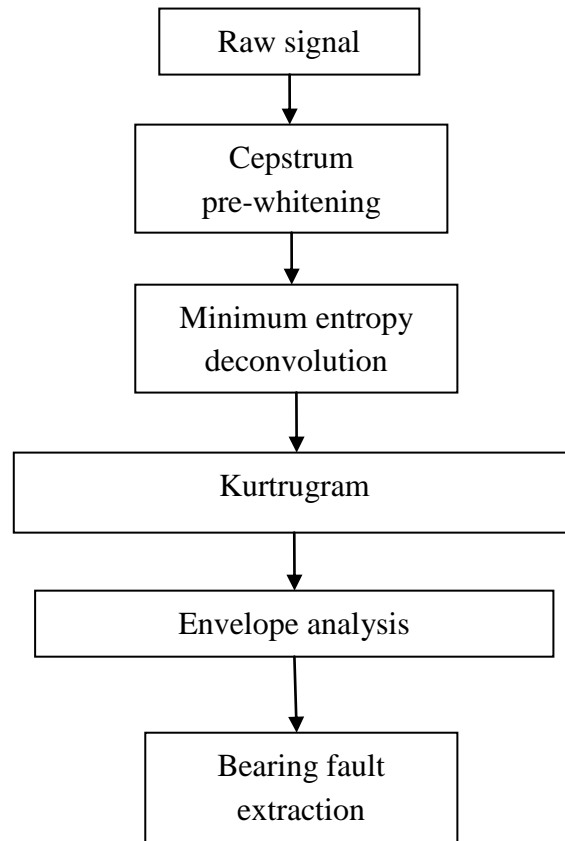


Fig. 6.2 Flow chart of the procedure developed for bearing fault diagnosis based on internal sensor measurements

In order to testify the effectiveness of the presented approach for the internal sensor-based measurement, a series of tests are conducted on a specially designed planetary gearbox test rig. Details of the measured bearing fault signal are introduced in the section 6.3, and the experimental results are presented in section 6.4

6.3 Vibration signal description

6.3.1 Test equipment

The planetary gearbox test rig and the data collection system used for the experiments are detailed introduced in chapter 3. In this study, two sets of Brüel & Kjær 4394

IEPE-type accelerometers were installed in the hunting tooth planetary gearbox for both the internal and external vibration measurements. The internal accelerometer was mounted on the planet carrier in the axial direction, and the external accelerometer was installed on the top of the ring gear. Since the internal accelerometer rotates with the planet carrier, a Michigan Scientific B6-2 slip ring was used for transmitting the vibration signal from the internal accelerometer to the signal conditioner. A Brüel & Kjær PULSE front end was connected to a laptop running B&K Labshop for data capturing and recording. The recorded data can then be exported to MATLAB for further signal processing.

6.3.2 Bearing fault information

Both the inner race fault and outer race fault were seeded in the planet gear bearings in this study. IKO NAF 122812 needle roller bearings (see Table 6.1) were used as the planet gear bearings. Each contained 11 roller pins of 3 mm diameter, and the bearing pitch diameter was 19 mm. The technique of electric spark erosion was used for the fault seeding in both the inner race and outer race. The widths of notches in the outer race were 0.4, 0.8, 1.2 and 1.6 mm with a depth of 0.4 mm, and the notches on the inner races were same as the outer race notches.

Table 6.1 Planet gear bearing parameters

Type	IKO NAF 122812
Needle roller diameter (d)	3 mm
Pitch circle diameter (D)	19 mm
Number of rolling elements (n)	11
Contact angle (β)	0°

6.3.3 Test conditions

During the operation of the gearbox rig, based on the test parameters setting presented in [14, 27, 43], testing was conducted at a constant input shaft speed of 4 Hz

(setting by variable frequency drive) and a constant torque load of 40 Nm. Also, testing with bearings in different status (good bearing, inner race fault bearing, outer race fault bearing) were conducted. In each test, the vibration signals were collected for both the internal accelerometer and external accelerometer. In addition, the tacho signal collected by shaft encoder was applied for tracking the actual input speed. The sampling frequency was set as 131072 Hz. Details of experiment conditions for the test rig is presented in Table 6.2.

Table 6.2 Test conditions of the gearbox rig

Test number	Input shaft Speed (Hz)	Load (Nm)	Bearing status	Defect size (mm)
1	3.70	40	Good	0
2	3.72	40	Outer race fault	0.4
3	3.72	40	Outer race fault	0.8
4	3.71	40	Outer race fault	1.2
5	3.72	40	Outer race fault	1.6
6	3.71	40	Inner race fault	0.4
7	3.72	40	Inner race fault	0.8
8	3.70	40	Inner race fault	1.2
9	3.71	40	Inner race fault	1.6

6.3.4 Planetary gearbox calculations

6.3.4.1 Components frequency calculations

The gear arrangements of the planetary gearbox are shown as follows:

Pinion gear tooth number (Input shaft): $N_{pin}=42$

Wheel gear tooth number (Meshed with the pinion gear): $N_w=55$

Ring gear tooth number: $N_r= 80$

Planet gear tooth number: $N_p= 23$

Sun gear tooth number: $N_s= 34$

Based on the gear above arrangements, the key frequency components of the planetary gearbox could be calculated as follows (f_i is the actual input speed):

Carrier spin frequency (f_c):
$$f_c = -f_i \times \frac{N_{pin}}{N_w} = 0.76f_i$$

Planet gear spin frequency (f_p):
$$f_p = f_c \times \frac{N_r}{N_p} = 2.64f_i$$

Sun gear spin frequency (f_s):
$$f_s = f_c \times \left(\frac{N_r}{N_s} + 1 \right) = 2.55f_i$$

Spur gear mesh frequency (f_{sgm}):
$$f_{sgm} = f_i \times N_{pin} = 42f_i$$

Planet gear mesh frequency (f_{pgm}):
$$f_{pgm} = f_c \times N_r = 60.8f_i$$

6.3.4.2 Bearing fault frequencies

The theoretical equations for calculating the characteristic frequencies of both the inner race fault and outer race fault are illustrated in chapter 5. In this case, with a real input shaft speed of around 3.7 Hz (shown in Table 6.2), the approximate fault frequencies are: $BPFO=45.5$ Hz and $BPFI=62.6$ Hz.

6.4 Experimental results

In this section, the experimental results for two main types of bearing defects (outer race fault and inner race fault) are presented, and both the results of internal sensor measured signal and external sensor measured signal are displayed as comparison.

6.4.1 Outer race fault detection

For the outer race fault detection, the experimental results of the measured vibration signal, which were collected from a series of faulty bearings with different defect sizes (widths of notches in the outer race were 0.4, 0.8, 1.2 and 1.6 mm), are respectively presented from section 6.4.1.1 to 6.4.1.4.

6.4.1.1 1.6 mm defect size

The characteristic frequency for the outer race fault is 45.76 Hz as the actual input shaft speed is 3.72 Hz. In this case, the proposed diagnostic procedure was applied to the vibration signal acquired from the internal accelerometer. As plotted in Fig. 6.3, the impulsiveness of the vibration signal became much clearer after the Cepstrum whitening step and MED filtering because the kurtosis value gradually increased from Fig. 6.3 (a) to Fig. 6.3 (c). The next step was to use the Kurtrugram to look for the best demodulation band. An optimal bandwidth of 512Hz was used on the basis of band selection criteria presented in chapter 5. The Kurtrugram is shown in Fig. 6.4, where the optimal center frequency for demodulation was 52356 Hz identified by its maximum kurtosis value of 67.65. Therefore, the high-frequency band [52100 Hz - 52612 Hz] was chosen as the optimal demodulation band. Envelope analysis was then conducted at the selected high-frequency band for demodulation and fault information pick-up. The outer race fault frequency 46.2 Hz (a slight difference due to actual slip in the bearing) of the planetary bearing could be clearly identified in the envelope spectrum shown in Fig. 6.5. Also, it is noted that the bearing fault frequency is modulated by the planet gear spin frequency of 9.8 Hz. The envelope spectrum for the same band of the good bearing is also presented in Fig. 6.6 as a comparison (note difference in amplitude scale). The dominant frequency components include 156.4 Hz of the spur gear mesh frequency and the 2.85 Hz of carrier spin frequency.

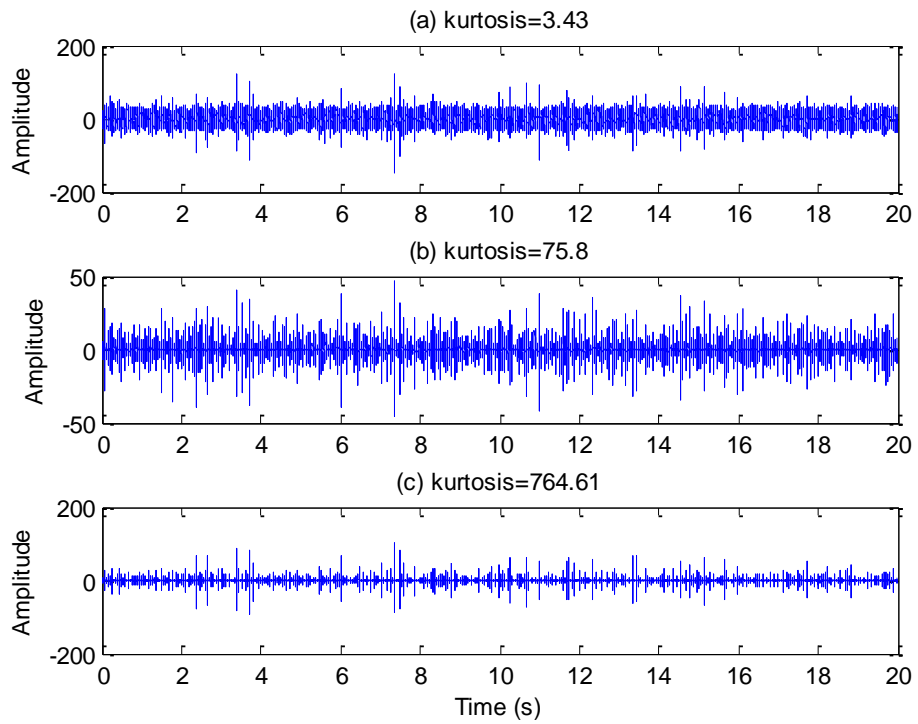


Fig. 6.3 (a) Raw time signal; (b) Cepstrum whitened signal; (c) Signal after Cepstrum whitening and MED filter (45 Nm, 1.6 mm outer race fault, internal sensor)

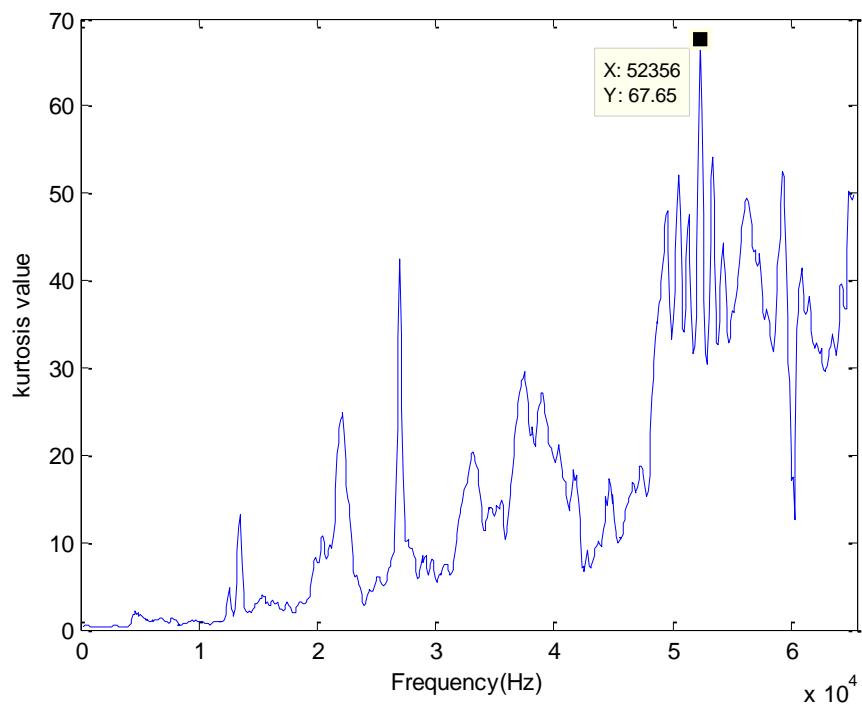


Fig. 6.4 Kurtrugram (1.6 mm outer race fault, internal sensor)

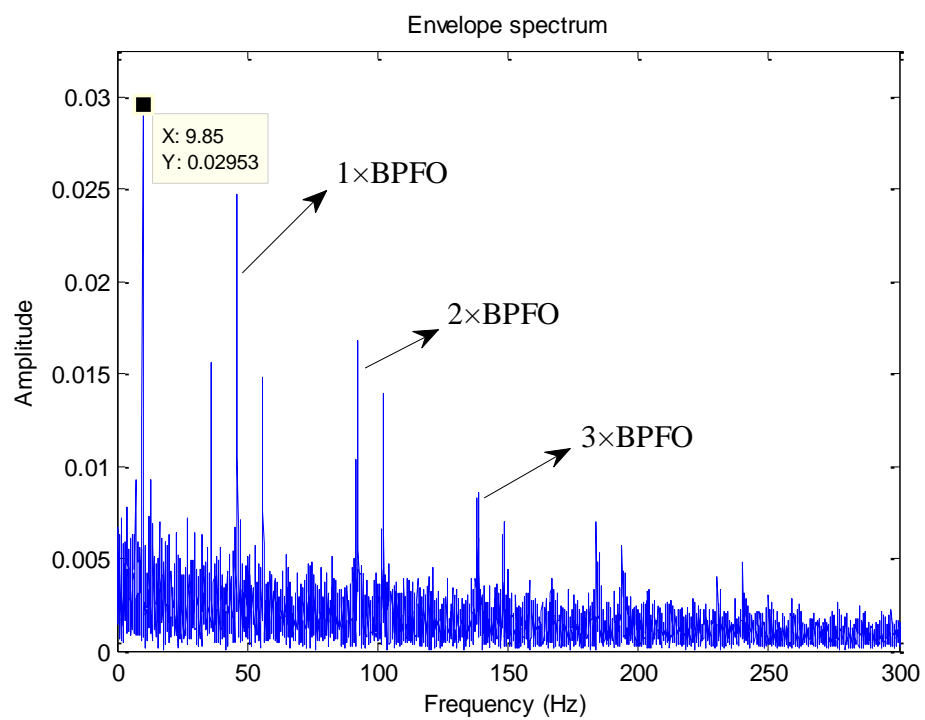


Fig. 6.5 Envelope spectrum (1.6 mm outer race fault, internal sensor)

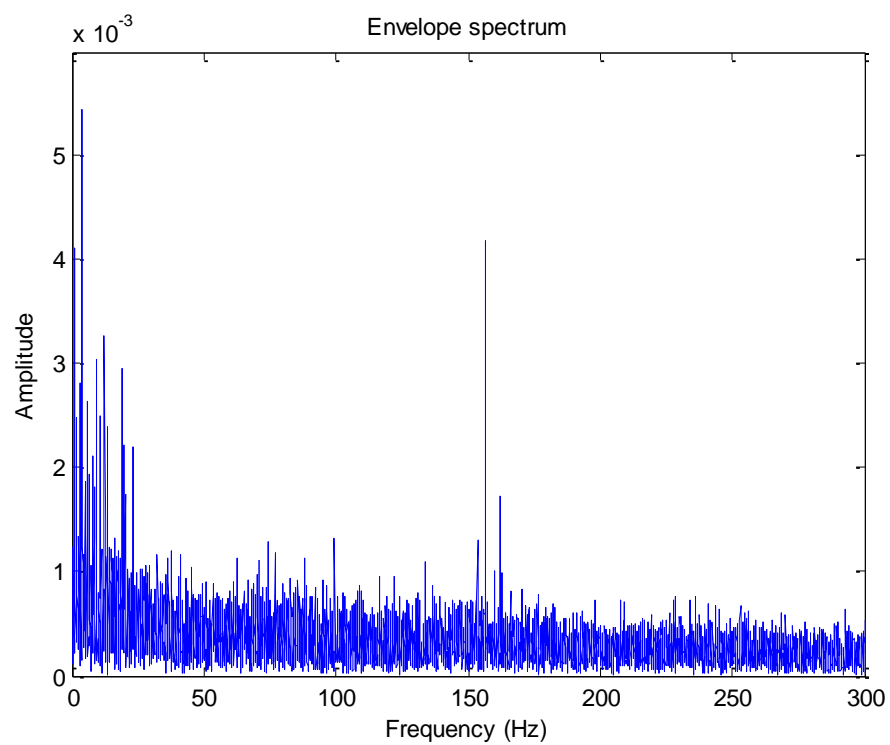


Fig. 6.6 Envelope spectrum (Good bearing, internal sensor)

The Kurtrugram and the squared envelope spectrum of the external sensor-based measurement are presented in Figs. 6.7 and 6.8 respectively. The optimal demodulation bandwidth was set to be 512 Hz, and the optimal center frequency was selected as 44956 Hz due to its maximum kurtosis value of 33.59. The result in Fig. 6.8 showed that the external sensor-based measurement also can recognize the outer race fault in planetary bearings by extracting the bearing fault frequency 46.2 Hz and its harmonics. However, it is also noted that the bearing fault frequency is modulated by the planet gear spin frequency of 9.8 Hz.

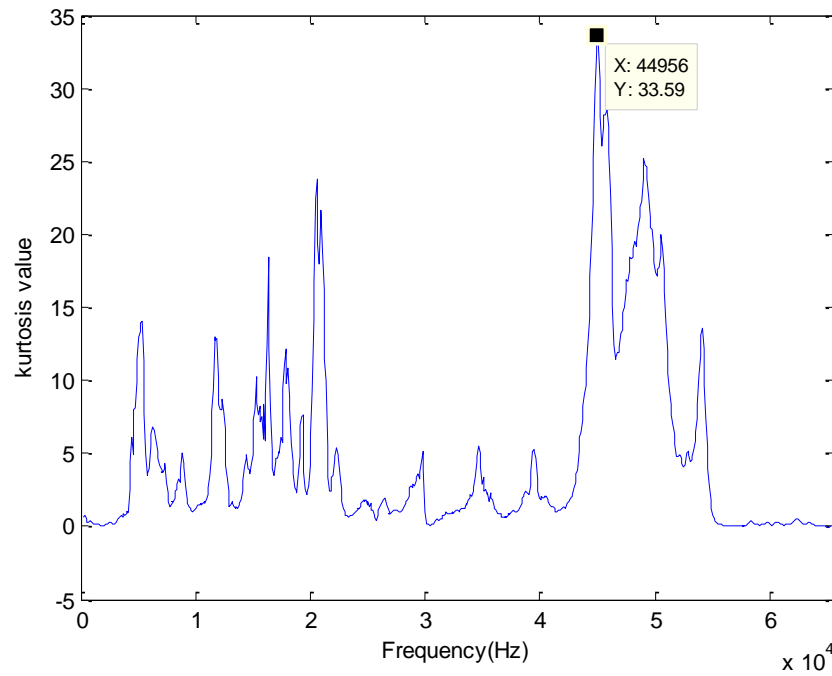


Fig. 6.7 Kurtrugram (1.6 mm outer race fault, internal sensor)

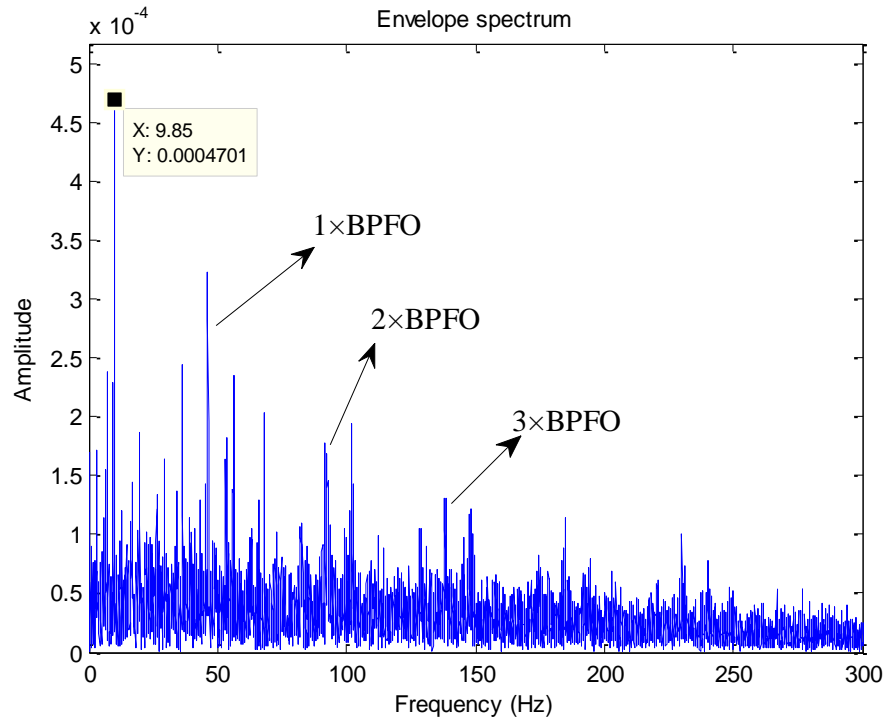


Fig. 6.8 Envelope spectrum (1.6 mm outer race fault, internal sensor)

6.4.1.2 1.2 mm defect size

In this case, the characteristic frequency for the outer race fault is 45.64 Hz as the actual input shaft speed is 3.71 Hz. The proposed diagnostic procedure was applied to the vibration signal obtained from the internal accelerometer. As plotted in Fig. 6.9, the impulsiveness of the vibration signal became much clearer after the Cepstrum whitening step and MED filtering because the kurtosis value gradually increased from Fig. 6.9 (a) to Fig. 6.9 (c). The next step was to use the Kurtrugram to search for the best demodulation band. An optimal bandwidth of 512Hz was used on the basis of band selection criteria. The Kurtrugram is shown in Fig. 6.10, where the optimal center frequency for demodulation is 59356 Hz identified by its maximum kurtosis value of 119.3. Therefore, the high-frequency band [59100 Hz - 59612 Hz] is selected as the optimal demodulation band. Envelope analysis was then utilized at the selected high-frequency band for demodulation and fault information pick-up. The outer race

fault frequency 46.4 Hz (a slight difference due to actual slip in the bearing) of the planetary bearing could be clearly identified in the envelope spectrum shown in Fig. 6.11. Also, the planet gear spin frequency (9.85 Hz) could be recognized. The envelope spectrum for the same band of the good bearing is presented in Fig. 6.12 as a comparison (note difference in amplitude scale). The dominant frequency components include the 2.85 Hz (Carrier spin frequency) and 156.4 Hz of the spur gear mesh frequency.

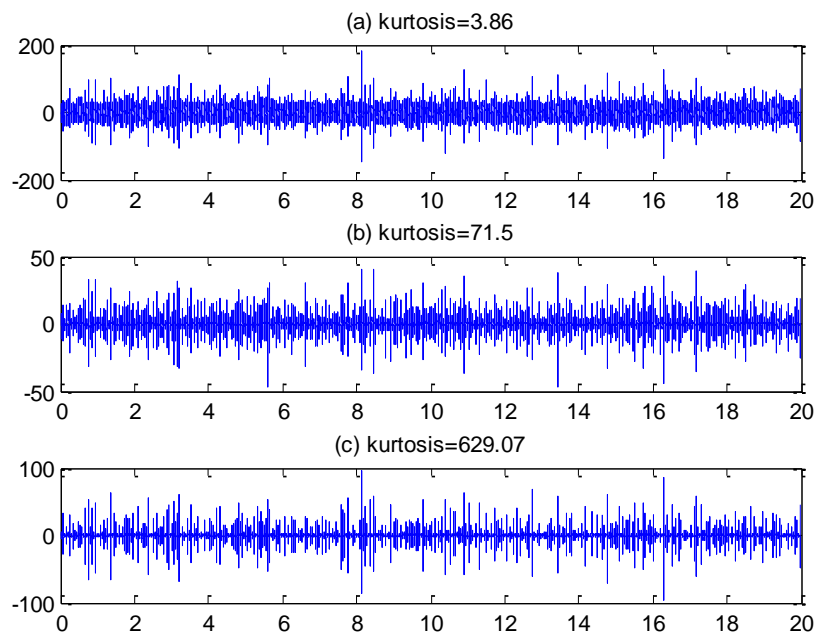


Fig. 6.9 (a) Raw time signal; (b) Cepstrum whitened signal; (c) Signal after Cepstrum whitening and MED filter (1.2 mm outer race fault, internal sensor)

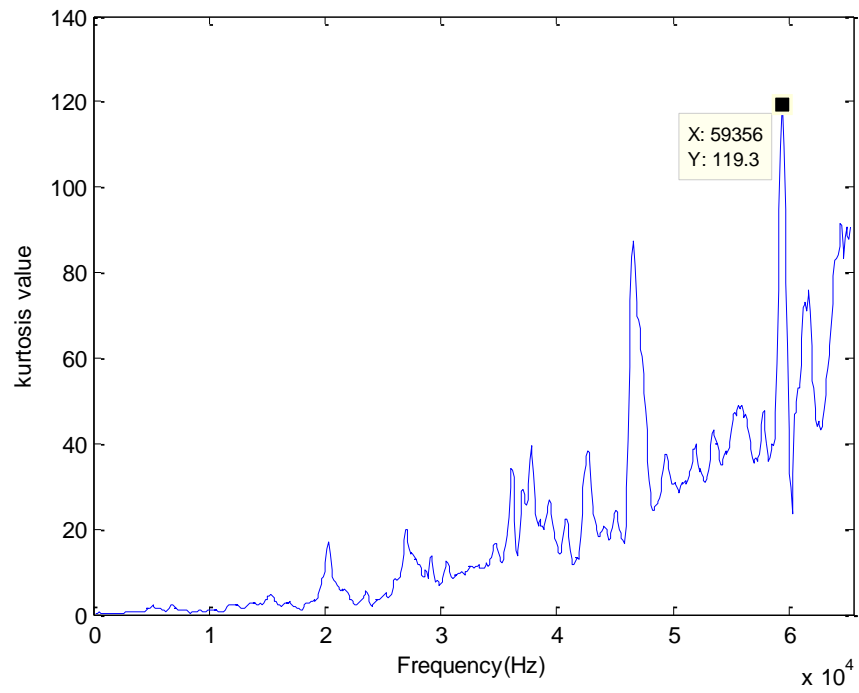


Fig. 6.10 Kurtogram (1.2 mm outer race fault, internal sensor)

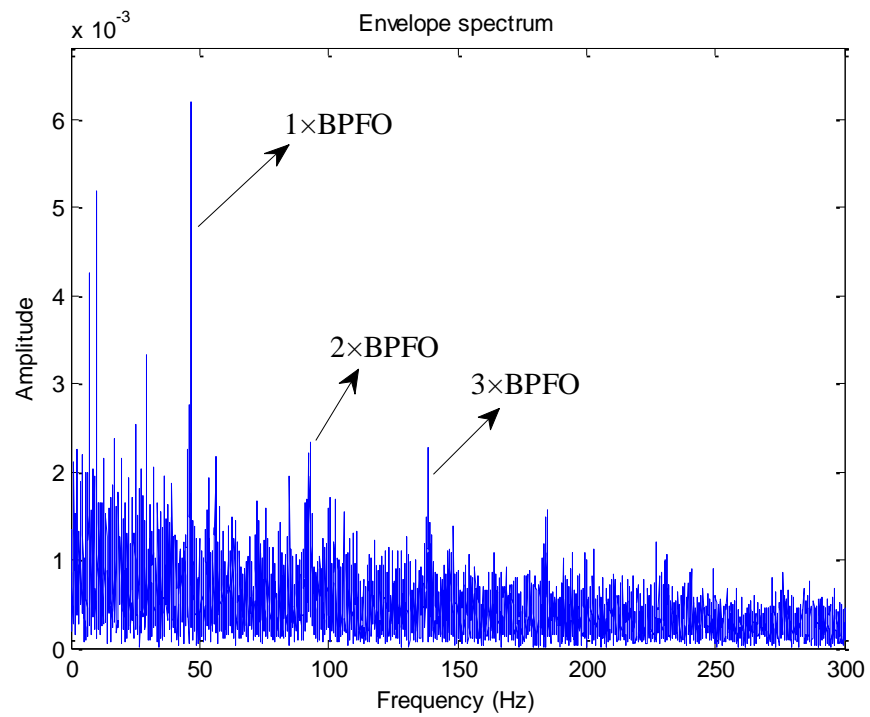


Fig. 6.11 Envelope spectrum (1.2 mm outer race fault, internal sensor)

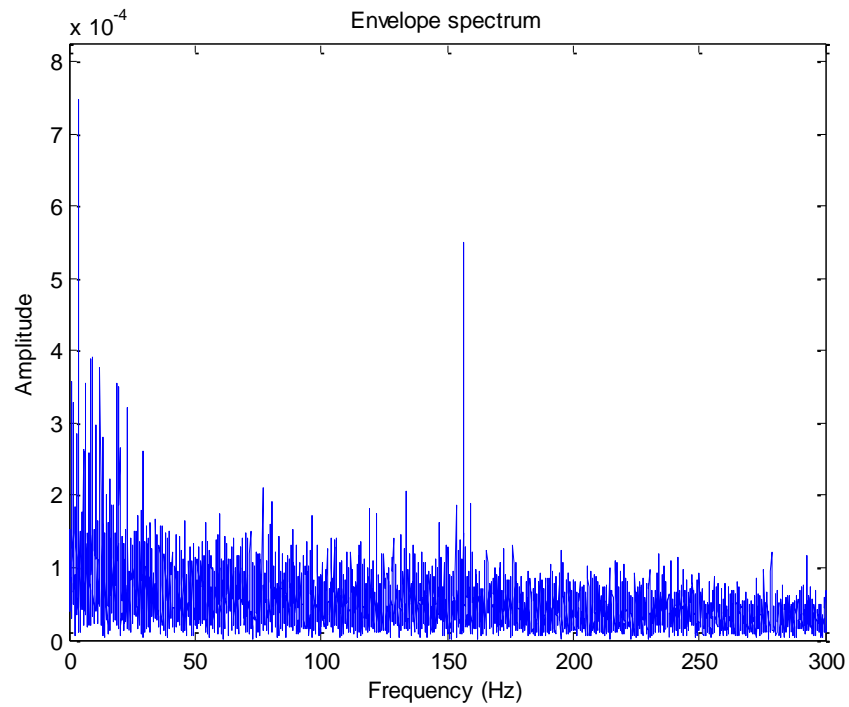


Fig. 6.12 Envelope spectrum (Good bearing, internal sensor)

The Kurtrugram and the squared envelope spectrum of the external sensor-based measurement are presented in Fig. 6.13 and Fig. 6.14 respectively. The optimal demodulation bandwidth was set to be 512 Hz, and the optimal center frequency was selected as 45056 Hz due to its maximum kurtosis value of 36.48. The result in Fig. 6.14 illustrated that the external sensor-based measurement could identify the outer race fault. It is noted that the envelope spectrum is also dominated by the planet gear spin frequency (9.85 Hz) and its harmonics.

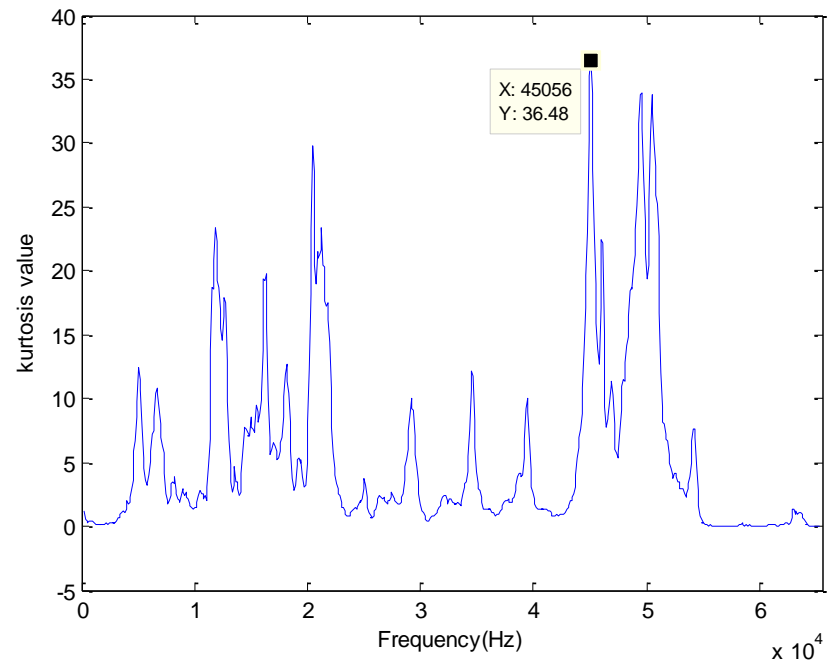


Fig. 6.13 Kurtrogram (1.2 mm outer race fault, external sensor)

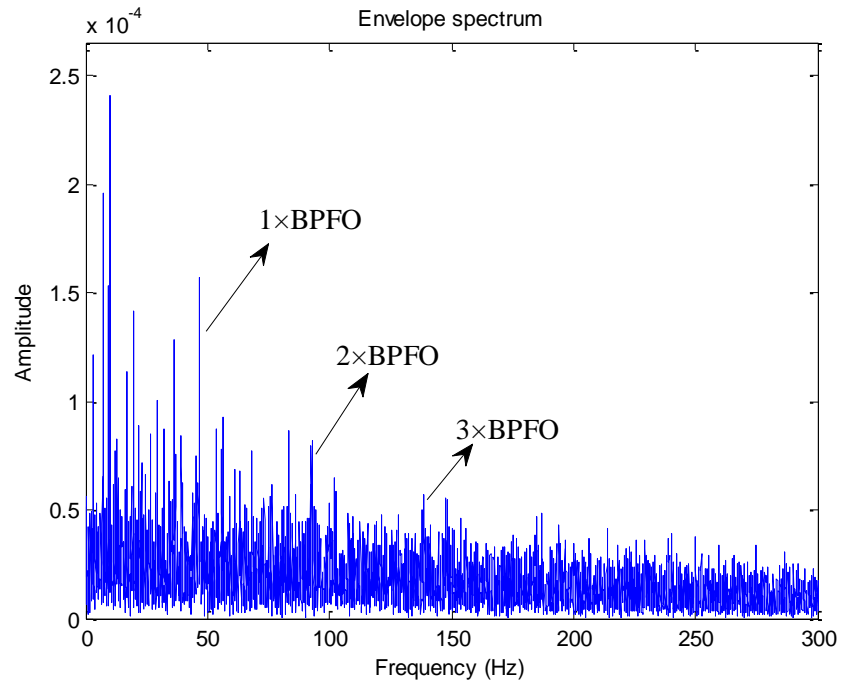


Fig. 6.14 Envelope spectrum (1.2 mm outer race fault, external sensor)

6.4.1.3 0.8 mm defect size

In this case, the characteristic frequency for the outer race fault is 45.76 Hz as the actual input shaft speed is 3.72 Hz. The proposed diagnostic procedure was applied to the vibration signal obtained from the internal accelerometer. As presented in Fig. 6.15, the impulsiveness of the vibration signal became much clearer after the Cepstrum whitening step and MED filtering because the kurtosis value gradually increased from Fig. 6.15 (a) to Fig. 6.15 (c). Kurtrugram was used as the next step in looking for the best demodulation band. The plot of Kurtrugram is shown in Fig. 6.16, where the optimal center frequency for demodulation was 55356 Hz identified by its maximum kurtosis value of 100.5. Therefore, the high-frequency band [55100 Hz - 55612 Hz] was selected as the optimal demodulation band. Envelope analysis was then utilized at the selected high-frequency band for demodulation and fault information pick-up. The outer race fault frequency 46.25 Hz (a slight difference due to actual slip in the bearing) with the modulation frequency of 9.9 Hz (Planet gear spin frequency) could be recognized in the envelope spectrum shown in Fig. 6.17. The envelope spectrum for the same band of the good bearing is also presented in Fig. 7.18 as a comparison (note difference in amplitude scale). The dominant frequency in envelope spectrum is related to the carrier spin frequency of 2.85 Hz. Also, the spur gear mesh frequency (156.4 Hz) could be recognised by a relative lower amplitude.

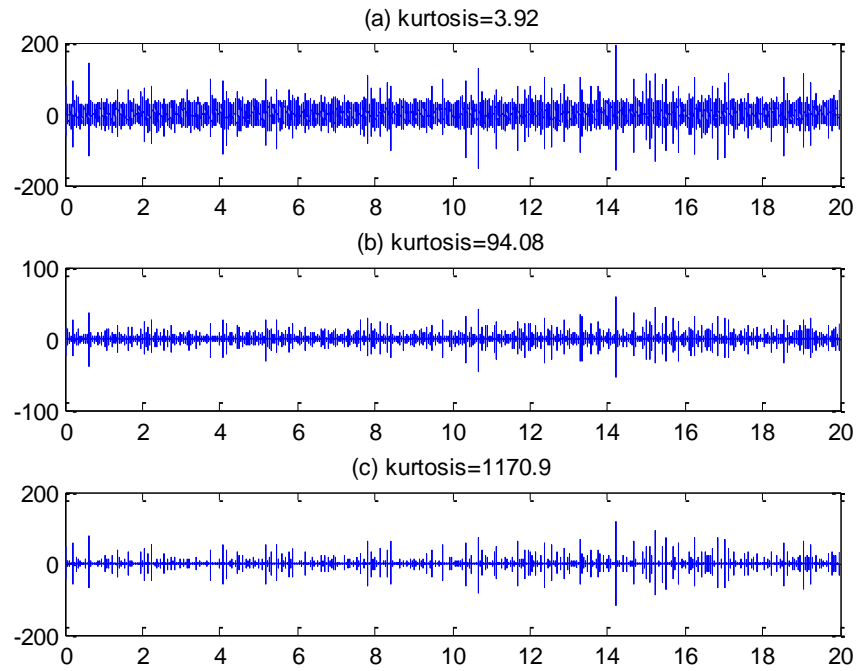


Fig. 6.15 (a) Raw time signal; (b) Cepstrum whitened signal; (c) Signal after Cepstrum whitening and MED filter (0.8 mm outer race fault, internal sensor)

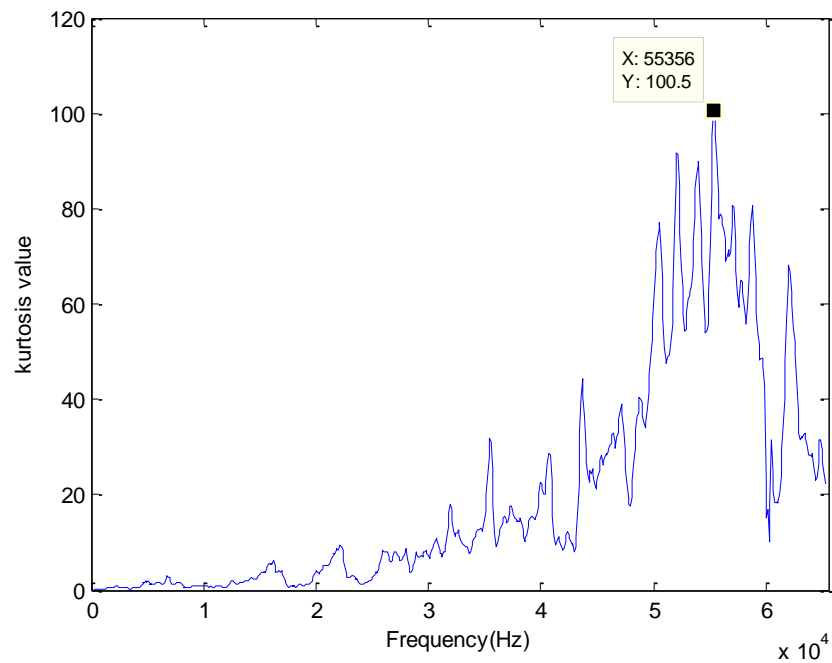


Fig. 6.16 Kurtrugram (0.8 mm outer race fault, internal sensor)

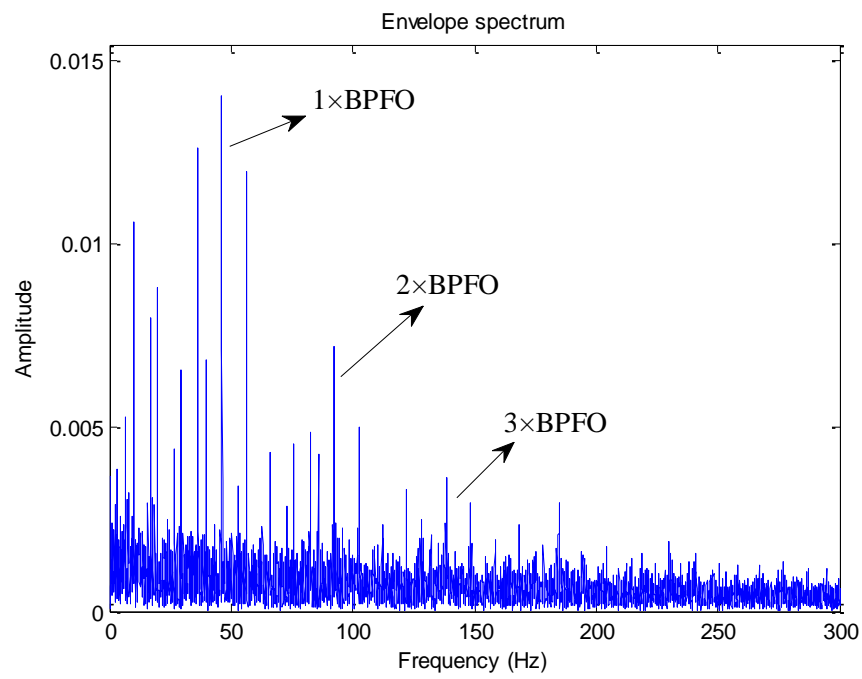


Fig. 6.17 Envelope spectrum (0.8 mm outer race fault, internal sensor)

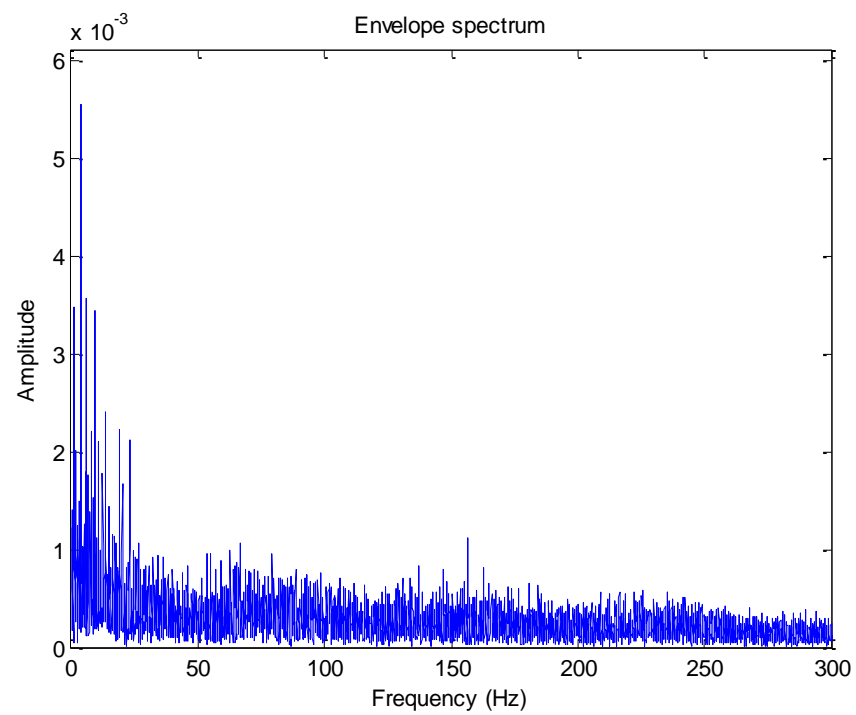


Fig. 6.18 Envelope spectrum (Good bearing, internal sensor)

The Kurtrugram and the envelope spectrum of the external sensor-based measurement are also presented in Fig. 6.19 and Fig. 6.20 respectively. The optimal demodulation bandwidth was set to be 512 Hz, and the optimal center frequency was selected as 50356 Hz due to its maximum kurtosis value of 65.96. The result in Fig. 6.20 shows that the external sensor-based measurement also can recognize the outer race fault in planetary bearings by extracting the bearing fault frequency 46.25 Hz and its harmonics. In addition, the bearing fault frequency components is modulated by the planet gear spin frequency of 9.9 Hz.

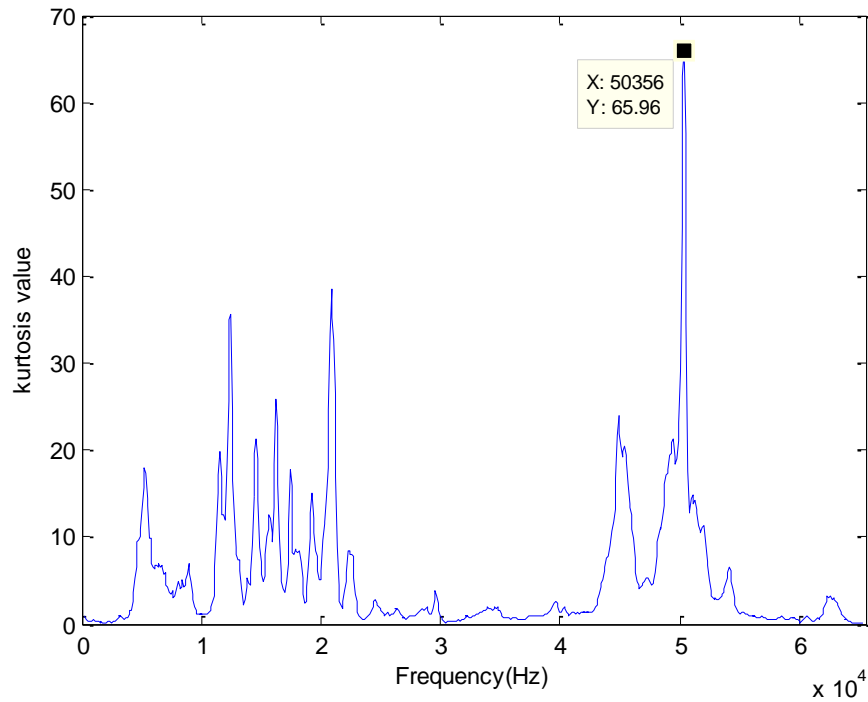


Fig. 6.19 Kurtrugram (0.8 mm outer race fault, external sensor)

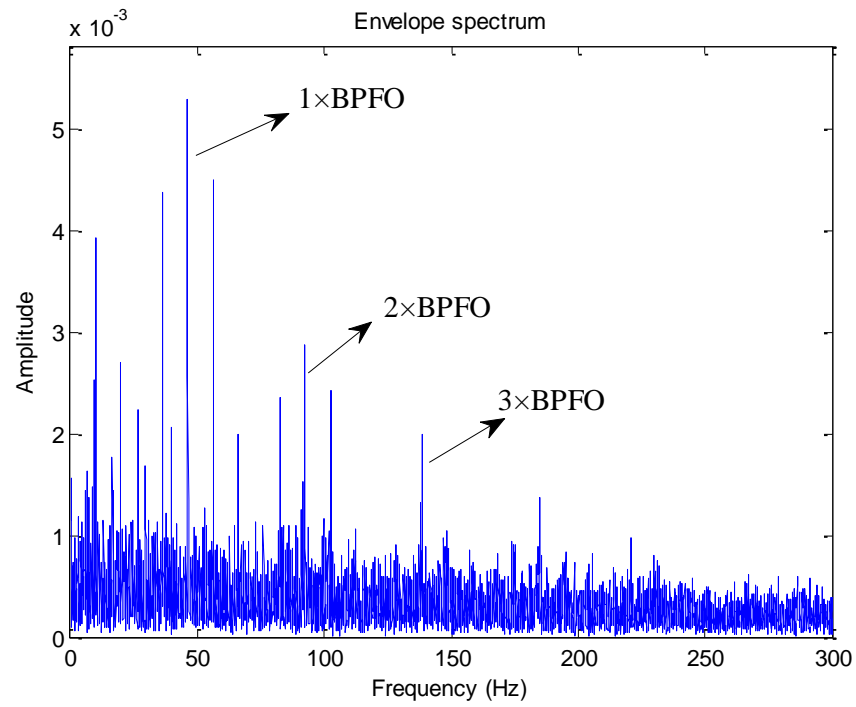


Fig. 6.20 Squared envelope spectrum (0.8 mm outer race fault, external sensor)

6.4.1.4 0.4 mm defect size

In this case, the characteristic frequency for the outer race fault is 45.76 Hz as the actual input shaft speed is 3.72 Hz. The proposed diagnostic procedure was applied to the vibration signal obtained from the internal accelerometer. As plotted in Fig. 6.21, the impulsiveness of the vibration signal became much clearer after the Cepstrum whitening step and MED filtering because the kurtosis value gradually increased from Fig. 6.21 (a) to Fig. 6.21 (c). The next step was to use the Kurtrugram to look for the best demodulation band. An optimal bandwidth of 512Hz was used on the basis of band selection criteria. The Kurtrugram is shown in Fig. 6.22, where the optimal center frequency for demodulation is 39756 Hz identified by its maximum kurtosis value of 102.9. Therefore, the high-frequency band [39500 Hz - 40012 Hz] is selected as the optimal demodulation band. Envelope analysis was then utilized at the selected high-frequency band for demodulation and fault information pick-up. As shown in the

squared envelope spectrum (Fig. 6.23), the bearing fault frequency could not be extracted, and the frequency components related to the carrier spin frequency (2.85 Hz) and the spur gear mesh frequency (156.1) dominate the envelope spectrum.

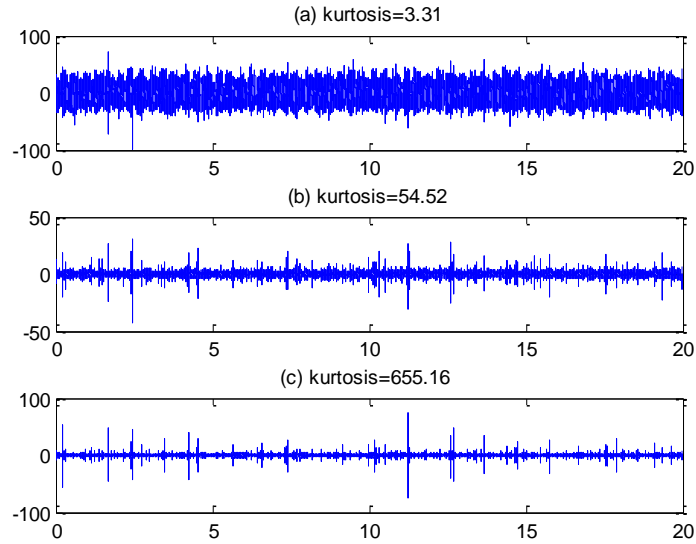


Fig. 6.21 (a) Raw time signal; (b) Cepstrum whitened signal; (c) Signal after Cepstrum whitening and MED filter (0.4 mm outer race fault, internal sensor)

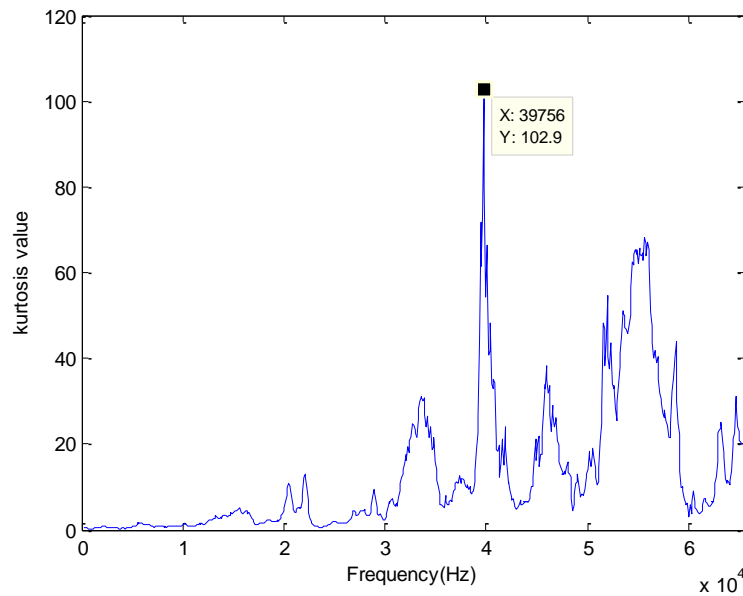


Fig. 6.22 Kurtrugram (0.4 mm outer race fault, internal sensor)

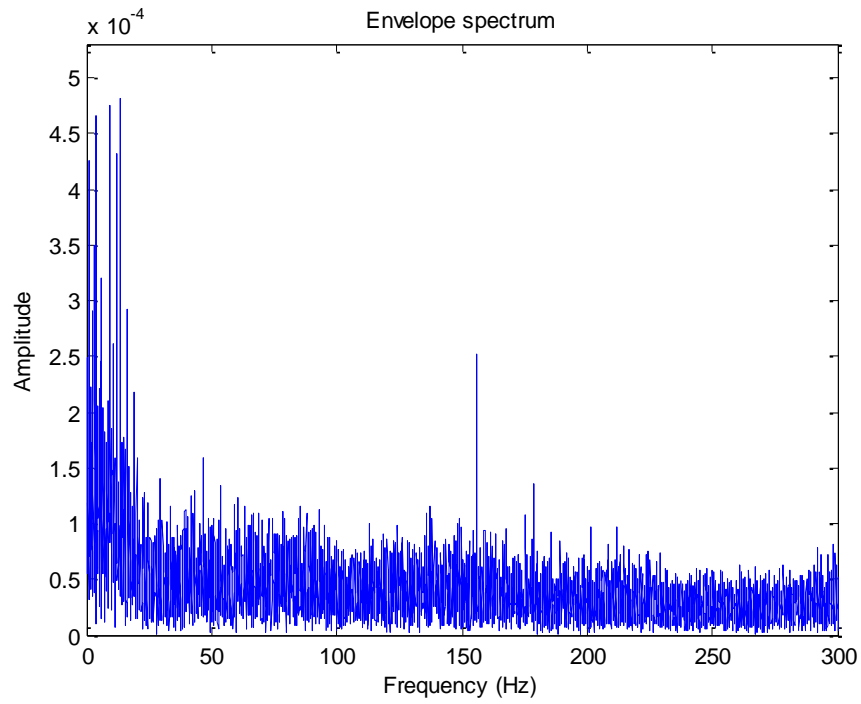


Fig. 6.23 Envelope spectrum (0.4 mm outer race fault, internal sensor)

The Kurtrugram and the squared envelope spectrum of the external sensor-based measurement are presented in Fig. 6.24 and Fig. 6.25 respectively. The optimal demodulation bandwidth was set to be 512 Hz, and the optimal center frequency was selected as 11656 Hz due to its maximum kurtosis value of 72.85. The envelope spectrum in Fig. 6.25 shows that the external sensor-based measurement also fails in recognizing the outer race fault in planetary bearings.

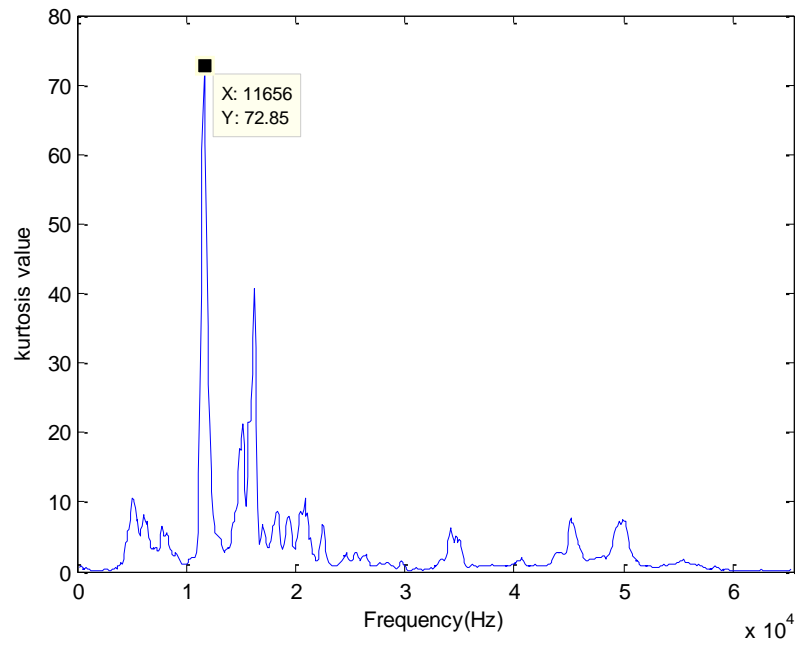


Fig. 6.24 Kurtrugram (0.4 mm outer race fault, external sensor)

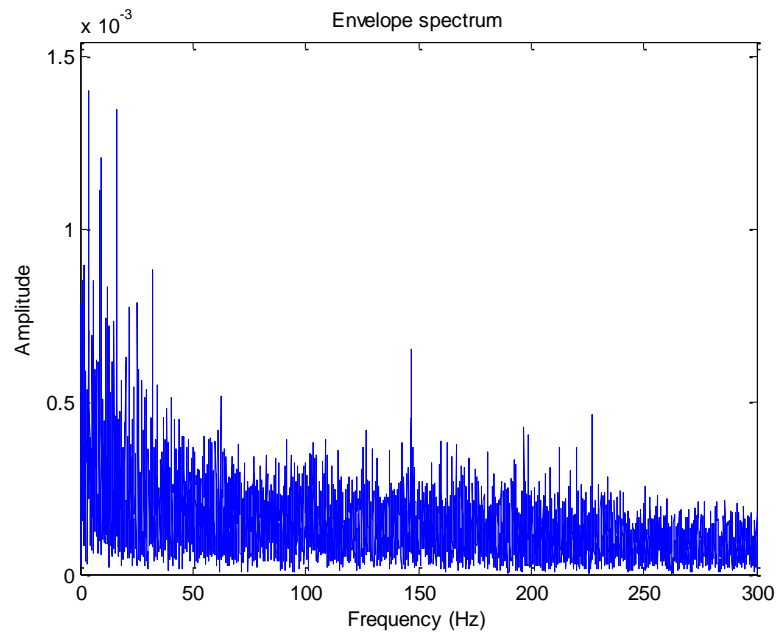


Fig. 6.25 Envelope spectrum (0.4 mm outer race fault, external sensor)

6.4.2 Inner race fault detection

For the inner race fault detection, the experimental results of the measured vibration signal, which were collected from a series of faulty bearings with different defect sizes

(widths of notches in the inner race were 0.4, 0.8, 1.2 and 1.6 mm), are respectively presented in sections 6.4.2.1-6.4.2.4.

6.4.2.1 1.6 mm defect size

The characteristic frequency for the outer race fault is 62.76 Hz as the actual input shaft speed is 3.71 Hz. In this case, the proposed diagnostic procedure was applied to the vibration signal acquired from the internal accelerometer. As presented in Fig. 6.26, the vibration signal became much more impulsive after the Cepstrum whitening step and MED filtering due to the gradually increasing kurtosis value from Fig. 6.26 (a) to Fig 6.26 (c). The next step was to use the Kurtrugram to look for the best demodulation band. An optimal bandwidth of 512Hz was used on the basis of band selection criteria presented in chapter 6. The Kurtrugram is shown in Fig. 6.27, where the optimal center frequency for demodulation was 61756 Hz identified by its maximum kurtosis value of 35.71. Therefore, the high-frequency band [61500 Hz - 62012 Hz] was chosen as the optimal demodulation band. Envelope analysis was then conducted at the selected high-frequency band for demodulation and fault information pick-up. The inner race fault frequency 63.45 Hz (a slight difference due to actual slip in the bearing) and its harmonics could be extracted in the envelope spectrum as plotted in Fig. 6.28. Also, the carrier spin frequency 2.8 Hz and the planet gear spin frequency 9.5 Hz could be recognized. Envelope spectrum for the same demodulation band of the good bearing is also presented in Fig. 6.29 as a comparison (note difference in amplitude scale). The dominant frequency components of the envelope spectrum include the 156.4 Hz of spur gear mesh frequency and 2.85 Hz of the carrier spin frequency.

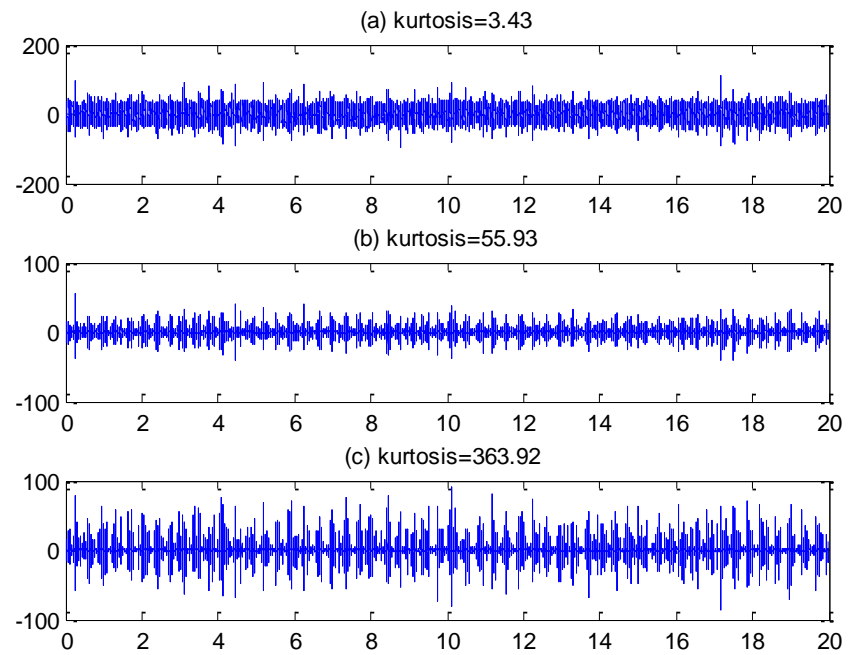


Fig. 6.26 (a) Raw time signal; (b) Cepstrum whitened signal; (c) Signal after Cepstrum whitening and MED filter (1.6 mm inner race fault, internal sensor)

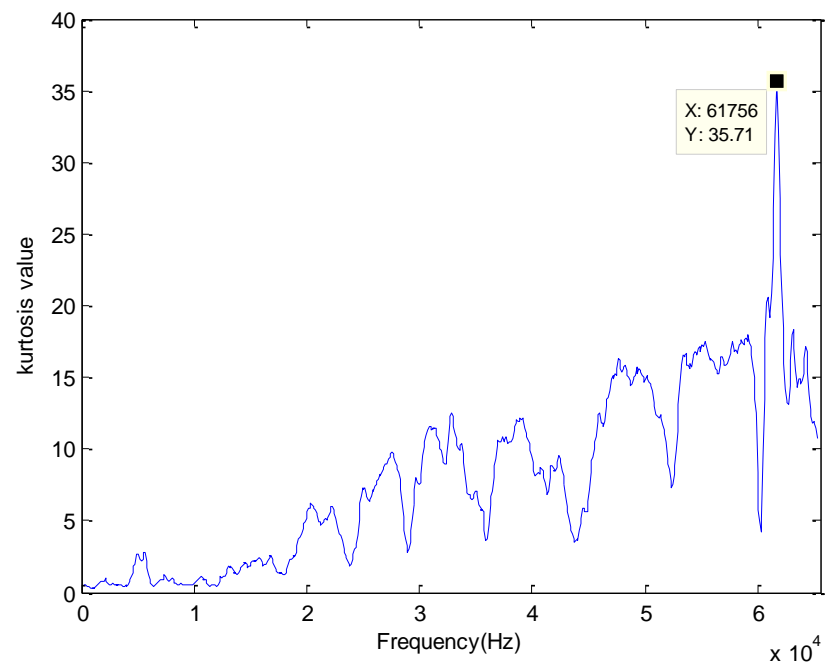


Fig. 6.27 Kurtrugram (1.6 mm inner race fault, internal sensor)

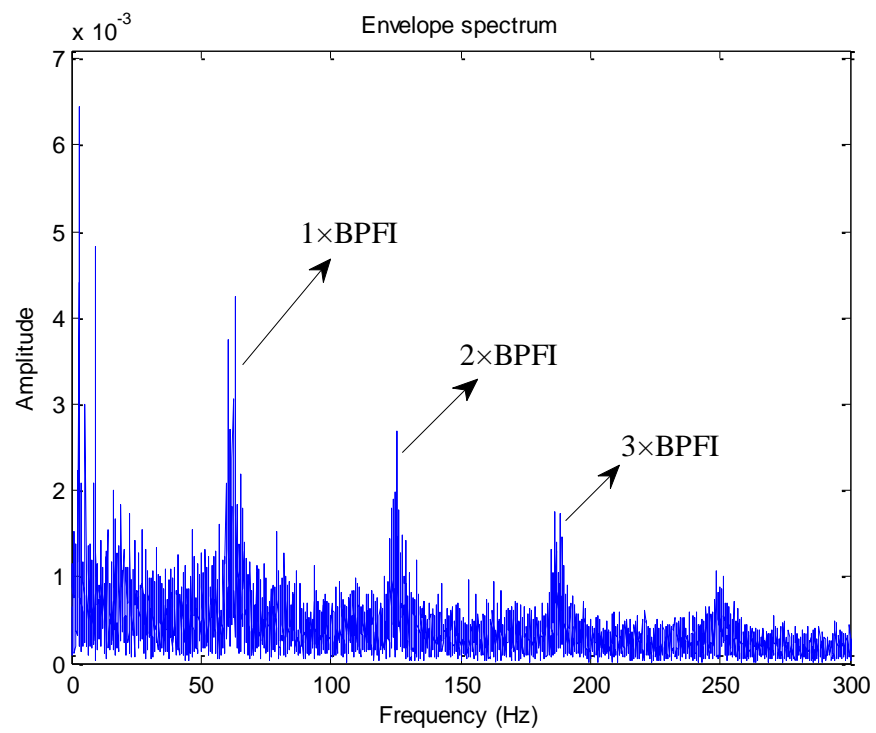


Fig. 6.28 Envelope spectrum (1.6 mm inner race fault, internal sensor)

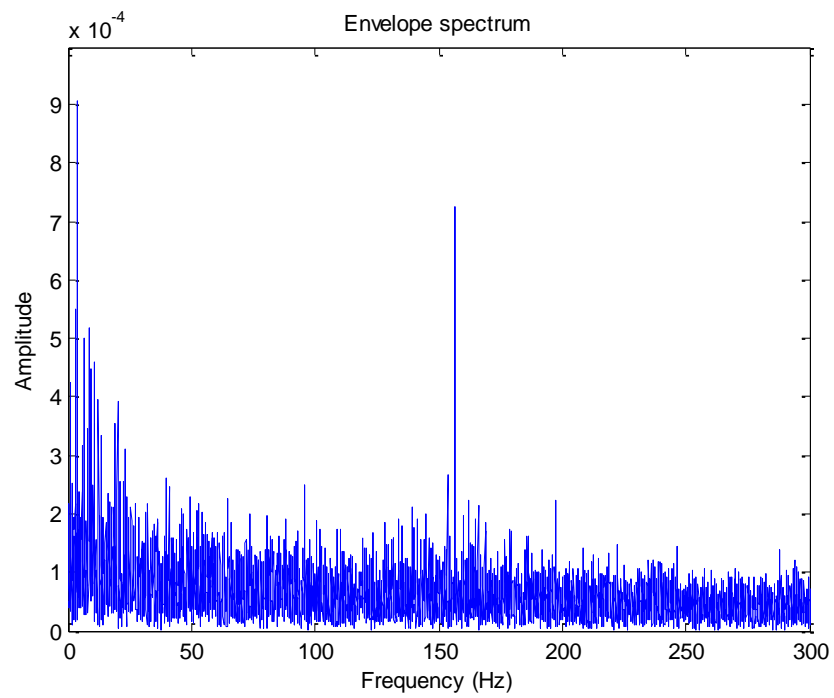


Fig. 6.29 Envelope spectrum (good bearing, internal sensor)

The analysis results using the external sensor signals are presented in Fig. 6.30 and Fig. 6.31 respectively. It is noted that the selected demodulation band is located in a relatively low-frequency area [17900 Hz - 18412 Hz] based on the maximum kurtosis value of 82.74. The related squared envelope spectrum shows that no bearing fault information could be identified through the selected demodulation band and the envelope spectrum is dominated by the planet gear spin frequency 9.5 Hz, carrier spin frequency 2.85 Hz and the harmonics.

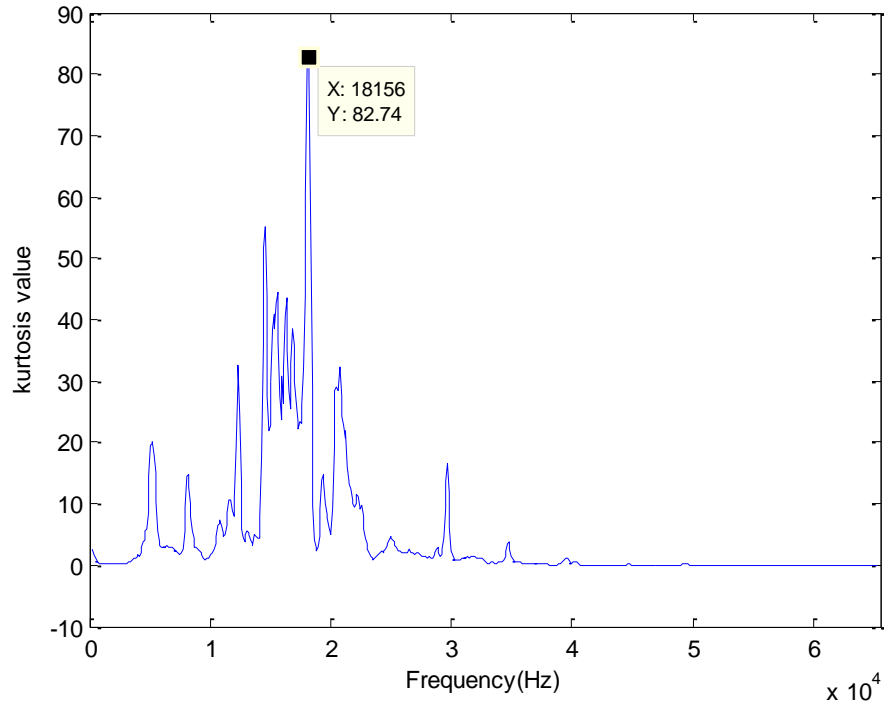


Fig. 6.30 Kurtrugram (1.6 mm inner race fault, external sensor)

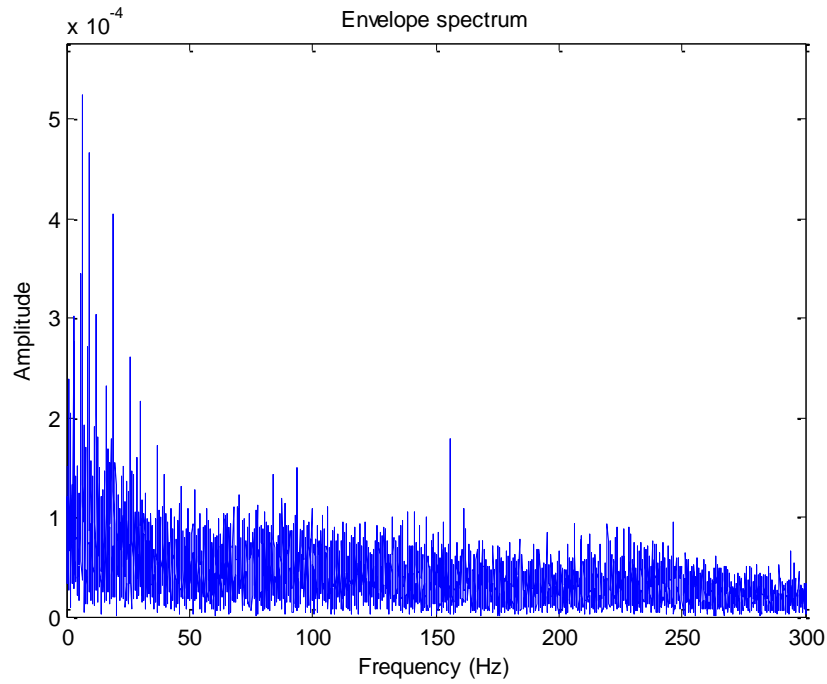


Fig. 6.31 Envelope spectrum (1.6 mm inner race fault, external sensor)

6.4.2.2 1.2 mm defect size

The characteristic frequency for the outer race fault is 62.59 Hz as the actual input shaft speed is 3.7 Hz. In this case, the proposed diagnostic procedure was applied to the vibration signal acquired from the internal accelerometer. As presented in Fig. 6.32, the vibration signal became much more impulsive after the Cepstrum whitening step and MED filtering due to the gradually increasing kurtosis value from Fig. 6.32 (a) to Fig. 6.32 (c). The further step was utilizing the Kurtrugram for the best demodulation band selection. The Kurtrugram is shown in Fig. 6.33, where the optimal center frequency for demodulation was 52456 Hz identified by its maximum kurtosis value of 51.37. Therefore, the high-frequency band [52200 Hz - 52712 Hz] was chosen as the optimal demodulation band. Envelope analysis was then conducted at the selected high-frequency band for demodulation and fault information extraction. The inner race fault frequency 62.15 Hz (a slight difference due to actual slip in the bearing) and its

harmonics could be extracted in the corresponding envelope spectrum plotted in Fig. 6.34. Also, the carrier spin frequency 2.85 Hz with a relatively low amplitude could be recognized. Envelope spectrum for the same band of the good bearing is presented in Fig. 6.35 as a comparison (note difference in amplitude scale). The dominant frequency components of the envelope spectrum include the 156.4 Hz of spur gear mesh frequency and 2.85 Hz of the carrier spin frequency.

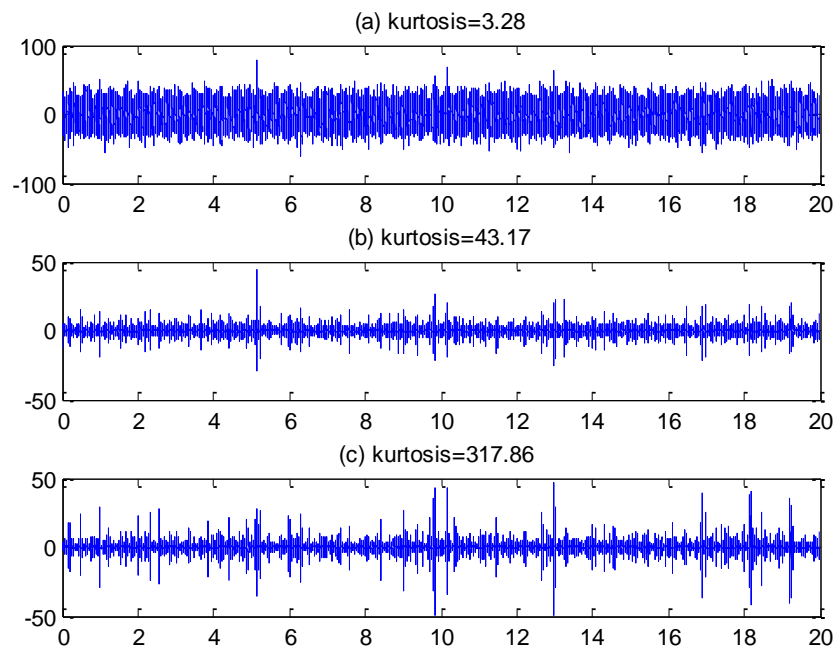


Fig. 6.32 (a) Raw time signal; (b) Cepstrum whitened signal; (c) Signal after Cepstrum whitening and MED filter (1.2 mm inner race fault, internal sensor)

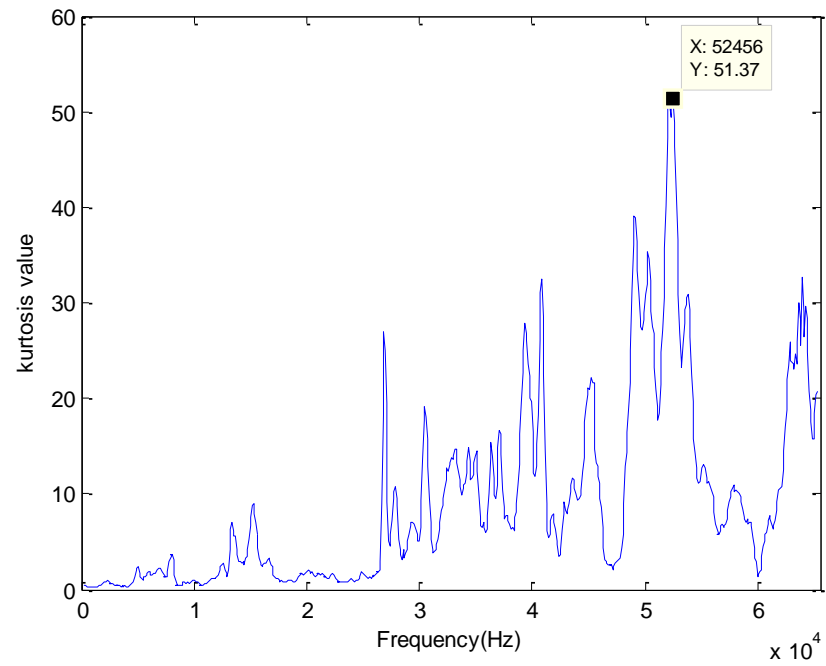


Fig. 6.33 Kurtrogram (1.2 mm inner race fault, internal sensor)

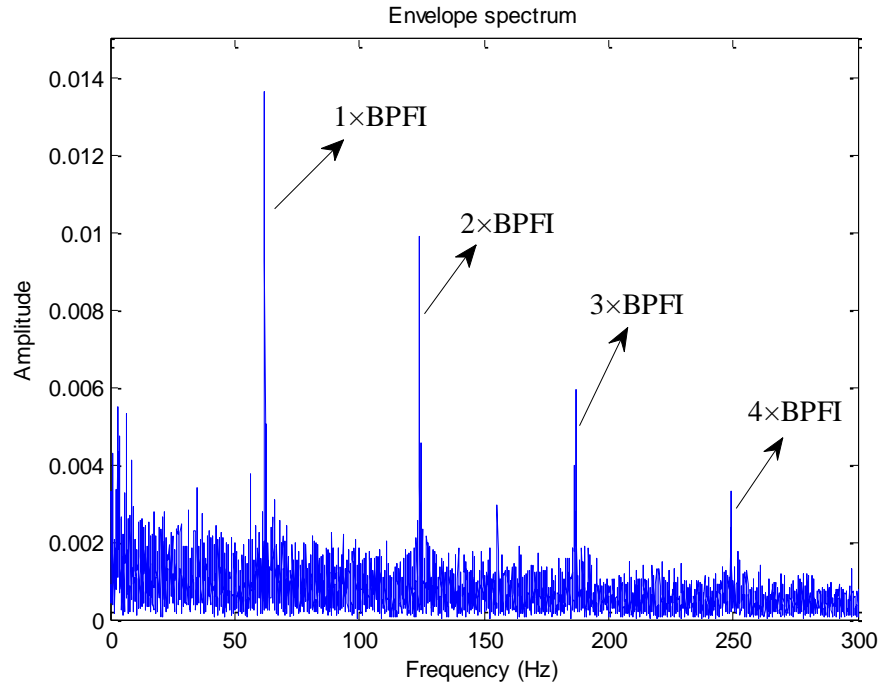


Fig. 6.34 Squared envelope spectrum (1.2 mm inner race fault, internal sensor)

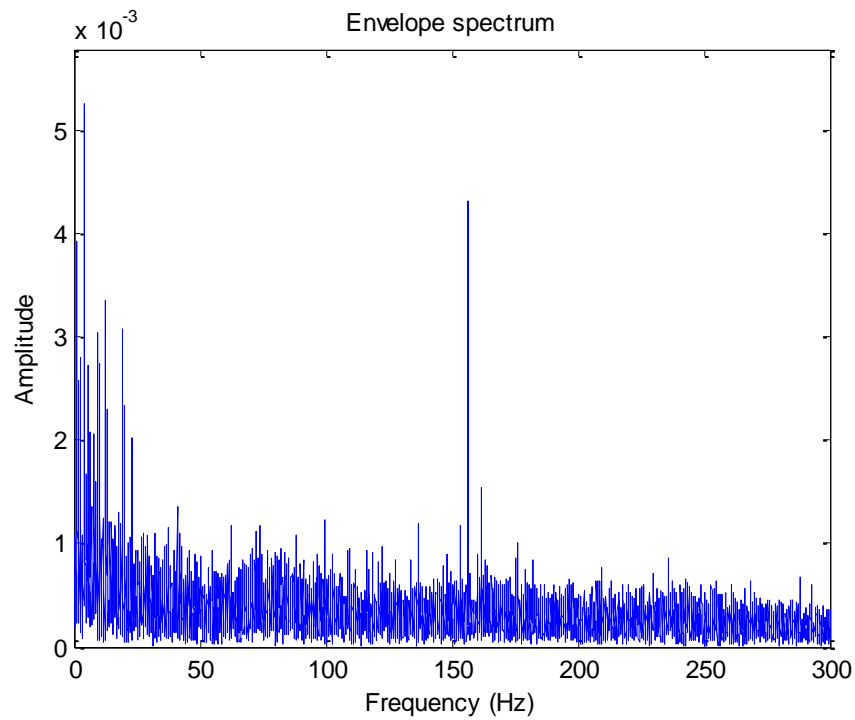


Fig. 6.35 Squared envelope spectrum (Good bearing, internal sensor)

The analysis results for the external sensor signals are presented in Fig. 6.36 and Fig. 6.37. It is noted that the selected demodulation band is located in a relatively low-frequency area [16000 Hz - 16512 Hz] based on the maximum kurtosis value of 71.5. As plotted in Fig. 6.37, the squared envelope spectrum shows that no bearing fault signature could be extracted from the selected demodulation band.

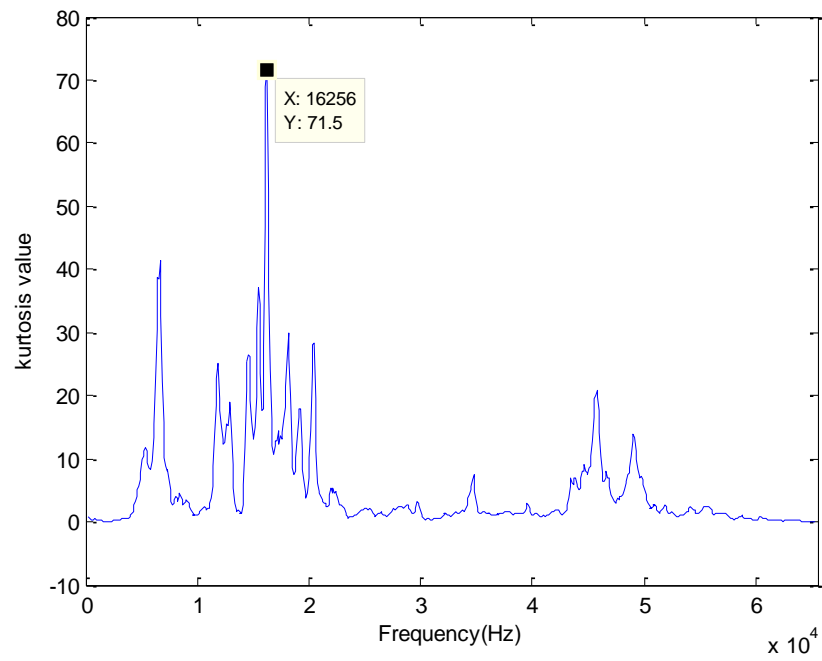


Fig. 6.36 Kurtrogram (1.2 mm inner race fault, external sensor)

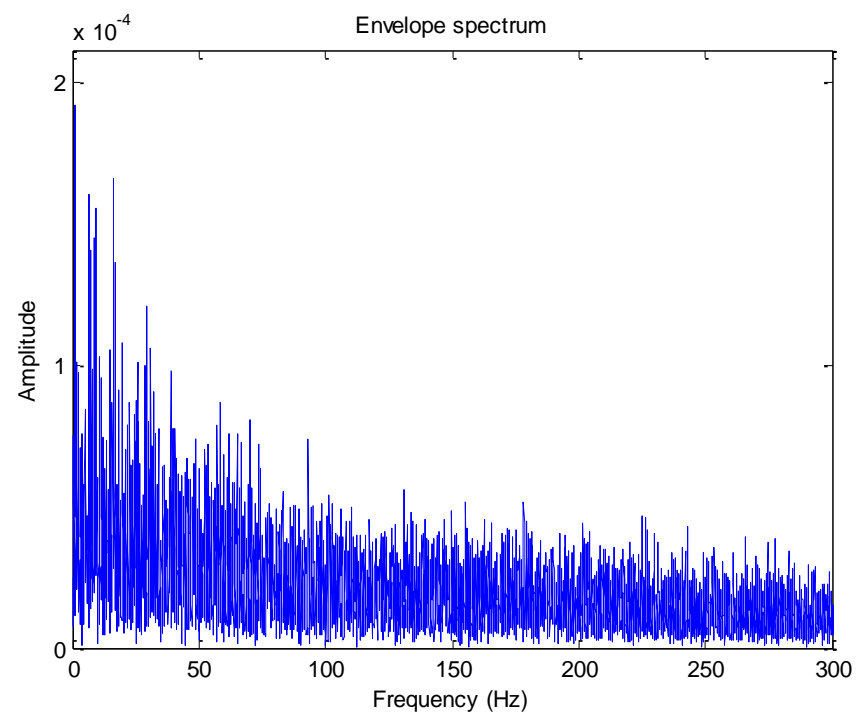


Fig. 6.37 Squared envelope spectrum (1.2 mm inner race fault, external sensor)

6.4.2.3 0.8 mm defect size

The characteristic frequency for the outer race fault is 62.93 Hz as the actual input shaft speed is 3.72 Hz. As presented in Fig. 6.38, the fault signal is more impulsive after the Cepstrum whitening and MED filtering steps as kurtosis value increases on the basis of the results in Fig. 6.38 (a) to Fig. 6.38 (c). The Kurtrugram was then applied for the best demodulation band selection. As presented in Fig. 6.39, where the optimal center frequency for demodulation was 55556 Hz identified by its maximum kurtosis value of 34.03. Thus, the high-frequency band [55300 Hz - 55812 Hz] was selected as the optimal demodulation band. Envelope analysis was then conducted at the selected high-frequency band for demodulation and fault information extraction. The inner race fault frequency 62.2 Hz (a slight difference due to actual slip in the bearing) and its harmonics could be extracted from the envelope spectrum plotted in Fig. 6.40. The planet carrier frequency of 2.85 Hz could also be extracted. Envelope spectrum for the same band of the good bearing is also presented in Fig. 6.41 as a comparison (note difference in amplitude scale). The main frequency components of the envelope spectrum (good bearing) are related to the 156.4 Hz of spur gear mesh frequency and 2.85 Hz of the carrier spin frequency.

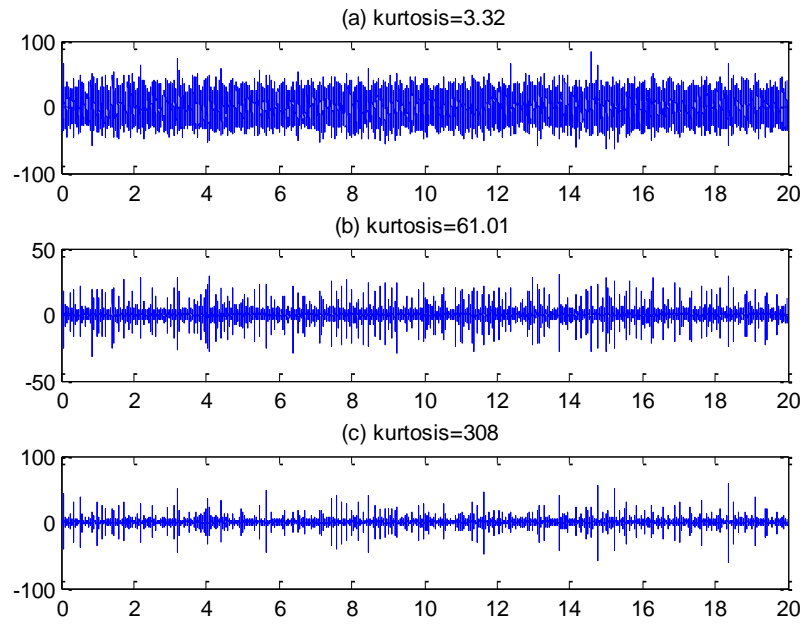


Fig. 6.38 (a) Raw time signal; (b) Cepstrum whitened signal; (c) Signal after Cepstrum whitening and MED filter (0.8 mm inner race fault, internal sensor)

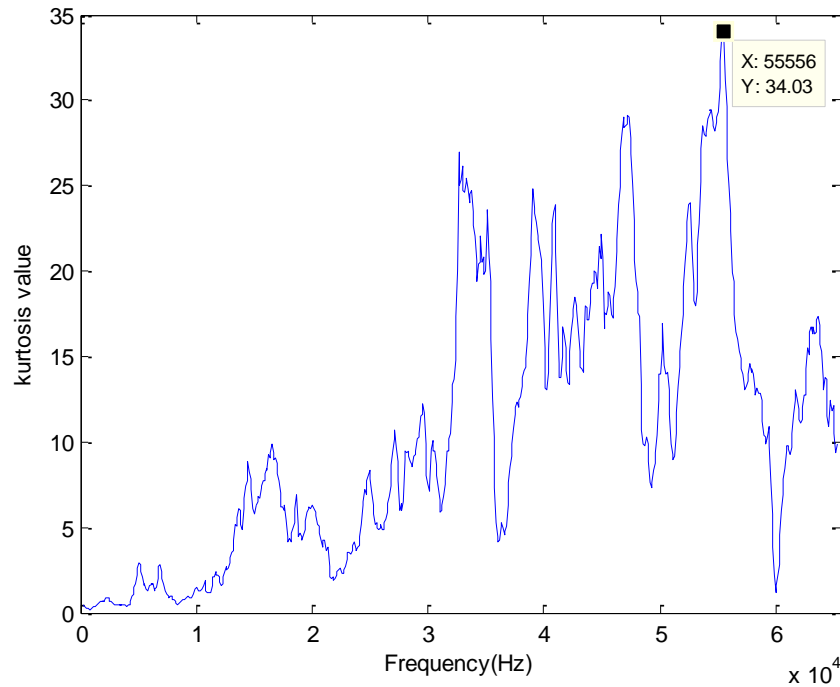


Fig. 6.39 Kurtrugram (0.8 mm inner race fault, internal sensor)

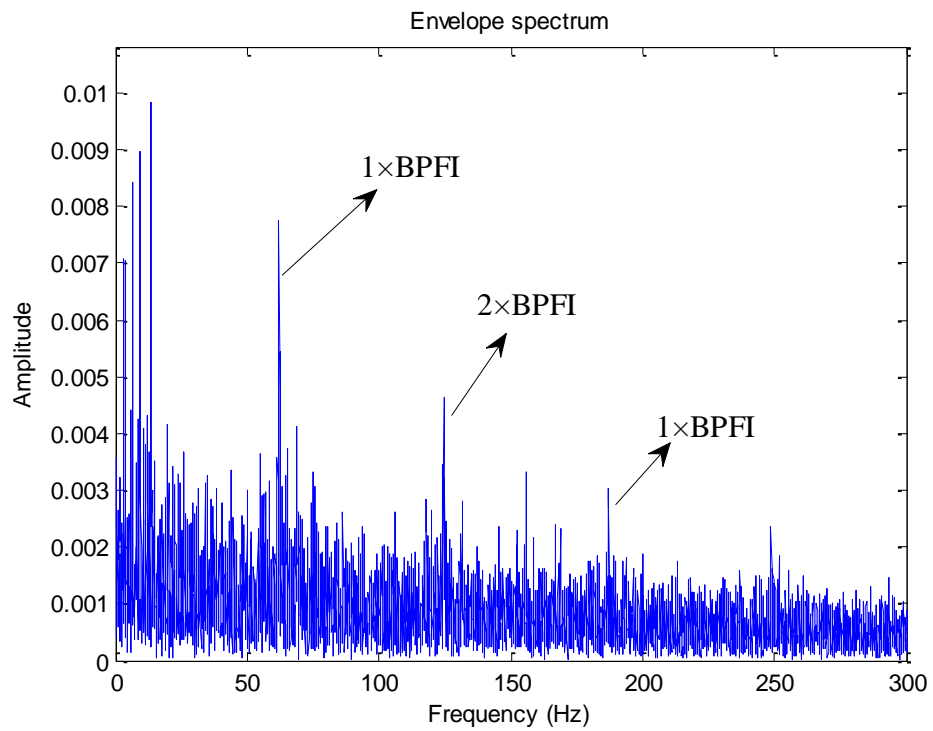


Fig. 6.40 Envelope spectrum (0.8 mm inner race fault, internal sensor)

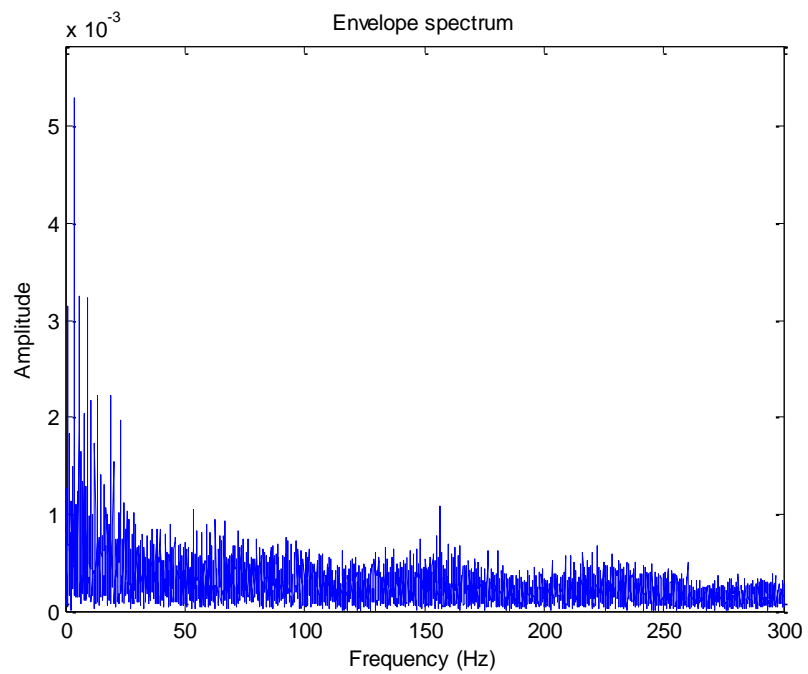


Fig. 6.41 Envelope spectrum (good bearing, internal sensor)

The analysis results for the external sensor signals are presented in Fig. 6.42 and Fig. 6.43. It is noted that the selected demodulation band is located in a relatively low-frequency area [14400 Hz - 14912 Hz] based on the maximum kurtosis value of 101.5. As plotted in Fig. 6.43, the results presents the planet gear spin frequency of 9.5 Hz, and the harmonics dominate the envelope spectrum and the bearing fault information could not be recognized.

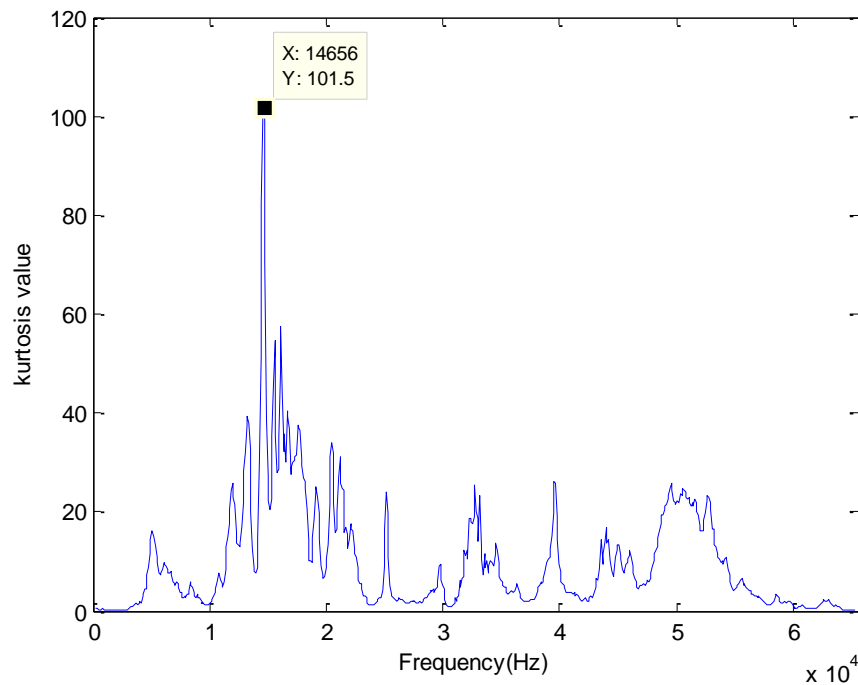


Fig. 6.42 Kurtrugram (0.8 mm inner race fault, external sensor)

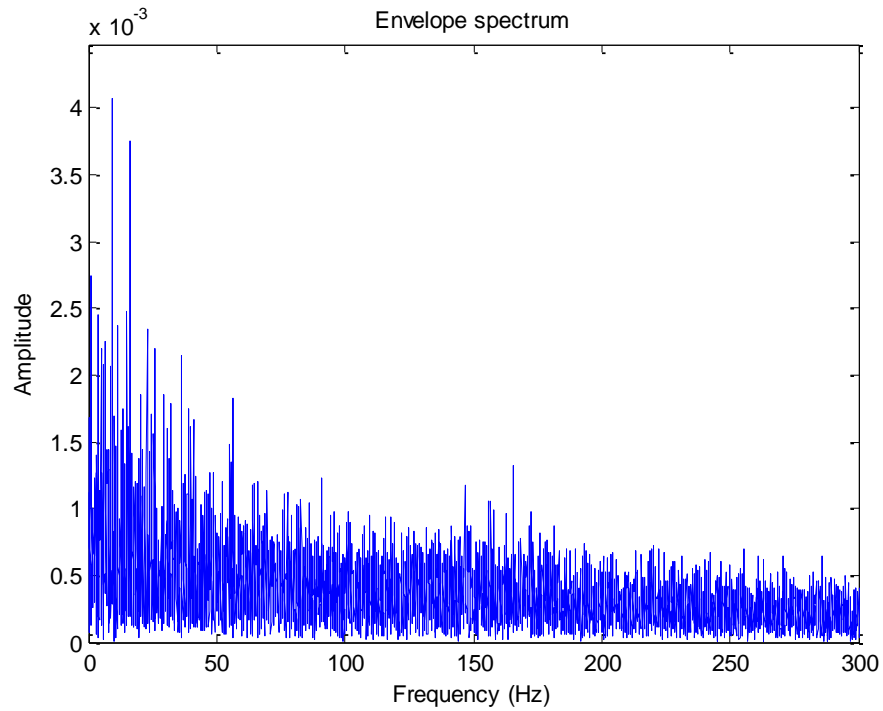


Fig. 6.43 Envelope spectrum (0.8 mm inner race fault, external sensor)

6.4.2.4 0.4 mm defect size

In this case, the characteristic frequency for the outer race fault is 62.76 Hz as the actual input shaft speed is 3.71 Hz. The proposed diagnostic procedure was applied to the vibration signal obtained from the internal accelerometer. As plotted in Fig. 6.44, the impulsiveness of the vibration signal became much clearer after the Cepstrum whitening step and MED filtering because the kurtosis value gradually increased from Fig. 6.44 (a) to Fig. 6.44 (c). The next step was to use the Kurtrugram to look for the best demodulation band. An optimal bandwidth of 512Hz was used in this case. The Kurtrugram is shown in Fig. 6.45, where the optimal center frequency for demodulation was 55156 Hz identified by its maximum kurtosis value of 232.7. Therefore, the high-frequency band [54900 Hz - 55412 Hz] was selected as the optimal demodulation band. Envelope analysis was then utilized at the selected high-frequency band for demodulation and fault information pick-up. As shown in the envelope spectrum (Fig.

6.46), the bearing fault frequency could not be extracted, and the envelope spectrum is dominated by the planet carrier spin frequency component (9.5 Hz).

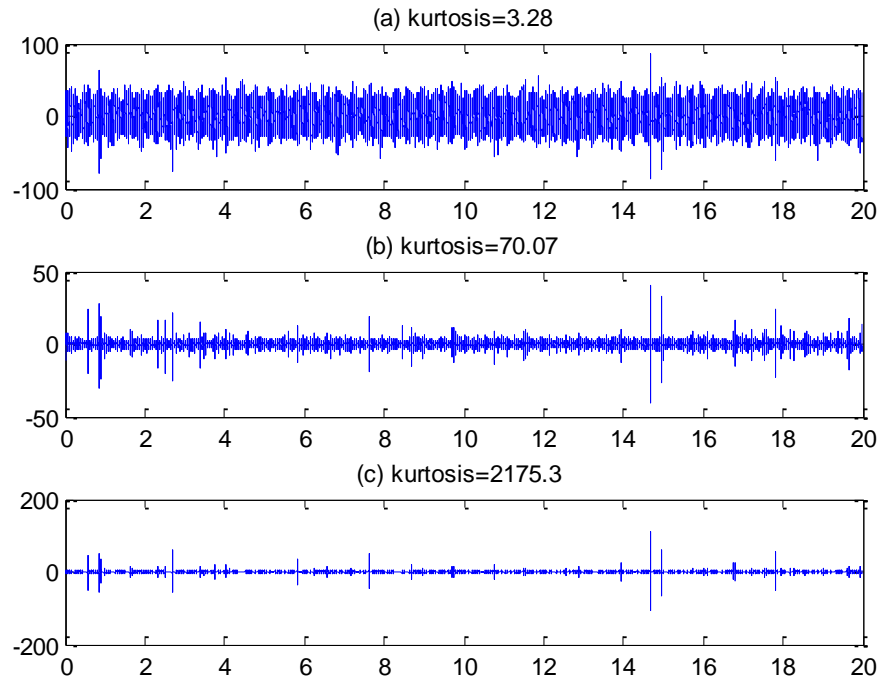


Fig. 6.44 (a) Raw time signal; (b) Cepstrum whitened signal; (c) Signal after Cepstrum whitening and MED filter (0.4 mm inner race fault, internal sensor)

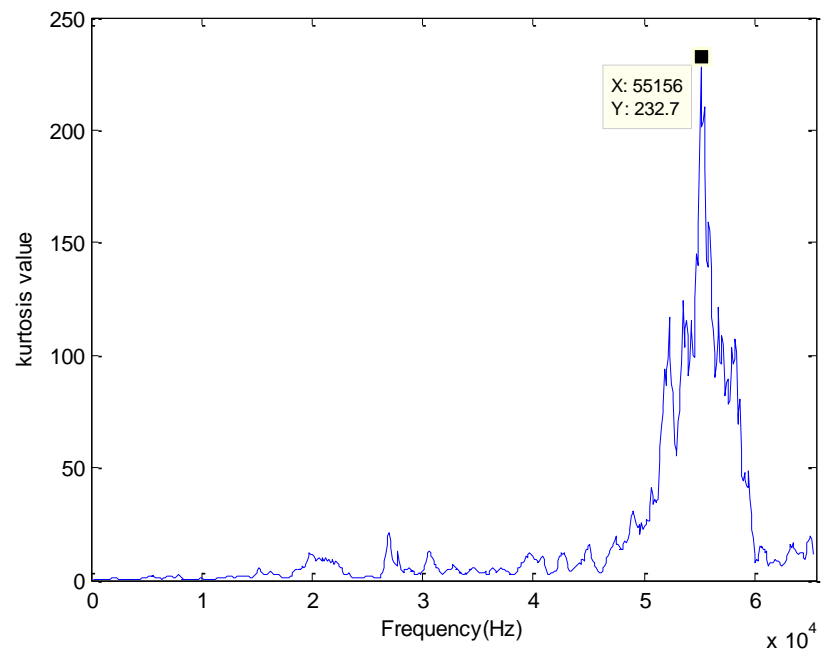


Fig. 6.45 Kurtrugram (0.4 mm inner race fault, internal sensor)

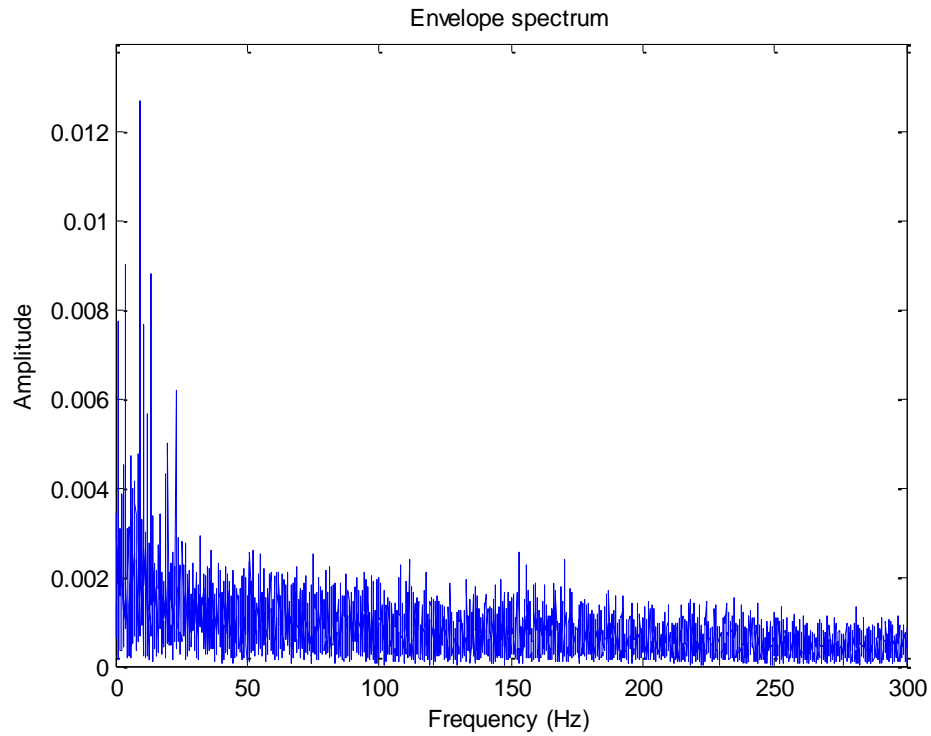


Fig. 6.46 Envelope spectrum (0.4 mm inner race fault, internal sensor)

The analysis results for the external sensor signals are presented in Fig. 6.47 and Fig. 6.48. It is noted that the selected demodulation band is located in a relatively low-frequency area [20900 Hz - 21412 Hz] based on the maximum kurtosis value of 71.01. As plotted in Fig. 6.48, the results presents that the planet gear spin frequency of 9.5 Hz and its harmonics dominate the envelope spectrum, and the bearing fault information could not be extracted.

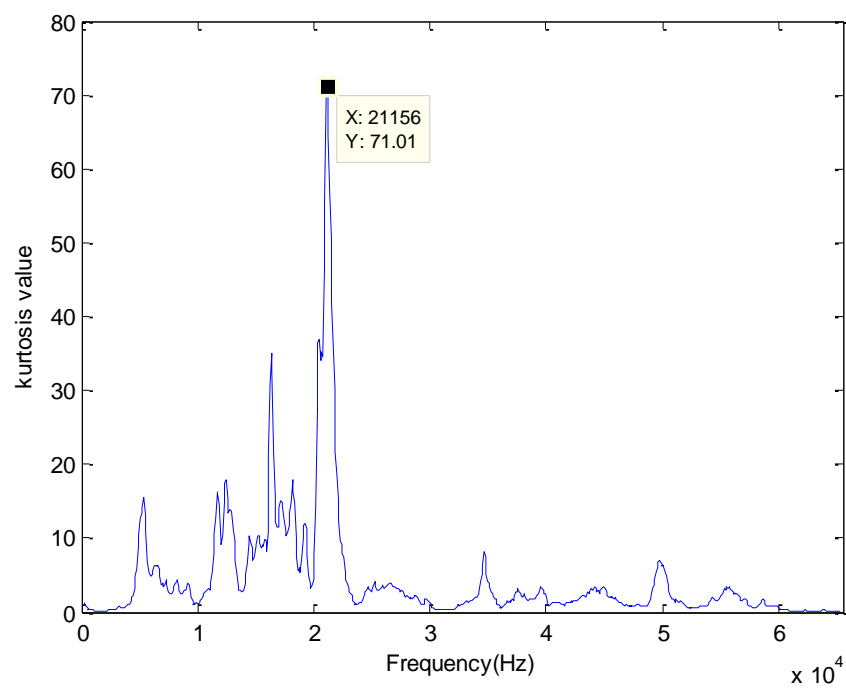


Fig. 6.47 Kurtrugram (0.4 mm inner race fault, external sensor)

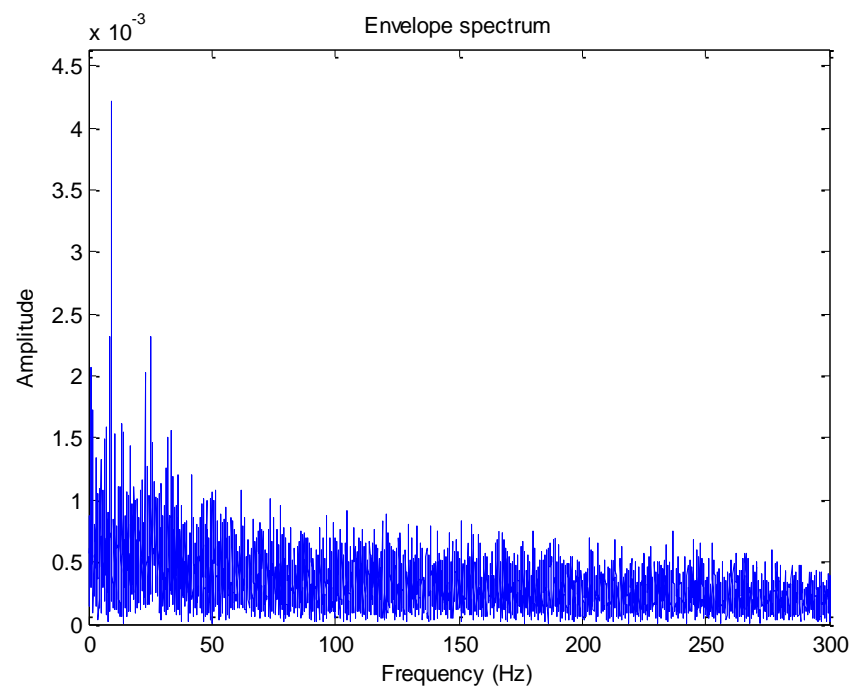


Fig. 6.48 Envelope spectrum (0.4 mm inner race fault, external sensor)

6.5 Discussions

6.5.1 Performance of outer race fault detection

The results of the proposed signal processing procedures for outer race fault detection are summarized in Table 6.3. Both of the internal sensor and external sensor-based measurements have good performances in detecting the outer race faults of planetary bearing. It is also noted that both of these two sensors could not detect the fault with the defect size of 0.4 mm. This is due to the reason that the bearing fault with a small defect size may generate a relative weak impulsive signal, which is masked by the background noise and hard to be extracted from the envelope signal. For the successful cases, the demodulation bands are chosen at very high-frequency bands with the range of 44-60 kHz. This is perhaps due to a small size of the bearings (with needle rollers of 3 mm diameter) exciting resonances only at very high frequencies.

Table 6.3 Diagnostic results for tests with outer race faults

Defect size (mm)	Sensor location	Demodulation band (Hz)	Diagnosis performance
1.6	External	44700-45212	Success
	Internal	52100-52612	Success
1.2	External	44800-45312	Success
	Internal	59100-59612	Success
0.8	External	50100-50612	Success
	Internal	55100-55612	Success
0.4	External	11400-11912	Fail
	Internal	39500-40012	Fail

6.5.2 Performance of inner race fault detection

The results of the proposed signal processing procedures for inner race fault detection are summarized in Table 6.4. It is clear that the internal sensor-based measurement is successful in recognizing the inner race faults of planetary bearing (defect size of 1.6, 1.2 and 0.8 mm), while the external sensor-based measurement fails in all cases. Same as the result of outer race fault case with the defect size of 0.4 mm, the internal sensor-based measurement also could not detect the inner race fault with the defect size of 0.4 mm (Although a high demodulation band was chosen in this case). For the successful cases with internal sensor, the demodulation bands are selected at high-frequency bands with the range of 52-62 kHz. Because the test bearing with a small size excites resonances only at very high frequencies. It is also interesting to notice that, for the all the failure cases of external sensor-based measurement, the demodulation bands were all chosen at the relative low-frequency bands with the range of 13-21 kHz.

Table 6.4 Diagnostic results for tests with inner race faults

Defect size (mm)	Sensor location	Demodulation band(Hz)	Diagnosis performance
1.6	External	17900-18412	Fail
	Internal	61500-62012	Success
1.2	External	16000-16512	Fail
	Internal	52200-52712	Success
0.8	External	14400-14912	Fail
	Internal	55300-55812	Success
0.4	External	20900-21412	Fail
	Internal	54900-55412	Fail

6.5.3 Effectiveness and limitations of the presented approach

As stated in section 6.1, this hybrid signal processing method is put forward for EMI issue raised from the internal sensor-based measurement and further highlighting the performance of internal sensor-based measurement in planetary bearing faults detection. Procedures of this proposed approach are primarily motivated by the semi-automated bearing diagnostic procedure, which was proved to be successful in a wide range of cases (plotted in Fig. 6.49 and details were presented in [27]). In this semi-automated procedure, step 1-2 are the preprocessing procedure for the separation of deterministic and random signal. Step 3 is for removing the effect of the transfer path and improving the clarity of the impulses. Step 4-5 is for the selection of optimum demodulation band (Fast Kurtogram) and the extraction of the bearing fault information.

For the applications of the internal sensor-based measurement, the measured vibration signal contains a large portion of EMI components. This EMI components negatively affects the performances of envelope analysis based signal processing methods [14], which includes the full bandwidth envelope analysis based approach (Cepstrum pre-whitening and envelope analysis) and narrow bandwidth envelope analysis based approach (order tracking, TSA, fast Kurtogram and envelope analysis). The procedures of the presented approach in this chapter are similar to the aforementioned semi-automated technique, which could be identified as a narrow bandwidth envelope analysis based procedure. However, some new changes are made in this proposed approach for improving the detection ability in the condition of intense EMI. The Cepstrum pre-whitening is utilized as the preprocessing step for the separation of deterministic and random signal. Because Cepstrum pre-whitening has better filtering performance compared with other common techniques and the step of order tracking is not required [43]. In addition, based on the results shown in chapter 5, the Cepstrum pre-whitening could also filter out parts of the EMI components in the measured signal. Instead of applying the technique of Fast Kurtogram in step 4 (Fig.

6.49), the new SK based method Kurtrugram is utilized for the optimal demodulation band selection, this method is mainly introduced in chapter 5, and the test results demonstrate it has better performance than Fast Kurtogram when the collected signal is corrupted by the EMI noise.

However, this presented signal processing procedure has some limitations. It could not be used for blind fault identifications, as the step of Kurtrugram requires the certain knowledge of the monitored system. In addition, the effectiveness of the presented method still needs to be validated in more industrial cases with the EMI interference.

6.6 Summary

This chapter presents an effective procedure for the diagnosis of the planetary bearing fault by using an internally mounted vibration sensor that rotates with the planet carrier rather than externally fixed. A set of signal processing methodologies, which combines the techniques of Cepstrum whitening, MED, Kurtrugram and envelope analysis, are employed for extracting the fault features in the measured signal through solving the demodulation band selection issue caused by electrical interference and for further optimizing the diagnostic performance of internal sensor-based measurement. The diagnosis performance using the traditional external mounted sensor is also presented as a comparison. The results demonstrated that both the external and internal accelerometers had good performances in outer race fault detection, but the presented internal sensor had an overwhelmingly superior performance in recognizing inner race faults.

CHAPTER 7 CONCLUSION AND FUTURE WORK

7.1 Conclusions

As stated previously, the aims of this research work are to develop a bearing fault detection method based on vibration data collected using an internally mounted accelerometer and to resolve the current EMI issues of the internal sensor-based measurement. The aims above of this project are achieved in this thesis via developing an effective signal processing procedure for the bearing diagnosis of internal sensor-based measurement.

The pretreatment process, as the first step of the signal processing procedure, was explored in chapter 4 for filtering out EMI components and other deterministic signals of the collected vibration signal. Several advanced signal processing techniques, including discrete random separation (DRS) and Cepstrum based techniques (Cepstrum editing and Cepstrum pre-whitening), were applied to the collected EMI signal for testing their abilities in removing the EMI components from the original signal. The results demonstrate that the Cepstrum pre-whitening is a suitable pretreatment process in the bearing fault detection procedure due to its high performance in filtering large portions of EMI components and its convenience in use. However, from the demodulation results of the processed signal, it is also noticed that a fraction of EMI signals remains, which means the residual EMI signal may still negatively influence the bearing faults detection and diagnosis.

In order to further reduce the impacts of the EMI interference in bearing fault diagnosis, a simple demodulation band selection method named as 'Kurtrugram' is presented in chapter 5 for effectively extracting bearing fault-related impulsive content from vibration signals contaminated with intense EMI. The method is then applied to internal sensor based vibration signals obtained from planet bearings seeded with both inner and outer race faults. The performance of the Kurtrugram method is compared

with two established optimal demodulation band selection techniques - Fast Kurtogram and Protrugram. The analysis demonstrates that the proposed method 'Kurtrugram' could overcome the drawbacks of aforesaid two established methods of dealing with the EMI-contaminated signals for selecting the right demodulation band. Also, the Kurtrugram has the potential applications in filtering out other types of wideband masking signals.

After the work of preprocessing step and optimal demodulation band selection mentioned above in this project, a systematic internal sensor based bearing fault detection procedure is established and presented in chapter 6. The techniques of Cepstrum pre-whitening, minimum entropy deconvolution (MED), Kurtrugram and envelope analysis, are utilized in this procedure for extracting the fault features of the measured signal via solving the demodulation band selection issue caused by EMI interference, and further optimizing the diagnostic performance of internal sensor-based measurement. Through applying the proposed signal processing procedure to the bearing fault data collected from hunting tooth planetary gearbox, the fault detection performance of internal sensor-based measurement could be further comprehensively investigated in this thesis. Compared with the traditional externally mounted sensor, it is found that the presented internal sensor has much better performance in detecting inner race faults of the planetary bearing.

7.2 Future work

7.2.1 Internal sensor-based measurement

- Investigating the performance of internal sensor-based measurement in the area of machine learning and pattern recognition. The statistical learning algorithms of artificial neural networks (ANNs) and support vector machine (SVM) would be employed. As both the signal processing techniques and machine learning

techniques are commonly applied in the area of machine fault detection and diagnosis, and the bearing fault detection performance of internal sensor-based measurement was investigated in this project via applying a series of signal processing techniques, and was proved to be more effective in detecting inner race fault than external sensor-based measurement. A further comparison of the bearing fault detection performance between the internal and traditional external sensors could be conducted through using the machine learning techniques for investigating whether the internal sensor has the better performance or not.

- Utilizing the vibration data collected from the internal accelerometer for the prognostics of planetary bearing faults. As the complex structure of the planetary gearbox, the vibration signal collected by the external sensor is strongly masked by both the deterministic signal and random noise. Thus, the established trending parameters may be affected by the noise and failed in estimating the fault severity. The internal sensor-based measurement may solve the issue above, as the internal sensor is close to the defect location and could obtain the bearing fault signal with a relative higher signal-to-noise ratio (SNR),
- Collecting and analyzing the planet gear faults data via using the internal accelerometer. As the internal sensor-based measurement was proved to have a better detection performance in planetary bearing faults detection, a systematic and efficient signal processing procedure could also be developed for investigating the planet gear fault detection ability of the internal sensor-based measurement.

7.2.2 EMI issue

- Applying the techniques of time-variant filtering for removing the EMI signal from the original vibration data. Although, the EMI issue is resolved by the method of Kurtrugram and the optimum demodulation band could be well selected.

The EMI components still appear in the envelope signal for some cases and may cause the problem in fault information extraction. In addition, filtering out the EMI components is crucial for the application of full bandwidth envelope analysis based techniques.

- Finding a better transmission strategy for the vibration data collected from the internal sensor. As chapter 4 demonstrates that the current signal transmission path via using the slip ring is the main reason for the EMI contamination. A better transmission strategy instead of slip ring transmission may lower the energy level of the EMI interference.
- Further investigations of the EMI issues using a simulation approach. The EMI interference is one of the major problems of the internally mounted sensor and simulated EMI signal could be applied to data analysis for finding the efficient filtering techniques.

References

- [1] Y. Lei, J. Lin, M. J. Zuo, and Z. He, "Condition monitoring and fault diagnosis of planetary gearboxes: A review," *Measurement*, vol. 48, pp. 292–305, Feb. 2014.
- [2] Y. Lei, J. Lin, Z. He, and D. Kong, "A method based on multi-sensor data fusion for fault detection of planetary gearboxes," *Sensors*, vol. 12, pp. 2005–2017, 2012.
- [3] D. G. Lewicki, R. T. Ehinger, and J. Fetty, "Planetary Gearbox Fault Detection Using Vibration Separation Techniques," in *67th Annual Forum and Technology Display*, 2011.
- [4] P. J. Dempsey, D. G. Lewicki, and D. D. Le, "Investigation of current methods to identify helicopter gear health," in *Aerospace Conference, 2007 IEEE*, 2007, pp. 1–13.
- [5] A. K. S. Jardine, D. Lin, and D. Banjevic, "A review on machinery diagnostics and prognostics implementing condition-based maintenance," *Mechanical Systems and Signal Processing*, vol. 20, no. 7, pp. 1483–1510, Oct. 2006.
- [6] R. B. Randall, *Vibration-based Condition Monitoring: Industrial, Aerospace and Automotive Applications*. 2010.
- [7] J. Yu and V. Makis, "Wavelet analysis with time-synchronous averaging of planetary gearbox vibration data for fault detection and diagnostics," in *2011 IEEE International Conference on Computer Science and Automation Engineering, CSAE 2011*, 2011, vol. 1, pp. 417–421.
- [8] W. Bartelmus and R. Zimroz, "Vibration condition monitoring of planetary gearbox under varying external load," *Mechanical Systems and Signal Processing*, vol. 23, no. 1, pp. 246–257, Jan. 2009.
- [9] T. Barszcz and R. B. Randall, "Application of spectral kurtosis for detection of a tooth crack in the planetary gear of a wind turbine," *Mechanical Systems and Signal Processing*, vol. 23, no. 4, pp. 1352–1365, May 2009.
- [10] Y. Lei, D. Han, J. Lin, and Z. He, "Planetary gearbox fault diagnosis using an adaptive stochastic resonance method," *Mechanical Systems and Signal Processing*, vol. 38, no. 1, pp. 113–124, Jul. 2013.

- [11] M. Khazaee, H. Ahmadi, M. Omid, and A. Moosavian, "An Appropriate Approach for Condition Monitoring of Planetary Gearbox Based on Fast Fourier Transform and Least-Square Support Vector Machine," *International Journal of Multidisciplinary Sciences and Engineering*, vol. 3, no. 5, pp. 22–26, 2012.
- [12] R. B. Randall, "Detection and diagnosis of incipient bearing failure in helicopter gearboxes," *Engineering Failure Analysis*, vol. 11, no. 2, pp. 177–190, Apr. 2004.
- [13] M. Ryan, "Internal vibration monitoring of a planetary gearbox," University of Pretoria, 2009.
- [14] W. Smith, L. Deshpande, R. Randall, and H. Li, "Bearing diagnostics in a planetary gearbox : a study using internal and external vibration signals," in *26th International Congress of Condition Monitoring and Diagnostic Engineering Management*, 2013.
- [15] G. L. Skibinski, R. J. Kerkman, and D. Schlegel, "EMI Emissions of Modern PWM AC Drives," *IEEE Industrial Applications Magazines*, vol. 5, no. 6, pp. 47–81, 1999.
- [16] J. Mathew and R.J.Alfredson, "The Condition Monitoring of Rolling Element Bearings Using Vibration Analysis," *Journal of Vibration and Acoustics*, vol. 106(3), pp. 447–453, 1984.
- [17] K. N. Gupta, "Vibration - A tool for machine diagnostics and condition monitoring," *Sadhana*, vol. 22(3), pp. 393–410, 1997.
- [18] Z. Peng, "An integrated intelligence system for wear debris analysis," *Wear*, vol. 252(9), pp. 730–743, 2002.
- [19] W. Zhou, T. G. Habetler, R. G. Harley, and Z. Wei, "Bearing Condition Monitoring Methods for Electric Machines: A General Review," *2007 IEEE International Symposium on Diagnostics for Electric Machines, Power Electronics and Drives*, pp. 3–6, 2007.
- [20] Z. Peng and N. Kessissoglou, "An integrated approach to fault diagnosis of machinery using wear debris and vibration analysis," *Wear*, vol. 255, no. 7–12, pp. 1221–1232, 2003.
- [21] S. Ebersbach, Z. Peng, and N. J. Kessissoglou, "The investigation of the condition and faults of a spur gearbox using vibration and wear debris analysis techniques," *Wear*, vol. 260, no. 1–2, pp. 16–24, Jan. 2006.

- [22] A. Choudhury and N. Tandon, "Application of acoustic emission technique for the detection of defects in rolling element bearings," *Tribology International*, vol. 33, pp. 39–45, 2000.
- [23] S. Bagavathiappan, B. B. Lahiri, T. Saravanan, J. Philip, and T. Jayakumar, "Infrared thermography for condition monitoring – A review," *Infrared Physics & Technology*, vol. 60, pp. 35–55, Sep. 2013.
- [24] C. Meola and G. M. Carlomagno, "Recent advances in the use of infrared thermography," *Measurement Science and Technology*, vol. 15, pp. R27–R58, 2004.
- [25] A. Soylemezoglu, S. Jagannathan, and C. Saygin, "Mahalanobis Taguchi System (MTS) as a Prognostics Tool for Rolling Element Bearing Failures," *Journal of Manufacturing Science and Engineering*, vol. 132(5), p. 051014, 2010.
- [26] N. Sawalhi, "Diagnostics , Prognostics and Fault Simulation For Rolling Element Bearings," University of New South Wales, 2007.
- [27] R. B. Randall and J. Antoni, "Rolling element bearing diagnostics—A tutorial," *Mechanical Systems and Signal Processing*, vol. 25, no. 2, pp. 485–520, Feb. 2011.
- [28] NPTEL, "Theory and Practise of Rotor Dynamics." [Online]. Available: <http://www.nptel.ac.in/courses/112103024/48>.
- [29] P. D. McFadden and J. D. Smith, "Model for the vibration produced by a single point defect in a rolling element bearing," *Journal of Sound and Vibration*, vol. 96, pp. 69–82, 1984.
- [30] P. D. McFadden and J. D. Smith, "The vibration produced by multiple point defects in a rolling element bearing," *Journal of Sound and Vibration*, vol. 98, pp. 263–273, 1985.
- [31] D. Ho and R. B. Randall, "Optimisation of Bearing Diagnostic Techniques Using Simulated and Actual Bearing Fault Signals," *Mechanical Systems and Signal Processing*, vol. 14, no. 5, pp. 763–788, Sep. 2000.
- [32] R. B. Randall, J. Antoni, and S. Chobsaard, "The Relationship Between Spectral Correlation and Envelope Analysis in the Diagnostics of Bearing Faults and Other Cyclostationary Machine Signals," *Mechanical Systems and Signal Processing*, vol. 15, no. 5, pp. 945–962, 2001.

- [33] A. Raad, J. Antoni, and M. Sidahmed, "Indicators of cyclostationarity: Theory and application to gear fault monitoring," *Mechanical Systems and Signal Processing*, vol. 22, no. 3, pp. 574–587, Apr. 2008.
- [34] J. Antoni, "Cyclostationarity by examples," *Mechanical Systems and Signal Processing*, vol. 23, no. 4, pp. 987–1036, May 2009.
- [35] C. R. Trimble, "What Is Signal Averaging?," *Hewlett-Packard Journal*, vol. 19(8), pp. 2–7, 1968.
- [36] P. D. McFadden and J. D. Smith, "Vibration monitoring of rolling element bearings by the high-frequency resonance technique — a review," *Tribology International*, vol. 17, no. 1, pp. 3–10, Feb. 1984.
- [37] P. D. McFadden, "A revised model for the extraction of periodic waveforms by time domain averaging," *Mechanical Systems and Signal Processing*, vol. 1, pp. 83–95, 1987.
- [38] P. D. Mcfadden and M. M. Toozhy, "Application of Synchronous Averaging To Vibration Monitoring of Rolling Element Bearings," *Mechanical Systems and Signal Processing*, vol. 14, no. 6, pp. 891–906, 2000.
- [39] D. Fried, J. Wolf, V. Pokasov, S. Khmelevstov, R. Buser, R. Lutomirski, R. Warren, A. Vinogradov, Y. Kravtsov, and V. Tatarski, "Adaptive Noise Cancelling : Principles and Applications," *Proceedings of the IEEE*, vol. 63, no. 12, pp. 105–112, 1975.
- [40] J. Antoni and R. B. Randall, "Unsupervised noise cancellation for vibration signals: part I—evaluation of adaptive algorithms," *Mechanical Systems and Signal Processing*, vol. 18, no. 1, pp. 89–101, Jan. 2004.
- [41] J. Antoni and R. B. Randall, "Unsupervised noise cancellation for vibration signals: part II—a novel frequency-domain algorithm," *Mechanical Systems and Signal Processing*, vol. 18, no. 1, pp. 103–117, Jan. 2004.
- [42] S. N. Randall R B, "A new method for separating discrete components from a signal," *Sound and Vibration*, vol. 45(5), p. 6, 2011.
- [43] P. Borghesani, P. Pennacchi, R. B. Randall, N. Sawalhi, and R. Ricci, "Application of cepstrum pre-whitening for the diagnosis of bearing faults under variable speed conditions," *Mechanical Systems and Signal Processing*, vol. 36, no. 2, pp. 370–384, Apr. 2013.

- [44] W. Geophysical, "Minimum entropy deconvolution," *Geoexploration*, vol. 16, pp. 21–35, 1978.
- [45] H. Endo and R. B. Randall, "Enhancement of autoregressive model based gear tooth fault detection technique by the use of minimum entropy deconvolution filter," *Mechanical Systems and Signal Processing*, vol. 21, no. 2, pp. 906–919, Feb. 2007.
- [46] N. Sawalhi, R. B. Randall, and H. Endo, "The enhancement of fault detection and diagnosis in rolling element bearings using minimum entropy deconvolution combined with spectral kurtosis," *Mechanical Systems and Signal Processing*, vol. 21, no. 6, pp. 2616–2633, Aug. 2007.
- [47] T. Barszcz and N. Sawalhi, "Fault Detection Enhancement in Rolling Element Bearings Using the Minimum Entropy Deconvolution," *Archives of Acoustics*, vol. 37, no. 2, pp. 131–141, Jan. 2012.
- [48] C. Junsheng, Y. Dejie, and Y. Yu, "A fault diagnosis approach for roller bearings based on EMD method and AR model," *Mechanical Systems and Signal Processing*, vol. 20, no. 2, pp. 350–362, Feb. 2006.
- [49] D. Yu, J. Cheng, and Y. Yang, "Application of EMD method and Hilbert spectrum to the fault diagnosis of roller bearings," *Mechanical Systems and Signal Processing*, vol. 19, no. 2, pp. 259–270, Mar. 2005.
- [50] H. Li, Y. Zhang, and H. Zheng, "Bearing fault detection and diagnosis based on order tracking and Teager-Huang transform," *Journal of Mechanical Science and Technology*, vol. 24, no. 3, pp. 811–822, Mar. 2010.
- [51] V. K. Rai and a. R. Mohanty, "Bearing fault diagnosis using FFT of intrinsic mode functions in Hilbert–Huang transform," *Mechanical Systems and Signal Processing*, vol. 21, no. 6, pp. 2607–2615, Aug. 2007.
- [52] W.-C. Tsao, Y.-F. Li, D. Du Le, and M.-C. Pan, "An insight concept to select appropriate IMFs for envelope analysis of bearing fault diagnosis," *Measurement*, vol. 45, no. 6, pp. 1489–1498, Jul. 2012.
- [53] J. Dybała and R. Zimroz, "Rolling bearing diagnosing method based on Empirical Mode Decomposition of machine vibration signal," *Applied Acoustics*, vol. 77, pp. 195–203, Mar. 2014.

- [54] Y. Wang and M. Liang, "An adaptive SK technique and its application for fault detection of rolling element bearings," *Mechanical Systems and Signal Processing*, vol. 25, no. 5, pp. 1750–1764, Jul. 2011.
- [55] J. Antoni and R. B. Randall, "The spectral kurtosis: application to the vibratory surveillance and diagnostics of rotating machines," *Mechanical Systems and Signal Processing*, vol. 20, no. 2, pp. 308–331, Feb. 2006.
- [56] J. Antoni and R. B. Randall, "The spectral kurtosis: Application to the vibratory surveillance and diagnostics of rotating machines," *Mechanical Systems and Signal Processing*, vol. 20, no. 2, pp. 308–331, Feb. 2006.
- [57] J. Antoni, "The spectral kurtosis: a useful tool for characterising non-stationary signals," *Mechanical Systems and Signal Processing*, vol. 20, no. 2, pp. 282–307, Feb. 2006.
- [58] J. Antoni, "Fast computation of the kurtogram for the detection of transient faults," *Mechanical Systems and Signal Processing*, vol. 21, no. 1, pp. 108–124, Jan. 2007.
- [59] Y. Zhang and R. B. Randall, "Rolling element bearing fault diagnosis based on the combination of genetic algorithms and fast kurtogram," *Mechanical Systems and Signal Processing*, vol. 23, no. 5, pp. 1509–1517, Jul. 2009.
- [60] W. Guo, P. W. Tse, and A. Djordjevich, "Faulty bearing signal recovery from large noise using a hybrid method based on spectral kurtosis and ensemble empirical mode decomposition," *Measurement*, vol. 45, no. 5, pp. 1308–1322, Jun. 2012.
- [61] Y. Lei, J. Lin, Z. He, and Y. Zi, "Application of an improved kurtogram method for fault diagnosis of rolling element bearings," *Mechanical Systems and Signal Processing*, vol. 25, no. 5, pp. 1738–1749, Jul. 2011.
- [62] B. Chen, Z. Zhang, Y. Zi, Z. He, and C. Sun, "Detecting of transient vibration signatures using an improved fast spatial-spectral ensemble kurtosis kurtogram and its applications to mechanical signature analysis of short duration data from rotating machinery," *Mechanical Systems and Signal Processing*, vol. 40, no. 1, pp. 1–37, Oct. 2013.
- [63] T. Barszcz and A. Jabloński, "A novel method for the optimal band selection for vibration signal demodulation and comparison with the Kurtogram," *Mechanical Systems and Signal Processing*, vol. 25, no. 1, pp. 431–451, Jan. 2011.

- [64] D. Wang, P. W. Tse, and K. L. Tsui, "An enhanced Kurtogram method for fault diagnosis of rolling element bearings," *Mechanical Systems and Signal Processing*, vol. 35, no. 1–2, pp. 176–199, Feb. 2013.
- [65] Brüel & Kjær, "Detecting faulty rolling-element bearings," 2007.
- [66] D. Dyer and R. M. Stewart, "Detection of Rolling Element Bearing Damage by Statistical Vibration Analysis," *Journal of Mechanical Design*, vol. 100, no. 77, p. 229, 1978.
- [67] N. Tandon and A. Choudhury, "A review of vibration and acoustic measurement methods for the detection of defects in rolling element bearings," *Tribology international*, vol. 32, pp. 469–480, 1999.
- [68] F. Al-Badour, M. Sunar, and L. Cheded, "Vibration analysis of rotating machinery using time–frequency analysis and wavelet techniques," *Mechanical Systems and Signal Processing*, vol. 25, no. 6, pp. 2083–2101, Aug. 2011.
- [69] Z. K. Peng and F. L. Chu, "Application of the wavelet transform in machine condition monitoring and fault diagnostics: a review with bibliography," *Mechanical Systems and Signal Processing*, vol. 18, no. 2, pp. 199–221, Mar. 2004.
- [70] Y. Lei, J. Lin, M. J. Zuo, and Z. He, "Condition monitoring and fault diagnosis of planetary gearboxes: A review," *Measurement*, vol. 48, pp. 292–305, Feb. 2014.
- [71] P.D.McFadden and I.M.Howard, "The detection of seeded faults in an epicyclic gearbox by signal averaging of the vibration," *AERONAUTICAL RESEARCH LABS MELBOURNE (AUSTRALIA)*, 1990.
- [72] G. D’Elia, E. Mucchi, and G. Dalpiaz, "On the Time Synchronous Average in Planetary Gearboxes," in *Surveillance 7 International Conference*, 2013.
- [73] Z. Feng, M. J. Zuo, J. Qu, T. Tian, and Z. Liu, "Joint amplitude and frequency demodulation analysis based on local mean decomposition for fault diagnosis of planetary gearboxes," *Mechanical Systems and Signal Processing*, vol. 40, no. 1, pp. 56–75, Oct. 2013.
- [74] J. Zhang, R. Yan, R. X. Gao, and Z. Feng, "Performance enhancement of ensemble empirical mode decomposition," *Mechanical Systems and Signal Processing*, vol. 24, no. 7, pp. 2104–2123, Oct. 2010.

- [75] T. Barszcz and R. B. Randall, "Application of spectral kurtosis for detection of a tooth crack in the planetary gear of a wind turbine," *Mechanical Systems and Signal Processing*, vol. 23, no. 4, pp. 1352–1365, May 2009.
- [76] Y. Lei, D. Han, J. Lin, and Z. He, "Planetary gearbox fault diagnosis using an adaptive stochastic resonance method," *Mechanical Systems and Signal Processing*, vol. 38, no. 1, pp. 113–124, Jul. 2013.
- [77] Z. Feng and M. Liang, "Fault diagnosis of wind turbine planetary gearbox under nonstationary conditions via adaptive optimal kernel time-frequency analysis," *Renewable Energy*, vol. 66, pp. 468–477, 2014.
- [78] Z. Feng and M. J. Zuo, "Fault diagnosis of planetary gearboxes via torsional vibration signal analysis," *Mechanical Systems and Signal Processing*, vol. 36, pp. 401–421, 2013.
- [79] Z. Feng and M. Liang, "Complex signal analysis for wind turbine planetary gearbox fault diagnosis via iterative atomic decomposition thresholding," *Journal of Sound and Vibration*, vol. 333(20), pp. 5196–5211, 2014.
- [80] L. Hong and J. S. Dhupia, "A time domain approach to diagnose gearbox fault based on measured vibration signals," *Journal of Sound and Vibration*, vol. 333, pp. 2164–2180, 2014.
- [81] R. B. Randall, "Detection and diagnosis of incipient bearing failure in helicopter gearboxes," *Engineering Failure Analysis*, vol. 11, no. 2, pp. 177–190, Apr. 2004.
- [82] J. Antoni, "The spectral kurtosis: a useful tool for characterising non-stationary signals," *Mechanical Systems and Signal Processing*, vol. 20, no. 2, pp. 282–307, Feb. 2006.
- [83] N. Sawalhi and R. B. Randall, "Helicopter gearbox bearing blind fault identification using a range of analysis techniques," *Engineering Assets Management*, pp. 724–737, 2006.
- [84] Y. Jiang, B. Tang, Y. Qin, and W. Liu, "Feature extraction method of wind turbine based on adaptive Morlet wavelet and SVD," *Renewable Energy*, vol. 36, no. 8, pp. 2146–2153, Aug. 2011.
- [85] J. Wang, R. X. Gao, and R. Yan, "Integration of EEMD and ICA for wind turbine gearbox diagnosis," *Wind Energy*, vol. 17(5), pp. 757–773, 2014.

- [86] A. Bligh, "Design , Manufacture and Testing of a Planetary Gearbox Rig," University of New South Wales, 2012.
- [87] N. Sawalhi and R. B. Randall, "Vibration response of spalled rolling element bearings: Observations, simulations and signal processing techniques to track the spall size," *Mechanical Systems and Signal Processing*, vol. 25, no. 3, pp. 846–870, Apr. 2011.
- [88] N. Sawalhi, "Spall Detection , Diagnosis and Quantification in Rolling Element Bearings using State of the Art Vibration Analysis."
- [89] N. Sawalhi, R. B. Randall, and H. Endo, "The enhancement of fault detection and diagnosis in rolling element bearings using minimum entropy deconvolution combined with spectral kurtosis," *Mechanical Systems and Signal Processing*, vol. 21, no. 6, pp. 2616–2633, Aug. 2007.
- [90] X. Zhang, N. Hu, L. Hu, B. Fan, and Z. Cheng, "Enhanced Fault Detection of Rolling Element Bearing Based on Cepstrum Editing and Stochastic Resonance," *Journal of Physics: Conference Series*, vol. 364(1), p. 012029, 2012.
- [91] Rajan Battish, "The 4-1-1 on Variable-Frequency Drives," *RTKL Electrical Construction and Maintenance*, 2011. [Online]. Available: <http://ecmweb.com/harmonics/4-1-1-variable-frequency-drives>.
- [92] P. E. Vanwiltenburg, "Mitigation of EMI Generated by a Variable-Frequency-Drive Controller for an AC Induction Motor," NAVAL POSTGRADUATE SCHOOL MONTEREY CA, 1994.
- [93] X. Pei, K. Zhang, Y. Kang, and J. Chen, "Analytical estimation of common mode conducted EMI in PWM inverter," in *Industry Applications Conference*, 2004, p. 4: 2651–2656.
- [94] G. Skibinski, J. Pankau, R. Sladky, and J. Campbell, "Generation, control and regulation of EMI from ac drives," in *Industry Applications Conference*, 1997, pp. 2:1571–1583.
- [95] J. Sun, "Pulse-Width Modulation," in *Dynamics and Control of Switched Electronic Systems*, F. V. and L. Iannelli, Ed. Springer London, 2012, pp. 25–61.
- [96] N. Sawalhi, K. Detrick, and S. Ganeriwala, "The Interference of Variable Frequency Drives (VFDs) on the Vibration Signature Analysis of Machine Defects," in *Tenth International Conference on Condition Monitoring and Machinery Failure Prevention Technologies*, 2013.

- [97] R. B. Randall, "A History of Cepstrum Analysis and Its Application to Mechanical Problems," in *Surveillance 7 International Conference*, 2013, pp. 1–16.
- [98] R. R. N. Sawalhi, "Semi-Automated Bearing Diagnostics-Three Case Studies," *NON DESTRUCTIVE TESTING AUSTRALIA*, vol. 45, p. 59, 2008.

Appendix MATLAB signal processing codes

A. Envelope analysis

```
function [env,Env,Env2] = EnvelopeTime1(xn,Bw,fc,fs,Lp)

nfft=length(xn);
df=fs/nfft;
Xn=(1/nfft)*fft(xn);
freq=(0:nfft-1)*df;
Bn=2*round(Bw/(df*2)); %Convert bandwidth to samples (nearest even value
so it can be halved later);
fn=round(fc/df); %Convert fc to samples;

%% Demodulation of FFT spectrum
N_demod=2^nextpow2(2*Bn); % Automated N_demod determination added by Wade
Smith, Oct 2012
sp=zeros(N_demod,1);
sp(1:Bn)=Xn((fn-Bn/2):(fn+Bn/2-1)); %Selection of band identified by using
Fast_Kurtogram
f_demod=freq(1:N_demod);
figure()
semilogy(f_demod,abs(sp))
xlabel('Zoomed bandwidth (Hz)')
ylabel('Amplitude')
title('Demodulation bandwidth (log scale)')

%% Inverse Transform to obtain complex (analytic) time signal
env=zeros(N_demod,1);
env_comp=N_demod*ifft(sp); %complete envelope
env_comp_abs=abs(env_comp); %amplitude
end_wnd=50; %no of samples to discard at beginning and end of envelope (equiv
to a rectangular window) to remove end effects
env(end_wnd:end-end_wnd)=env_comp_abs(end_wnd:end-end_wnd); %remove end
effects from envelope
t=(0:nfft-1)*(1/fs);
t_demod=t(1:N_demod).*(nfft/N_demod); %New time axis based on nfft for
```

```

demodulation band
figure()
plot(t_demod,env)
xlabel('Time (s)')
ylabel('Amplitude')
title('Envelope time signal (analytic signal (abs))')
xlim([0 max(t_demod)])

%% FFT of envelope signal
env_0DC=env-mean(env); %remove DC component
Env=(1/N_demod)*abs(fft(env_0DC));

%% Plot envelope:
figure()
plot(f_demod(2:end),Env(2:end)); hold on
xlabel('Frequency (Hz)')
ylabel('Amplitude')
title('Envelope spectrum')
xmax=Lp;
xlim([0 xmax])
ylim([0 1.1*max(abs(Env))])

%Calculate and plot the squared envelope
env2=env.^2;
env2_0DC=env2-mean(env2); %remove DC component
Env2=(1/N_demod)*abs(fft(env2_0DC));
figure()
plot(f_demod(2:end),Env2(2:end)); hold on
xlabel('Frequency (Hz)')
ylabel('Squared Envelope Amplitude')
title('Squared envelope spectrum')
xlim([0 xmax])
ylim([0 1.1*max(abs(Env2))])

```

B. Protrugram

```
function [k2,y] = rawProtrugram2(xn,Bw,step,fs)
tic
%% Input the raw signal and FFT transform
xn=xn-mean(xn);
Xn = fft(xn);

%% Select the bandwidth
nfft=length(xn);
df=fs/nfft;
freq=(0:nfft-1)*df;
Bn=Bw*nfft/fs; %Convert bandwidth to samples
% fn=round(fc/df); %Convert fc to samples;
%%
y=Bw/2:step:fs/2-Bw/2;
env=zeros(length(y),Bn);
for i=1:length(y)
    fc(i)=y(i);
    fn(i)=round(fc(i)*nfft/fs);
    sp(i,1:Bn)=Xn((fn(i)-Bn/2+1):(fn(i)+Bn/2));
    env_comp(i,:)=ifft(sp(i,:)); %complete envelope
    env_comp_abs(i,:)=abs(env_comp(i,:)); %amplitude
    end_wnd=50; %no of samples to discard at beginning and end of envelope
    (equiv to a rectangular window) to remove end effects

    env(i,end_wnd:end-end_wnd)=env_comp_abs(i,end_wnd:end-end_wnd); %remove
    end effects from envelope
    f(i,:)=env(i,end_wnd:end-end_wnd);
    F(i,:)=fft(f(i,:));
    F2(i,:)=F(i,2:end);
    k2(i)=kurtosis(abs(F2(i,:)));
end
figure;
plot(y(10:end),k2(10:end));xlim([0 fs/2])
title('Protrugram')
ylabel('kurtosis value');
```

```

        xlabel('Frequency(Hz) ');
toc

```

C. Kurtrugram

```

function [k1,y] = kurtrugram(xn,Bw,step,fs)
tic
%% Input the raw signal and FFT transform
xn=xn-mean(xn);
Xn = fft(xn);

%% Select the bandwidth
nfft=length(xn);
df=fs/nfft;
freq=(0:nfft-1)*df;
Bn=Bw*nfft/fs; %Convert bandwidth to samples
% fn=round(fc/df); %Convert fc to samples;
%%
y=Bw/2:step:fs/2-Bw/2;
env=zeros(length(y),Bn);
for i=1:length(y)
    fc(i)=y(i);
    fn(i)=round(fc(i)*nfft/fs);
    sp(i,1:Bn)=Xn((fn(i)-Bn/2+1):(fn(i)+Bn/2));
    env_comp(i,:)=ifft(sp(i,:)); %complete envelope
    env_comp_abs(i,:)=abs(env_comp(i,:)); %amplitude
    end_wnd=50; %remove end effects

    env(i,end_wnd:end-end_wnd)=env_comp_abs(i,end_wnd:end-end_wnd); %remove
end effects from envelope
    f(i,:)=env(i,end_wnd:end-end_wnd);
    f(i,:) = f(i,:) - mean(f(i,:));
    E1(i) = mean(abs(f(i,:)).^2);
    k1(i)= mean(abs(f(i,:)).^4)/E1(i)^2-2;

end
figure;
plot(y,k1);xlim([0 fs/2])
title('Kurtrugram')

```

```

        ylabel('kurtosis value');
        xlabel('Frequency (Hz) ');
    toc

```

D. Pulse width modulation signal

```

F2=input('Message frequency=');
F1=input('Carrier Sawtooth frequency=');
A=5;
t=0:1/131072:1-1/131072;
c=A.*sawtooth(2*pi*F1*t);%Carrier sawtooth
subplot(3,1,1);
plot(t,c);
xlabel('time');
ylabel('Amplitude');
title('Carrier sawtooth wave');
grid on;
m=0.75*A.*sin(2*pi*F2*t);%Message amplitude must be less than Sawtooth
subplot(3,1,2);
plot(t,m);
xlabel('Time');
ylabel('Amplitude');
title('Message Signal');
grid on;
n=length(c);%Length of carrier sawtooth
for i=1:n %Comparing Message and Sawtooth amplitudes
    if (m(i)>=c(i))
        pwm(i)=1;
    else
        pwm(i)=0;
    end
end
subplot(3,1,3);
plot(t,pwm);
xlabel('Time');
ylabel('Amplitude');
title('plot of PWM');
axis([0 1 0 2]);%X-Axis varies from 0 to 1 & Y-Axis from 0 to 2
grid on;

```